Master thesis : DESIGN OF REFRACTIVE OPTICAL LENSES FOR AN INFRARED CAMERA

Auteur : Riera Salva, Anna
Promoteur(s) : Habraken, Serge
Faculté : Faculté des Sciences appliquées
Diplôme : Master en ingénieur civil en aérospatiale, à finalité spécialisée en "aerospace engineering"
Année académique : 2017-2018
URI/URL : http://hdl.handle.net/2268.2/4632

University of Liège - Faculty of Applied Sciences
Academic year 2017-2018

DESIGN OF REFRACTIVE OPTICAL LENSES FOR AN INFRARED CAMERA

Graduation Studies conducted for obtaining the Master's degree in Aerospace Engineering by Anna Riera Salvà

Author: Anna Riera Salvà
Supervisor: Prof. Serge Habraken

With the collaboration of:

June 2018

Abstract

This master thesis is developed within the framework of the project OUFTI-NEXT (Orbital Utility for Thermal Imaging-NEXT). OUFTI-NEXT will be a CubeSat launched by Université de Liège with the collaboration of Centre Spatial de Liège (CSL). Its mission is to observe crop fields in order to monitor their temperature in the Mid-Wave InfraRed (MWIR) bandwidth.

More in detail, this master thesis presents a study of a refractive solution for the optical system of the thermal imaging system. Different solutions are studied from the simplest configuration with asphere lenses (doublet achromat) to a doublet hybrid (refractive-diffractive) configuration, considering also triplet configurations. The work focuses on the optical system without losing sight of the overall project (specifications and restrictions of the cubesat).

Keywords: *infrared, optics, cubesat*

Contents

List of Figures

List of Tables

Acknowledgements

First of all, I would like to express my deep gratitude to Prof. Serge Habraken, my master thesis supervisor, for his patient guidance and encouragement throughout all these months. He believed in me to face a subject in which I had little knowledge when I started. I would also like to thank Prof. Jérôme Loicq and Prof. Gaëtan Kerschen who, together with Prof. Serge Habraken and supervisors Xavier Werner and Victor Laborde, participate in this rewarding and ambitious project contributing with their knowledge, experience and time. I would also like to offer my special thanks to the students that also participate in this project: Donatien Calozet, Colin Dandumont, Anthony Kellens, Pierre Remacle and Lidiia Suleimanova. All together you have made me feel as part of the team.

My special thanks are extended to *Centre Spatial de Liège* for the chance to develop this work at your facilities. I am particularly grateful for the advice in optical design given by Ir. Alexandra Mazzoli and for the charming reception of Mr. Nicolas Grevesse and Ms. Florence Defraigne.

I wish to thank various people for their support during all these years of studying. Starting from this academic year, I would like to thank Miguel and Jordi, who were the first two people I met when I arrived, and Rebeca and Irene, who have become essential here in Liège in only few months.

I am also thankful to all the people I have met during the past years as a student in Terrassa. Especially to my classmates Anna, Anna, Ona and Natalia and the members of *Bergants*. You made hard days less hard and great days greater.

Finally, I wish to express my huge gratitude to Albert, who always encourages me, and to my family for their unconditional support even if they do not understand my decisions.

Acronyms

AR Anti-Reflection.

AS Aperture Stop.

CR Chief Ray.

CSL Centre Spatial de Liège.

DOE Diffractive Optical Element.

EFL Effective Focal Length.

FoV Field of View.

FPA Focal Plane Array.

FS Field Stop.

GSD Ground Sample Distance.

HOE Holographic Optical Element.

iFoV Instantaneous Field of View.

MCT Mercury Cadmium Telluride.

MR Marginal Ray.

MTF Modulation Transfer Function.

MWIR Mid-Wave InfraRed.

NEP Noise-Equivalent Power.

OPD Optical Path Difference.

OUFTI-1 Orbital Utility For Telecommunication Innovations.

OUFTI-NEXT Orbital Utility for Thermal Imaging - NEXT.

RMS Root Mean Square.

SNR Signal to Noise Ratio.

TMA Three Mirror Anastigmat.

ULiège Université de Liège.

Chapter 1

Introduction

1 Motivation: The OUFTI-NEXT project

OUFTI satellites are a series of CubeSats developed by students and professors from Université de Liège (ULiège). The first CubeSat, Orbital Utility For Telecommunication Innovations (OUFTI-1), was successfully launched in April 2016 with the mission to prove an innovative telecommunications protocol, called D-STAR. OUFTI-2, a CubeSat with the same characteristics than OUFTI-1, is currently being developed.

As a result of the successful OUFTI-1, a brainstorming session with several professors from different faculties took place on November 2016 to determine the mission of the next CubeSat. Finally, the idea that best convinced the team in charge of the project was to monitor the hydric stress in crop fields in order to improve the management efficiency of the water resources in arid regions. From that moment on, Orbital Utility for Thermal Imaging - NEXT (OUFTI-NEXT) was born.

Hydric stress detection can be done by observing in the Mid-Wave InfraRed (MWIR) bandwidth. When a plant does not have enough water closes its stomas, which are small apertures at the leaves surfaces,to avoid exchanging water vapor with the atmosphere. This leads to an increase of the temperature and it is a sign of hydric stress. Therefore, by comparing the ground surface temperature and the plants temperature it is possible to know if the plants need to be irrigated.

Monitoring crop fields for an efficiently management requires daily updated data. For doing this, a constellation of satellites is needed. Thus, only launching one OUFTI-NEXT is not enough to monitor the agricultural fields efficiently. However, this project does not pretend to directly manage some crop fields but to be a proof that it is possible to properly gather useful data by using a CubeSat.

This project is being developed by both professors and students from ULiège in collaboration with Centre Spatial de Liège (CSL). During the academic year 2016-2017 two feasibility studies of the mission were presented as a master thesis in the framework of the project [8] [28]. This master thesis is part of a set of seven currently being developed regarding different parts of the OUFTI-NEXT.

OUFTI-NEXT is designed as a 3U CubeSat. A 1U CubeSat corresponds to a $10 \times 10 \times 10$ cm^3 with a mass of not exceeding 1.33 kg. Therefore, OUFTI-NEXT will have a volume of $30 \times 10 \times 10$ cm^3, where the payload occupies only 1U. The payload consists of a thermal imaging system in the MWIR, which comprises mainly two parts: the optical system and the detector.

Regarding the optical system, three master thesis are being developed simultaneously to find different type of solutions in optical terms: reflective optics (mirrors), refractive optics (lenses) and refractive optics totally based on Fresnel lenses. In particular, this work focuses on

refractive lenses.

2 Objectives

The main objective of this master thesis is to survey the capability of a refractive optical system to accomodate the requirements of the OUFTI-NEXT payload. This main objective can be subdivided into the following subojectives:

- To design an appropriate lens configuration for the detector as simple as possible.
- To ensure that the proposed configuration works in the whole thermal range at which the optical system will be exposed.
- To proof that the proposed configuration fits the requirements of the CubeSat (in terms of available space and desired performance of the camera).

To achieve the objective, three steps are carried out. First, a literature research is done to study the configuration of refractive systems with similar characteristics. Second, an optimization of the studied configurations is carried out. This is done starting from the simplest one in order to keep the solution uncomplicated. Third, the changes in the system driven by the temperature are briefly studied.

Chapter 2

Background

1 Optical systems based on refractive lenses

The optical system is the combination of mirrors, lenses or prisms that collects the power so that it reaches the detector. As it has been said in chapter 1, this master thesis is focuses on an optical system based only on refractive lenses.

In contrast with the reflective optical systems, refractive systems depend on the light's wavelength. This is a huge disadvantage for two reasons: first, because the system will suffer from chromatic aberrations (see section 1.2.1) and, second and especially in the MWIR, because there are not many materials which are transparent for this bandwidth. In addition, the temperature variation can seriously affect the system. Despite all these disadvantages, refractive systems are usually more compact than reflective ones, which is a clearly advantage because of the reduced available space on board the satellite.

Next, a brief description of the fundamental parameters that characterize a refractive system is presented (see section 1.1), followed by a study of what affects the image quality (see section 1.2) and how to evaluate it (see section 1.3).

1.1 Description of a refractive optical system

Optical systems are characterized by a set of fundamental parameters:

- Optical axis: A line passing through the centre of curvature of a lens or spherical mirror and parallel to the axis of symmetry.
- Object Distance: Distance between the object being imaged and the lens. If the distance is very large it can be considered as infinite (see figure 2.1).
- Image Distance: Distance between the lens and the imaging plane (see figure 2.1).
- Effective Focal Length (EFL): Distance from the rear principal plane of an optical system to its imaging plane with an object located at infinity. The principal plane is defined as a hypothetical plane where incident light rays can be considered to bend due to refraction [24].
- Aperture Stop (AS): Stop or lens ring which physically limits the solid angle of rays passing through the system from an on-axis object point (see figure 2.2) [1].
- Entrance pupil: Opening an observer would identify as the limitation on the solid angle of rays diverging from an on-axis object point (see figure 2.2). Its diameter is the entrance pupil diameter (D_p).

- Exit pupil: Image of the aperture stop formed by the light rays after they have passed through the optical system (see figure 2.2) [1].
- f-number, f/#: ratio of the system's effective focal length to the diameter of the entrance pupil, $f/\# = \frac{EFL}{D_p}$
- Chief Ray (CR): For an off-axis object, it is the ray that passes through the center of the aperture stop (see figure 2.2) [1].
- Marginal Ray (MR): For an off-axis object, it is the ray that passes through the edge of the aperture stop (see figure 2.2) [1].
- FoV: Angle formed by the edges of the entrance window at the on-axis position of the entrance pupil [1]. It determines the angle through which the system is able to collect the power.
- Field Stop (FS): Solid angle formed by chief rays from off-axis objects.
- Wavelength band: Bandwidth for which the optical system is designed.

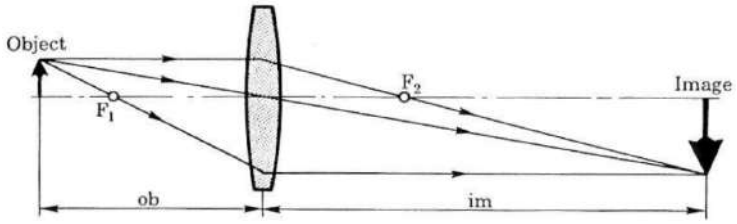

Fig. 2.1: Sketch for understanding Object Distance (ob) and Image Distance (im) parameters

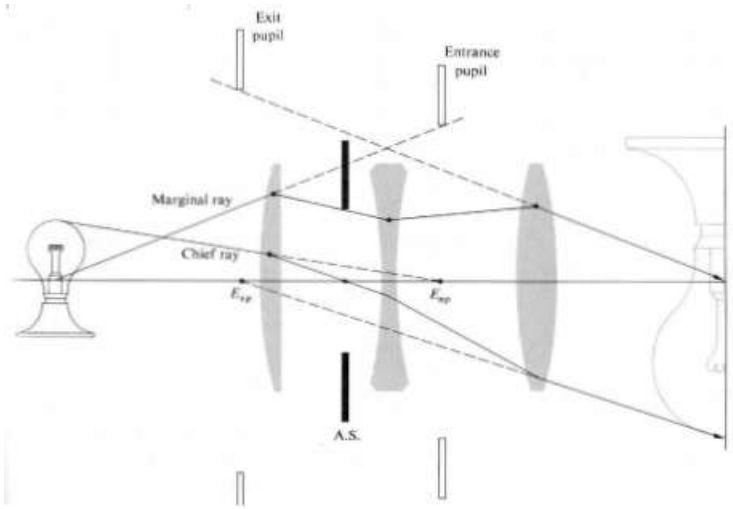

Fig. 2.2: Sketch for understanding CR, MR, AS, Entrance Pupil and Exit Pupil definitions parameters

1.2 Image quality: diffraction and aberrations

Image quality is never perfect. The image of a point object is never a perfect point image due to geometrical aberrations or diffraction. Geometrical aberrations are produced because of the

failure of the optical system to form a perfect geometrical image while diffraction is the effect resulting from the interaction of light with the sharp limiting edge of an optical system. This creates the so called Airy disk instead of a point (see figure 2.3). If the geometrical aberrations are significantly larger than the theoretical diffraction pattern, the geometrical aberrations will dominate. Otherwise, if the geometrical aberrations are much smaller than the theoretical diffraction pattern, the image will be dominated by the effect of the Airy disk. Finally, if both (geometrical and Airy disk) are approximately the same size, the image will be a somewhat degraded Airy disk [7]. In the next lines, there is a more detailed explanation on the existing types of geometrical aberrations and the theoretical diffraction limited pattern.

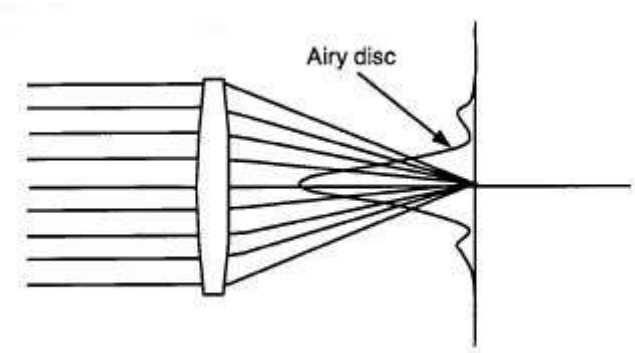

Fig. 2.3: Representation of the Airy Disk: it looks like a small gaussian intensity function surrounded by low intensity rings of energy [7]

1.2.1 Geometrical aberrations

As already discussed, aberrations are the failure of the optical system to produce a point image from a point object. There are different types of geometrical aberrations:

- **Spherical aberration**: It occurs when all the incoming rays end up focusing at different points of the optical axis because the rays passing near its horizontal axis are less refracted than those passing near the edge of the lens. Consequently, the rays passing near the edge of the lens converge closer to the lens than the ones passing near the horizontal axis (seen figure 2.4). This effect can be minimized by reducing the diameter of the lenses or by using aspheric surfaces (see section 1.4.3) [18].

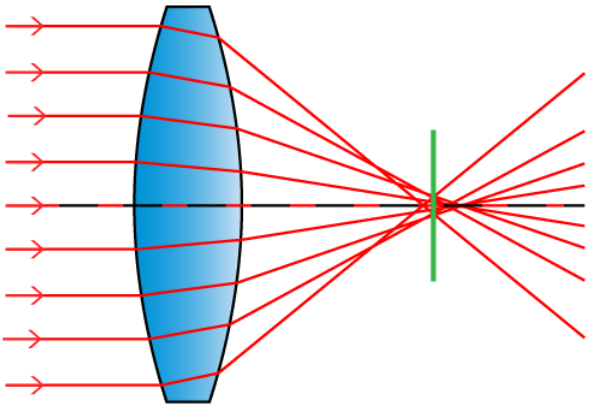

Fig. 2.4: Representation of spherical aberration [18]

- **Coma**: It causes rays from an off-axis point of light in the object plane to create a trailing "comet-like" blur directed away from the optic axis (see figure 2.5). It is caused by the difference of magnification. It can be minimized by moving the position of the aperture stop as far as they are not coincident with the lens. If moving the aperture stop is not possible, this abberration can also be minimized by using a combination of lenses symmetric about a central stop. It increases with the field of view and the aperture stop [7] [23].

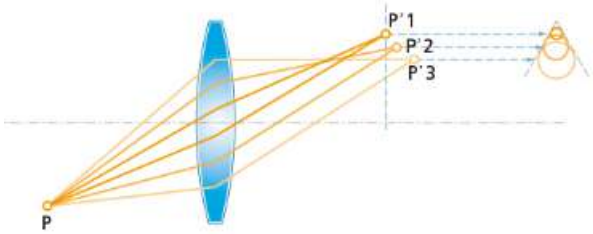

Fig. 2.5: Representation of coma [4]

- **Astigmatism**: It happens when rays in the meridional plane (which contains the optical axis of the lens) and sagittal plane (which is perpendicular to the meridional plane) are not focused at the same distance from the lens, having different focal points (see figure 2.6). It is difficult to reduce astigmatism, the only way is to design an anastigmatic system [7] [23].

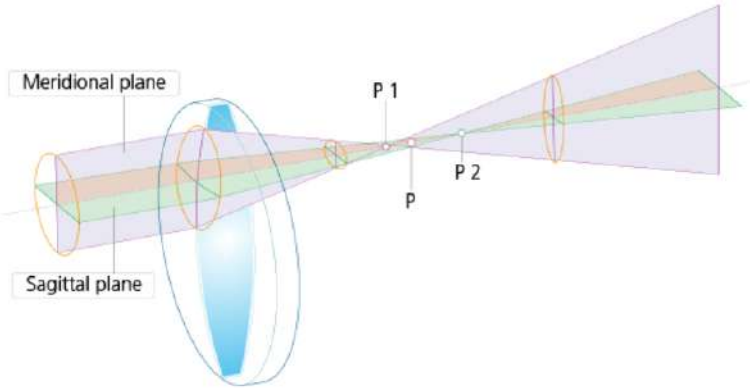

Fig. 2.6: Representation of astigmatism [4]

- **Field curvature**: In a positive lens, the image is not formed on a perpendicular plane to the optical axis but on a curved surface (see figure 2.7). If there is no astigmatism, this surface is called Petzval surface. This can be minimized by using a negative lens near the image plane [4] [7].

- **Distortion**: It is produced by variations in the magnification of the image depending on the distance from the optical axis (see figure 2.8) [4].

- **Chromatic aberration**: It is caused by the difference of wavelength of the electromagnetic radiation because the refraction index of the lens material varies with the wavelength.

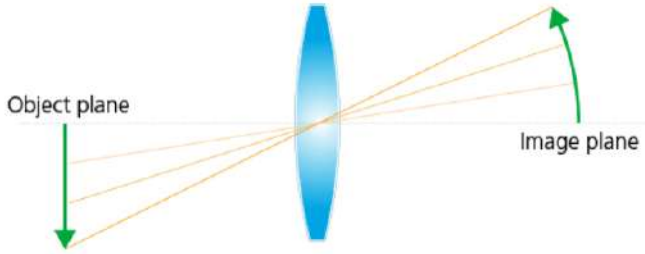

Fig. 2.7: Representation of field curvature [4]

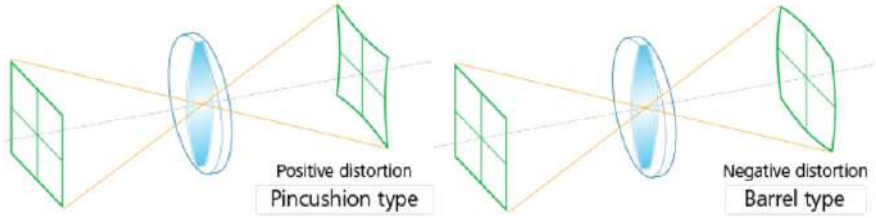

Fig. 2.8: Representation of distortion [4]

As a result, some wavelengths are more refracted than others. There are two types of chromatic aberrations: longitudinal (or axial) and lateral. Longitudinal chromatic aberration occurs when different wavelengths of color do not converge at the same point after passing through a lens (see figure 2.9(a)). Lateral chromatic aberration occurs when different wavelengths of color coming at an angle focus at different positions along the same focal plane (see figure 2.9(b)) [18]. This aberration can be corrected by using an achromatic doublet, which will be more deeply discussed in section 1.4.1.

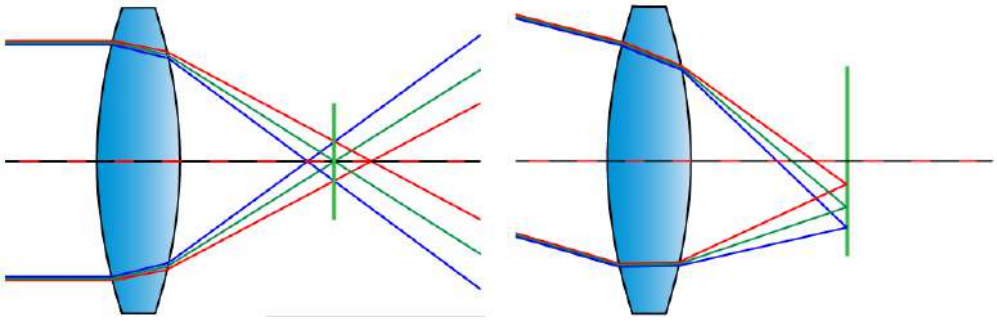

(a) Representation of longitudinal chromatic aberration

(b) Representation of lateral chromatic aberration

Fig. 2.9: Representation of chromatic aberrations [18]

1.2.2 Diffraction limit

As outlined before, due to the wave nature of radiation, the limiting edges of the system's aperture stop causes diffraction, converting the image of a point into a blur. If the system is dominated by diffraction instead of geometrical aberrations, the size of the diameter of the blur can be expressed as:

$$B_{diff} = 2.44\lambda f/\# \tag{2.1}$$

It is seen that the blur size is proportional to the wavelength, λ. Since the wavelength of the infrared is larger than visible light, infrared systems are more easily limited. Also, the smaller the f/#, the smaller the blur size due to diffraction. Consequently, to avoid limit diffraction EFL must be small and D_p large [27] [7].

1.3 Evaluation of the system

Nowadays, there exist many different softwares to design optical systems (*Code V*, *ASAP*, *Zemax*, ...) based on the optimization of a basic design. These programs do different graphics of the system's performance so that the user can determine if the designed system is good enough for the desired application. In the following lines, the most useful graphics used to determine the performance of an optical system are explained.

- **Ray Aberration Curves**: Also called ray trace curves, these curves measure the linear ray deviation from the focus point, allowing the designer to determine which aberrations are present and in which magnitude. They have two forms: longitudinal and transverse. The longitudinal ray aberration curves measures the distance between the aberrated chief ray and the focus point. The transverse ray aberration curve measures the distance between the focal point and the ray height above or below it in the focal plane [32]. Figure 2.10 shows the most typical ray aberrations curves.

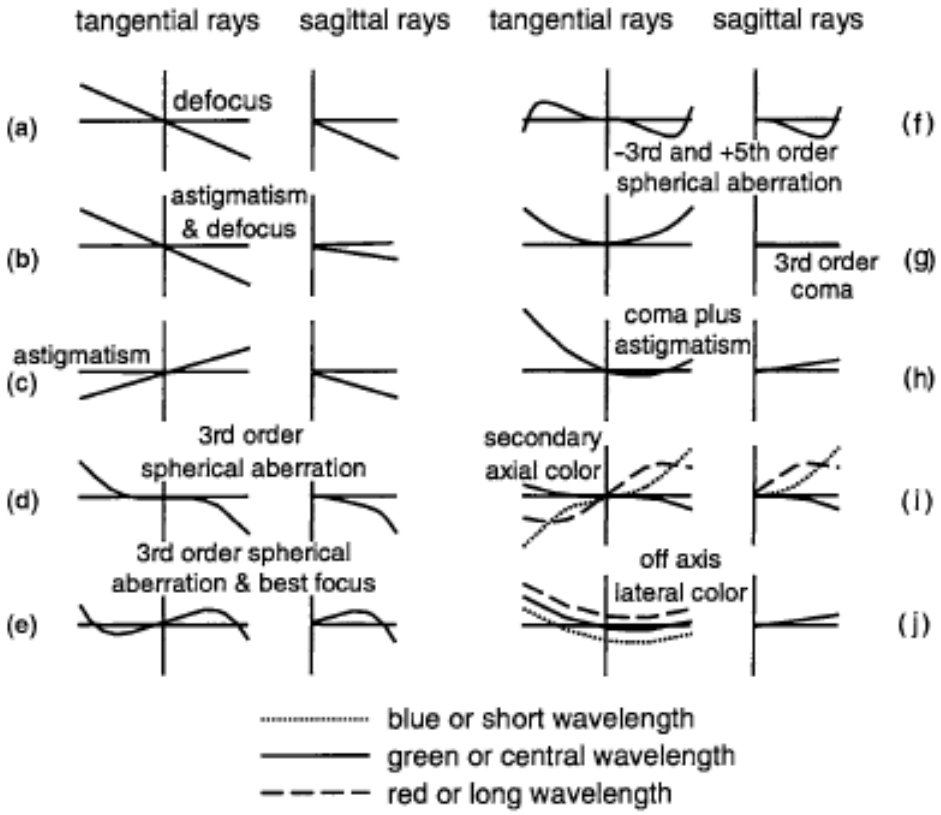

Fig. 2.10: Most typical ray aberrations curves [7]

- **Spot Diagram**: It is the geometrical image blur formed by the lens when imaging a point object [7]. This is a very informative plot, especially for systems with pixelated sensors where one wants the image of a point object to fall within a pixel, although it is sometimes

difficult to know from which aberrations the system is suffering. Usually, it is given the Root Mean Square (RMS) spot radius, which represents the radius of a circle containing 68% of the energy [7]. Figure 2.11 shows an example of spot diagram for three different fields of view (0°, 1.93°and 2.75°) and for different focus positions. It can be seen that for the focus position, that the on-axis spot size is smaller than the off-axis spot size where there are more aberrations.

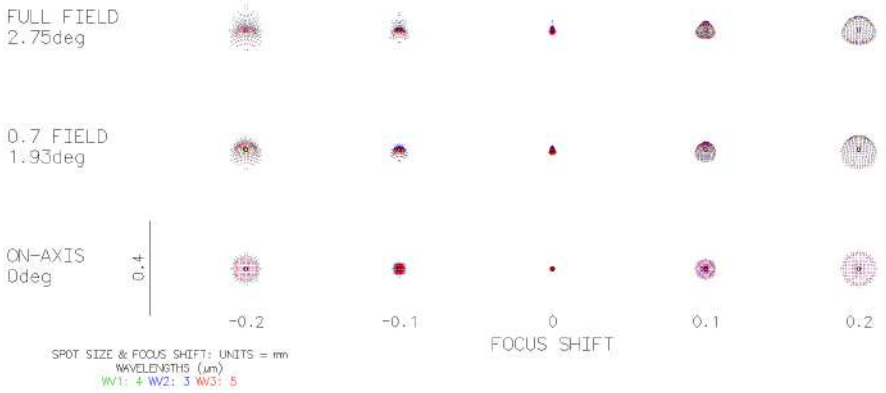

Fig. 2.11: Example of a spot diagram

- **Modulation Transfer Function (MTF)**: It represents the transfer of modulation from the object to the image by the lens as a function of spatial frequency. Because of aberrations and diffraction the image of an optical system is somewhat degraded, making the brights not that bright and the darks not that dark as the object. The modulation is defined as:

$$Modulation = \frac{I_{max} - I_{min}}{I_{max} + I_{min}} \tag{2.2}$$

Then:

$$MTF = \frac{Modulation_{image}}{Modulation_{object}} \tag{2.3}$$

Therefore, the MTF is the ratio between the modulation in image and the modulation in the object as a function of the spatial frequency, which is generally in the form of line pairs per millimeter [7]. Figure 2.12 shows a typical MTF curve. It is seen that in a real system the modulation decreases more rapidly when the spatial frequency increases than in a perfect system. The closer the MTF curve of the real system to the perfect system the better.

- **Encircled Energy**: It is the energy percentage plotted as a function of image radius. It is very useful for imaging optical system with pixeled sensors. A reliable specification is that 80% of the energy falls within the pixel size. As an example, figure 2.13 shows the energy encircled for an optical system used with a detector of 7.5 μm pixel pitch. Therefore, 80% of the energy should fall within less than 3.75 μm. It is seen that this is accomplished and so the optical system is good enough for the detector.

1.4 Typical lens systems

In this section, two different ways to get rid off chromatic aberrations are presented (see section 1.4.1 and section 1.4.2) as well as the aspheric lenses, a type of lenses used to get rid off aspherical aberrations (see section 1.4.3).

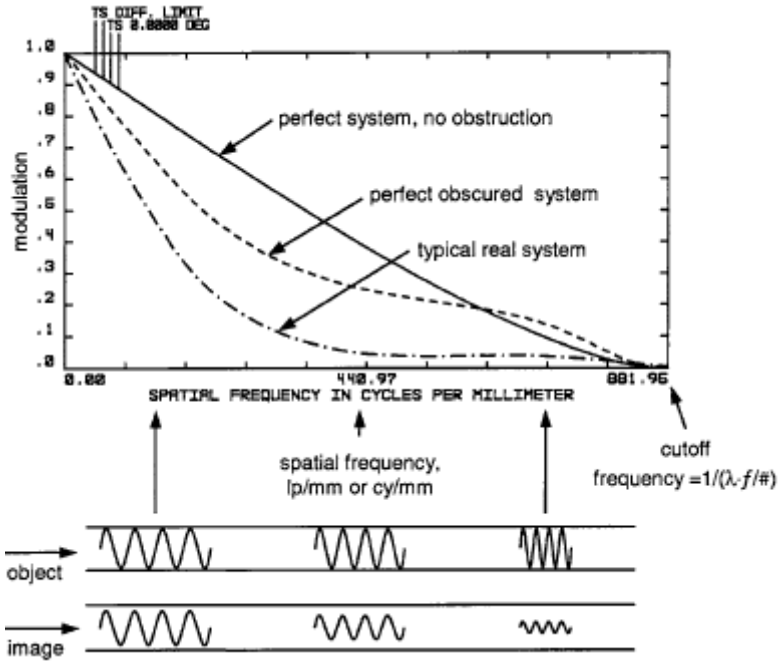

Fig. 2.12: Typical MTF [7]

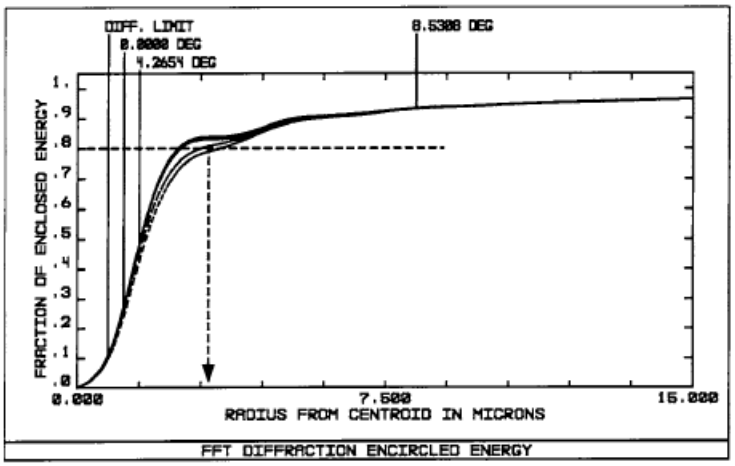

Fig. 2.13: Example of Encircled Energy plot[7]

1.4.1 The doublet achromat

The doublet achromat is designed to eliminate the chromatic spherical aberrations inherent in singlet lenses. Typically, the achromat is compound by two cemented elements, being the first one a positive (concave) element with low dispersion (property known as crown) and the second one a negative (convex) element with high dispersion (property known as flint). However, the optical cement does not transmit in the infrared bandwith, so the two elements must be separated[13] [27].

Figure 2.14 shows an schematic example of an achromatic doublet. It can be seen that the first element is concave and the second is convex. Blue and red rays represent the blue and red wavelengths, the extreme wavelengths of the visible bandwidth. It shows that both focus at the same point thanks to the combinations effects of the two lenses. The working principle in the

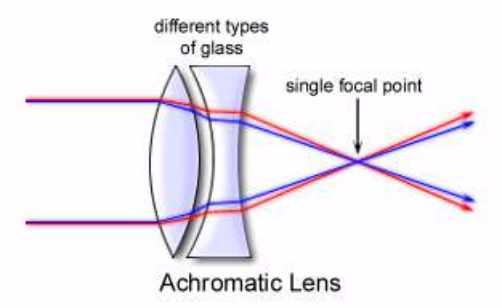

Fig. 2.14: Example of an achromatic doublet [5]

visible and in the infrared is the same, it just depends on the refractive index and transmission of the lens materials. Finally, it is important to remark that the achromatic doublet works very well on-axis but its performance is not that well off-axis.

1.4.2 Hybrid lenses

The doublet achromat is based on the combination of two elements with very different dispersion. This effect can also be achieved in one single lens by using a refractive-diffractive element.

These elements, also known as hybrid lenses, consist of a lens in which the first surface is a refractive surface meanwhile the second one uses a Diffractive Optical Element (DOE). The latter has some relief on its structure which makes a conversion of the wave front shape in a way the surface behaves as a negative element. So, the final result is that there is no need in using two lens as done with the doublet achromat because one single element achieves the desired effect to reduce the chromatic aberrations.

The use of theses lenses offers multiple advantages. First of all, hybrid achromats tend to be lighter and smaller than the conventional doublet achromat. In the infrared region they are even more advantageous because of the limited choice of materials, as well as often their high price [16]. Typically, the curvature of an hybrid lens must be smaller than the doublet achromat in order to achieve the same power and thus it eliminates the curvature barrier to high aperture achromats as well as it is easier to correct other aberrations as the curvature decreases [33].

Construction of the surface relief

As already said, the profile relief of the diffractive surface introduces a phase modulation of the light's wavefront aiming a constructive interference at the focal point. The relief construction of the lens is based on Fresnel zones. The full period Fresnel zones are spaced such that the optical path length from the edge of the j^{th} zone to the focal point is equal to $f + j\lambda$, where λ is the design wavelength and f is the desired focal length [16].

The phase function, $\varphi(r)$, can be written as

$$\varphi(r) = \frac{2\pi}{\lambda}(C_1 r^2 + C_2 r^4 + C_3 r^6 + C_4 r^8 + C_5 r^{10} + ...) \tag{2.4}$$

where r is the radial coordinate (as shown in figure 2.15) and C_1, C_2, C_3, ... the higher order phase coefficients.

Developing equation (2.4), it is possible to obtain that $C_1 = \frac{1}{2\lambda f}$ and that all the other higher terms are null, describing a parabolic blaze [16]. Similar to the way aspheric surfaces are defined (see section 1.4.3), giving value to the rest of higher order terms coefficients would correct aberrations.

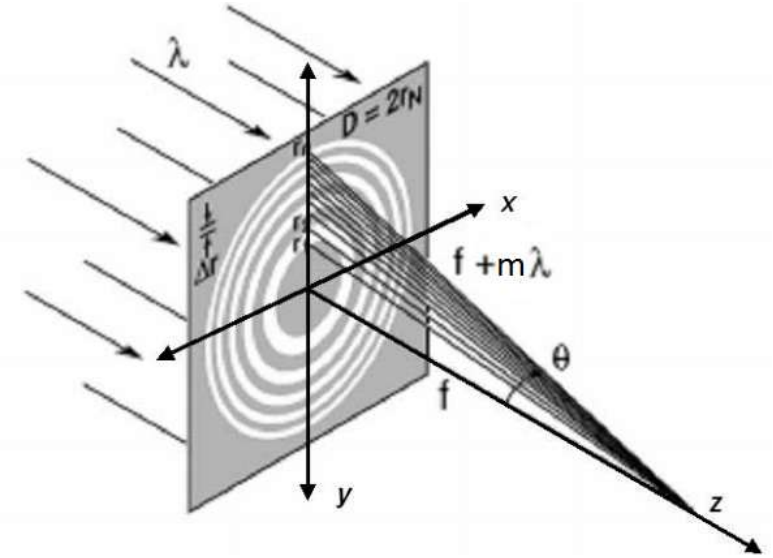

Fig. 2.15: Construction of Fresnel zones [26]

Let's divide now the lens into the different Fresnel zones.

$$\varphi(r_m) = 2\pi m \tag{2.5}$$

where m represents an integer which defines the Fresnel zone. According to figure 2.15, it is possible to state the following expressions:

$$r_m{}^2 + f^2 = (f + m\lambda)^2 \tag{2.6}$$

$$r_m = \sqrt{2fm\lambda + (m\lambda)^2} \rightarrow r_m{}^2 \approx 2fm\lambda \tag{2.7}$$

So, it is possible to say that: $r_1 = \sqrt{2f\lambda}$ and $r_m = r_1\sqrt{m}$
The maximum number of zones can be computed as follows:

$$m_{max} = \frac{R^2}{2f\lambda} \tag{2.8}$$

The depth of the zones is calculated as:

$$d_{max} = \frac{\lambda}{m-1} \tag{2.9}$$

1.4.3 Asphere surfaces

In aspheric lenses, the surface profile of these is not a portion of a sphere. This makes these surfaces often more challenging to manufacture than the conventional spherical lens due to the complex shape. However, they provide a great improvement in performance by eliminating aberrations and distortions without adding any other lens. So, this makes aspheric lenses very appropriate for our application as there the space available is reduced.

The aspheric surfaces are defined by several parameters (while spheric surfaces are only defined by one). This is because the curvature varies across the surface. An aspheric surface is usually defined by an analytical formula, although it is sometimes given in the form of a sag table for coordinate points across the surface. The sag is the the z-component of the displacement of

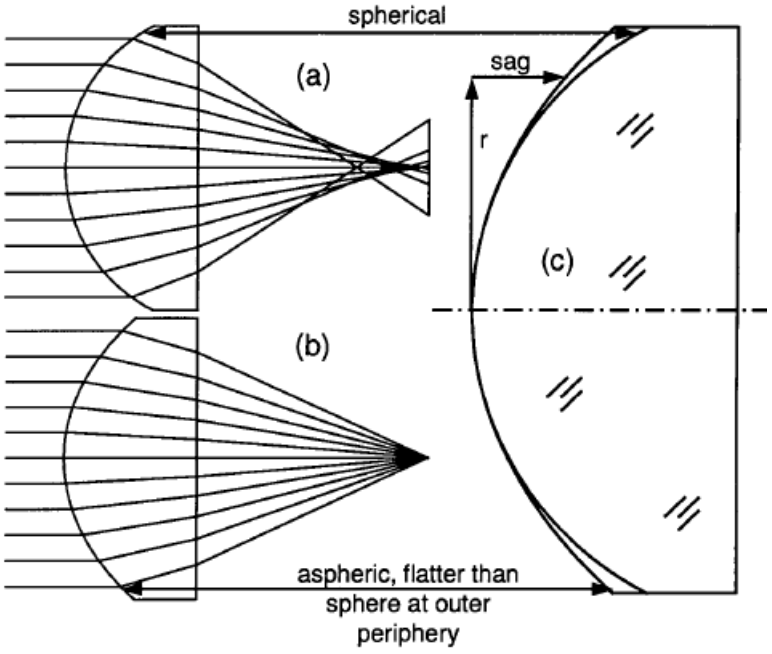

Fig. 2.16: Difference betweeen spheric and aspheric lenses [7]

the surface from the vertex, at distance r from the axis. Figure 2.16 helps both to clarify this concept and to note the difference between spheric and aspheric lenses.

There exist a lot of different shapes of aspheric surfaces. However, the most common among them is a rotationally symmetric surface with the sag defined as [7]:

$$Z(r) = \frac{c\,r^2}{1+\sqrt{(1-(1+K)c^2r^2)}} + A\,r^2 + B\,r^4 + C\,r^6 \tag{2.10}$$

where c is the base curvature at the vertex, K is a conic constant, r is the radial coordinate measured perpendicularly from the optical axis and A, B, C, ... are the higher-order aspheric terms. If these higher-order terms are null, the shape of the asphere lens will be a rotationally symmetric conic cross section.

Aspheric surfaces do not correct just spherical aberration. If the asphere surface is located at or near the aperture stop, it will primarly correct the spherical aberration. If the aspheric surface is located further away from the aperture stop, it can also help to minimize some off-axis aberrations such as coma or astigmatism.

2 The detector

Infrared detectors are broadly classified into thermal detectors and quantum detectors. Thermal detectors use the infrared energy as heat and their photo sensitivity is independent of wavelength. They do not require cooling but the response time is slow and detection capability is low. In contrast, quantum detectors offer higher detection performance and a faster response speed but their photo sensitivity is dependent on wavelength and some of them need to be cooled for accurate measurement [11].

Regardless of the detector type, it is important that it has a high Signal to Noise Ratio (SNR). The SNR compares the level of the desired signal to the level of background noise. In

[27], the signal-to-noise ratio is defined as:

$$SNR = \frac{P}{NEP} \tag{2.11}$$

where P is the collected radiant power in Watts (W) received by the detector and NEP is the Noise-Equivalent Power, a measure of the minimum signal that yields a unity signal to noise ratio, also expressed in W.

The power can be calculated as:

$$P = \frac{d_n d_m}{4(f/\#)^2} W \tag{2.12}$$

where d_n and d_m are the detector linear dimensions in the n and m directions respectively and I is the radiant emittance. The radiant emittance is defined as the radiated power in W/m^2 from a flat diffuse source surface into a hemisphere. The relationship between the radiant emittance and the radiance, L, is $L = W/\pi$.

On the other hand, the noise-equivalent power is a function of the detector characteristics:

$$NEP = \frac{\sqrt{d_n d_m}\sqrt{\Delta f}}{D^*} \tag{2.13}$$

where Δf is the bandwidth used in the measurement, measured in Hz, and D^* is the specific detectivity (defined as the signal-to-noise ratio when 1 W is incident on a detector having a sensitive are of 1 square centimeter and the noise is measured with an electrical bandwidth of 1 Hz), expressed in cm $Hz^{1/2}/W$. Combining equation (2.12) and equation (2.13) into equation (2.11) yields:

$$SNR = \frac{D^*\sqrt{d_n d_m}W}{4(f/\#)^2\sqrt{\Delta f}} \tag{2.14}$$

3 Radiance reaching the detector

The irradiance that a MWIR camera observing the Earth from the space receives comes from two sources. On one hand, the Earth's reflects the irradiance from the Sun (which emits as a black body at 5900 K) and, on the other hand, the Earth also emits radiation. All this reflected and emitted radiance does not reach the detector because the atmosphere is not totally transparent to the infrared light and the lenses of the optical system have some reflectance and absorptance. In the following lines, it is going to be studied the quantity of irradiance that reaches the detector by studying the atmosphere transmission, the radiance that the Earth emits and reflects and the lens transmission.

3.1 Atmosphere Transmission

The complex composition of the atmosphere makes its transparency dependent on the wavelength. Among the different gases present in the atmosphere, the major absorbent gases in MWIR bandwidth are water vapor (H_2O), carbon dioxide (CO_2) and nitrogen oxide (N_2O). Due to the absorption of these components in different wavelengths the transmission is not uniform along the MWIR bandwidth. In [8] a transmission model was presented (see equation (2.15) and figure 2.17).

$$\tau(\lambda) = \begin{cases} 1.125\lambda - 3.375 & \text{if } 3\mu\text{m} \leq \lambda \leq 3.4\mu\text{m} \\ 0.75 & \text{if } 3.4\mu\text{m} \leq \lambda \leq 4.2\mu\text{m} \\ 0 & \text{if } 4.2\mu\text{m} \leq \lambda \leq 4.4\mu\text{m} \\ -0.8817\lambda + 4.6129 & \text{if } 4.4\mu\text{m} \leq \lambda \leq 5\mu\text{m} \end{cases} \tag{2.15}$$

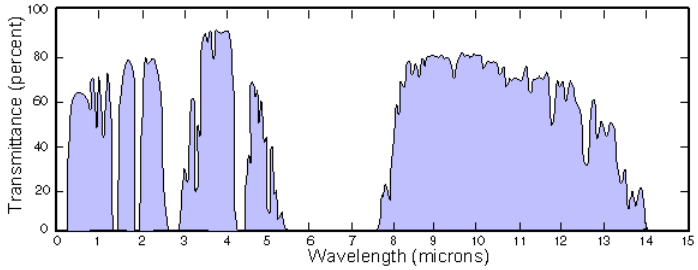

(a) Real transmission of the atmosphere [37]

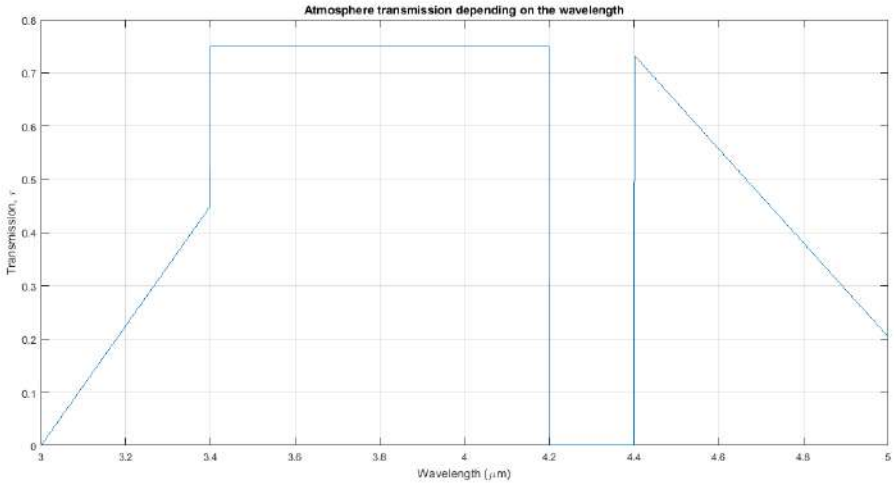

(b) Modeled transmission of the atmosphere along the MWIR bandwidth

Fig. 2.17: Atmosphere transmission

3.2 The radiance

3.2.1 Reflection of Sun's radiance

The spectral radiance emitted ($L(\lambda, T)$ in W/(m^{2}sr m)) by a black body can be computed using Planck's law [22]:

$$L(\lambda, T) = \frac{2hc^2}{\lambda^5(e^{\frac{hc}{\lambda kT}} - 1)} \tag{2.16}$$

where $h = 6.62607004 \cdot 10^{-34} Js$ is the Planck's constant, $c = 3 \cdot 10^8 m/s$ is the light's speed, $k = 1.38064852 \cdot 10^{-23} J/K$ is the Boltzmann constant, λ is the radiation wavelength and T is the temperature of the emitting black body [21].

The Sun can be approximated as a black body emitting at 5772 K [6]. Therefore, the amount of power emitted along the spectrum by the Sun per unit area and per steradian can be computed using equation (2.16). At this temperature, the maximum energy emitted corresponds to the visible bandwidth. However, the power emitted in the MWIR can not be neglected.

In this work, it is assumed that the Sun emits homogeneously in all directions. From all this emitted radiation, only a portion of the power emitted will reach the Earth, corresponding to the solid angle of the Sun seen from the Earth. Since the dimension of the Earth with respect to the Sun is small and the distance between both is large, it is possible to approximate the

Earth as a point. Then, the solid angle is given by equation (2.17):

$$\Omega_{S,E} = \frac{A_s}{d_s^2} \tag{2.17}$$

where A_s is the area of the Sun ($A_s = \pi R_s^2$, being R_s the Sun's radius) and d_s is the distance between the Sun and the Earth, as shown in figure 2.18. The distance d between the Sun and the Earth is $d = 1.5 \cdot 10^{11}$ m and the radius of the Sun is $R_s = 7 \cdot 10^8$ m.

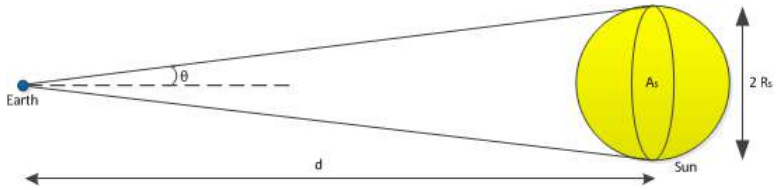

Fig. 2.18: Sketch of the Sun solid angle seen from the Earth

Therefore, the spectral emittance that the Earth receives from the Sun, in W/(m$_2$ m), is:

$$L_{S,Earth}(\lambda) = L(\lambda, T_s)\Omega_{s,E} \tag{2.18}$$

If the spectral emittance is integrated along the bandwidth, the irradiance that reaches the Earth from the Sun is obtained. However, not all of this irradiance arrives at the Earth's ground after passing through the atmosphere. Then, a small part of it is reflected and goes to the outer space, passing again through the atmosphere and reaching OUFTI-NEXT.

About the Earth's reflection of Sun's radiance, it is important to notice that the Earth's reflectance is not homogeneous because of the ground composition variability. However, in [8] the reflection coefficient is estimated as $\rho_g = 0.05$ based on an average of the ground composition. Since the reflection only occurs at one of the Earth's hemispheres (the illuminated one in that moment), the reflected radiance must be divided per a solid angle equal to π sr.

Combining all these equations, the radiance coming from the Sun and reflected by the Earth that reaches the detector can be computed using equation (2.19).

$$L_{S,det}(\lambda) = L_{S,Earth}(\lambda)\tau_a(\lambda)^2\frac{\rho_g}{\pi} \tag{2.19}$$

Figure 2.19 shows a graphic of the energy (W/cm$^2\mu$m) that reaches the detector due to the Earth's reflection of Sun's radiance.

3.2.2 Earth's radiance

The Earth cannot be considered a black body but a grey body. Grey bodies have a constant emissivity coefficient in all wavelengths and temperatures. In the case of the Earth's ground, the emissivity coefficient is ε_g=0.8.

The spectral radiance can be computed similarly as done to the Sun's (equation (2.20)). Since the temperature is not constant, the radiance will be dependent of both the wavelength and the temperature. The range of temperatures considered (temperatures at which crop fields are supposed to be) varies from 270 K to 320 K.

$$L_{E,emit}(\lambda, T_g) = \frac{2hc^2\varepsilon_g}{\lambda^5(e^{\frac{hc}{\lambda k T_g}} - 1)} \tag{2.20}$$

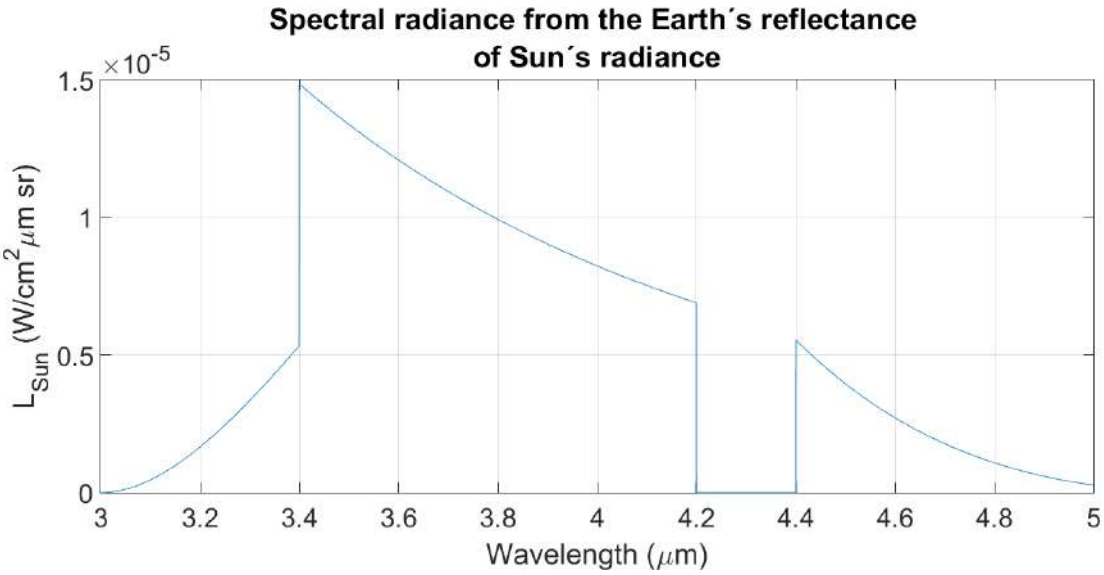

Fig. 2.19: Spectral radiance coming from the Earth's reflectance of Sun's radiance

However, the whole irradiance that will reach the detector is not given by equation (2.20) because the atmosphere transmissivity must be taken into account. Therefore, the radiance from the Earth's ground after going through the atmosphere is:

$$L_{E,det}(\lambda) = L_{E,emit}\tau_a(\lambda) \tag{2.21}$$

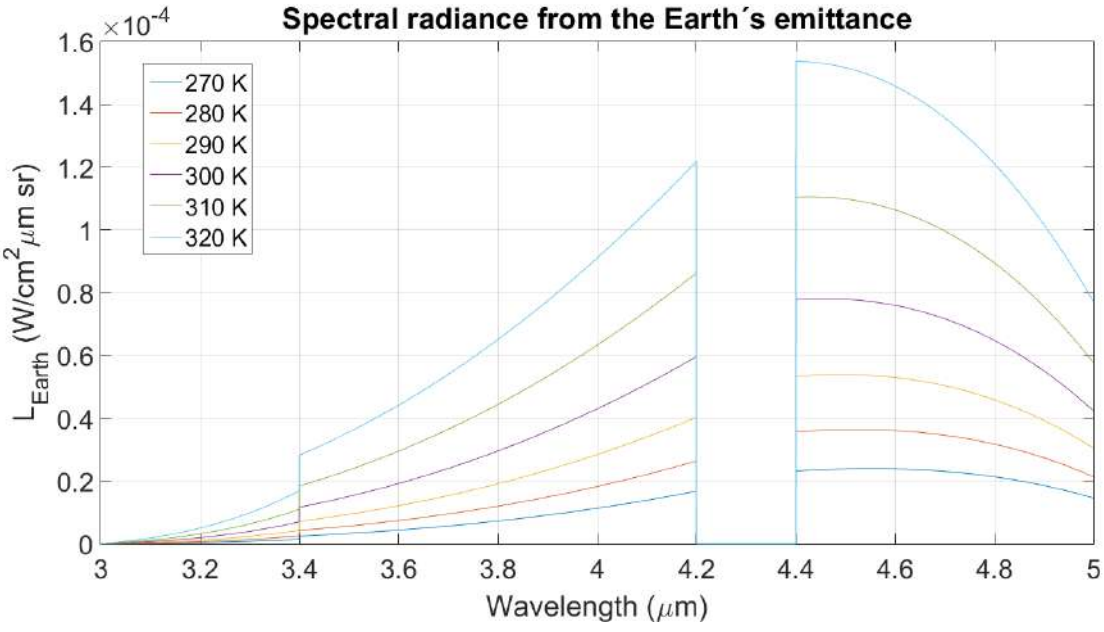

Fig. 2.20: Spectral radiance from the Earth's ground emittance

As seen in figure 2.20, the radiation emitted increases with Earth's ground temperature. It is also remarkable that the reflected energy by the Earth coming from the Sun is about ten times smaller than the Earth's radiance. The reason of this lays on the fact that the energy

peak of the Earth's ground temperature corresponds to the MWIR while the energy peak of the Sun corresponds to the visible bandwidth. Figure 2.21 shows the total spectral radiance (in W/cm$^2\mu$m sr), which is the contribution of both Sun's radiance reflected by the Earth and the Earth's radiance. Table 2.1 shows the values of the total radiance.

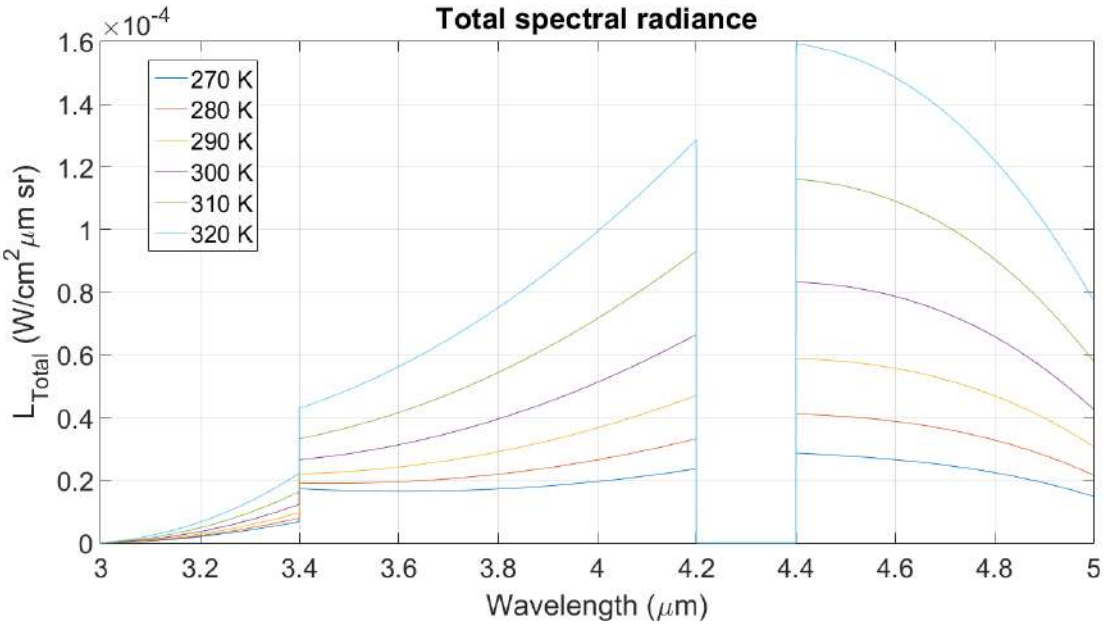

Fig. 2.21: Total spectral radiance

Table 2.1: Total radiance for different temperature values

Temperature	Total radiance (W/m$_2$ sr)
270	0.2991
280	0.4065
290	0.5595
300	0.7724
310	1.0621
320	1.4485

3.3 Lens transmission

When light passes through a glass, not all of the light is transmitted: some part is reflected and some part is absorbed. Regarding reflection and due to the fact that a lens has two surfaces, internal reflections occur causing disturbances because they generate secondary or *ghost* images [12]. Figure 2.22 shows a sketch of what happens in terms of reflection and refraction in a substrate with plane-parallel surfaces (which is similar to what happens in a lens).

If internal reflections are ignored, the transmittance, τ, through the substrate can be expressed as follows [27]:

$$\tau = \left(\frac{4n}{(n+1)^2}\right)^2 \tag{2.22}$$

where n is the refraction index of the material. Therefore, the higher the refractive index (which is usually the case for infrared materials) the lower the transmittance. As an example, the

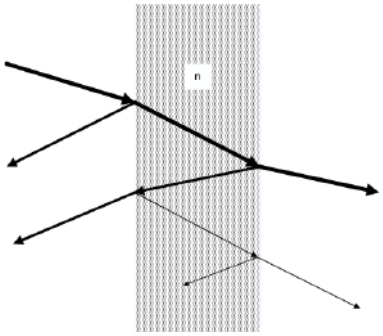

Fig. 2.22: Transmission and reflection at a plane-parallel substrate [27]

refractive index for Silicon at 4μm is 3.42 [25]. With this, $\tau = 0.49$. By itself, this is already a very low value. In addition, the overall transmittance of the system would be even lower given that more than one silicon lens will be needed to correctly collect the power on the detector.

In order to increase the lenses transmission, Anti-Reflection (AR) Coatings are used. These coatings increase the transmittance of the lens up to 95% for a specific bandwidth. Following the example of the silicon lens, figure 2.23 shows the transmittance of a silicon lens in the MWIR when coated on both surfaces [34]. It can be seen that the transmittance is not lower than 0.95 at this bandwidth.

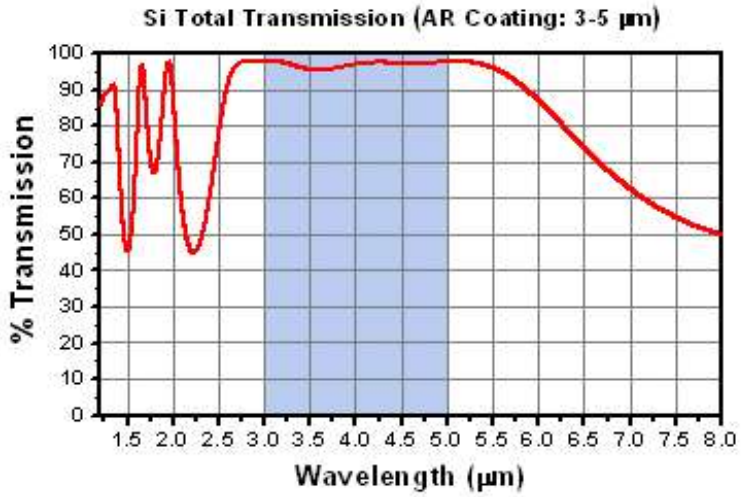

Fig. 2.23: Transmittance of a coated silicon lens [34]

Apart from the reflection, lens materials have also an absorptance. The attenuation of the radiance can be calculated by applying the Beer-Lambert law:

$$L = L_0 e^{-\alpha x} \tag{2.23}$$

where L_0 is the intensity of the radiance before entering the lens, L is the intensity of the radiance after passing through the lens, α is the absorptivity coefficient which depends on the material and x is the thickness of the material.

Therefore the total spectral radiance reaching the detector is:

$$L_T(\lambda) = (L_{S,det}(\lambda) + L_{E,det}(\lambda))\tau_{AR} e^{-\alpha x} \tag{2.24}$$

where τ_{AR} is the transmittance given by the manufacturer after applying the AR coating.

Chapter 3

Optical system parameters

The purpose of this chapter is to specify the parameters of the optical system to fulfill the thermal imaging system requirements. Therefore, before setting up the working parameters, it is necessary to do a parametric study with all the parameters that affect the thermal imaging system:

- Altitude, H: The orbit altitude of the satellite. It won't be known until some time before the launch but it is supposed to be between 400 and 800 km.
- Ground Sample Distance, GSD: It is the ground distance that can be measured in one pixel. It should be smaller than 100 m in order to have useful information on the crop fields.
- Field of View, FoV: Angular aperture of the detector beam.
- Instantaneous Field of View, Instantaneous Field of View (iFoV): Field of view of a single pixel.
- Effective focal length, EFL: effective focal length of the optical system.
- F-number, $f/\#$: ratio of the system's focal length to the diameter of the entrance pupil, $f/\# = \frac{EFL}{D_p}$
- Pixel size, ps: Size of the detector's pixels.
- Number of pixels, n and m: Number of pixels per row and column in the detector array.
- Signal to Noise Ratio, SNR: Measure that compares the level of a desired signal to the level of background noise. Its value gives direct information on the real possibility to obtain useful thermal information from the ground, the range of detectable temperatures and the thermal resolution.

Almost all parameters listed above are still not known as the project is at an initial design stage. However, some of them are already constrained. Although the detector is still not chosen, it is known it will have a pixel size of 15 μm and an array of 640 $\times$ 512 ($n \times m$). Moreover, the uncertainty of the final orbit of the satellite forces to design an optical system capable of working in the overall altitude range defined (400-800 km).

Here below a parametric study is done in order to understand how the whole system will work. By doing this, it will be possible to determine the parameters of the optical system so that the thermal imaging system has a good performance.

1 Parametric study

The lens configuration must be the appropriate so that each GSD's power concentrates in each detector's pixels. The GSD and the pixel size can be related by the optical system by means of its EFL. Figure 3.1 shows a sketch of the relation between these parameters at the nadir. The Earth's curvature is considered negligible. From figure 3.1 the following expression can be stated:

$$GSD = \frac{ps}{EFL} H \tag{3.1}$$

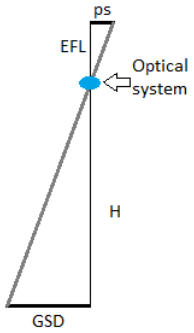

Fig. 3.1: Sketch of the relation between GSD, satellite altitude, EFL and pixel size (please, note that it is not proportional)

The FoV determines the total coverage area given that it is the angle through which the system (detector) is able to collect the power. If only one pixel is considered instead of the whole detector, then it is possible to relate the pixel size with the GSD by the iFoV using:

$$iFoV = \arctan\left(\frac{ps}{EFL}\right) \tag{3.2}$$

Once the iFoV is known, the full field of view can be computed taking into account the number of pixels of the detector. The number of columns and rows of the detector is not the same, so the FoV will be different in both directions. Being m the number of pixels in the considered direction, the Field of View is:

$$FoV = m \cdot iFoV = m \cdot \arctan\left(\frac{ps}{EFL}\right) \tag{3.3}$$

Finally, the total coverage area, the swath (SW), can be easily computed in one direction (in km) as follows:

$$SW = \frac{m \cdot GSD}{1000} \tag{3.4}$$

Since the detector is a 2D Focal Plane Array (FPA) where the number of pixels is different in its two dimensions, the shape of the total area covered is rectangular.

The camera collected data will not be useful to monitor the crop fields unless the GSD is 100 meters or smaller. Figure 3.2 shows the obtained value of GSD for different EFL at different altitudes, a high EFL (120 mm) is required in order to fulfill the GSD specification for all the altitudes.

The ground sample distance, the swath and the field of view have been calculated for different orbit altitudes and effective focal lengths (see table 3.1). As expected, the larger the EFL the smaller the GSD and the field of view. If the FoV is small, it will be easier that the

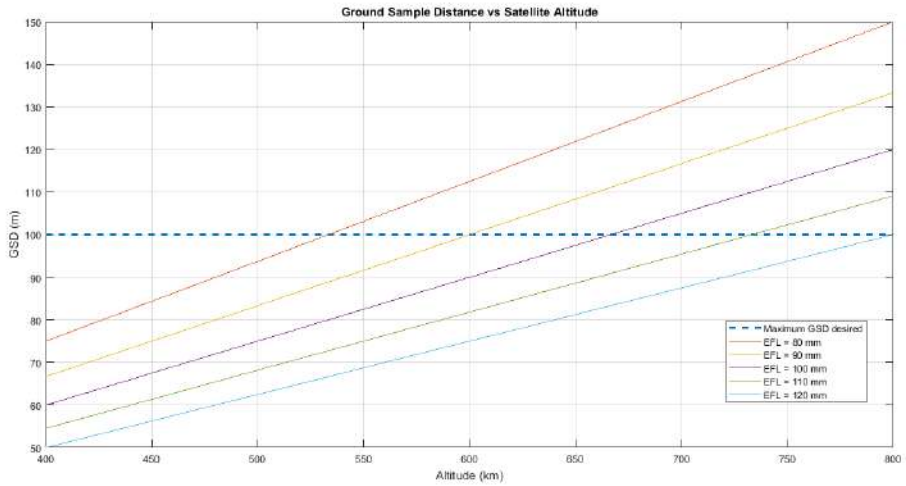

Fig. 3.2: GSD versus Satellite Altitude for different EFL values

Table 3.1: GSD, FoV and swath for different altitudes and different effective focal lengths

	EFL = 80 mm			EFL = 90 mm		
	FoV_n = 6.9°; FoV_m = 5.5°			FoV_n = 6.1°; FoV_m = 4.9°		
H (km)	GSD (m)	SW_n (km)	SW_m (km)	GSD (m)	SW_n (km)	SW_m (km)
400	75	48	38.4	66.67	42.67	34.13
500	93.75	60	48	83.33	53.33	42.67
600	112.5	72	57.6	100	64	51.2
700	131.25	84	67.2	116.67	74.67	59.73
800	150	96	76.8	133.33	85.33	68.27
	EFL = 100 mm			EFL = 110 mm		
	FoV_n = 5.5°; FoV_m = 4.4°			FoV_n = 5°; FoV_m = 4°		
H (km)	GSD (m)	SW_n (km)	SW_m (km)	GSD (m)	SW_n (km)	SW_m (km)
400	60	38.4	30.72	54.55	34.91	27.93
500	75	48	38.4	68.18	43.64	34.91
600	90	57.6	46.08	81.82	52.36	41.89
700	105	67.2	53.76	94.45	61.09	48.87
800	120	76.8	61.44	109.09	69.82	55.85

optical system has a good performance in all of its points. Thus, if only these parameters were to be taken into account, it could be concluded that the EFL should be as large as possible.

However, the EFL is upper limited by its relation with the $f/\#$ (remember that $f/\# = \frac{EFL}{D_p}$). On one hand, $f/\#$ and the SNR are related inversely proportional to the square (see equation (2.14)). Therefore, to increase SNR as much as possible, $f/\#$ must be as small as possible and so the EFL. On the other hand, $f/\#$ also plays a role in the diffraction limitation of the system. When introducing the design wavelength (λ=4 μm) and the pixel size (B_{diff}=15 μm) in equation (2.1) it is obtained a value of $f/\# \leq 1.54$. Therefore, both the SNR and the diffraction limit add an upper restriction to the EFL.

2 Optical System's parameters

After studying the contribution of the most relevant parameters that influence the thermal imaging system's performance, it is now possible to determine the optical system's design parameters that will lead to a good performance of the thermal imaging system.

So that the thermal information obtained from the crop field is useful, the GSD must be as low as possible, having a maximum value of 100 m. This can only be achieved for the overall range of altitudes if the EFL is 120 mm or longer. The following paragraphs study the viability of this restriction.

Since the system is designed for the infrared bandwidth, the diffraction limit constraint is very limiting. Taking this condition into account, it has been obtained $f/\# \leq 1.54$. This would force the system to have a pupil diameter of approximately 78 mm, which is feasible given the CubeSat face dimensions (10 $\times$ 10 cm). Regarding the space along the optical axis, it can not exceed 12cm (10 cm of 1U plus 2 cm of extra space). There is not any exact relation between the EFL and the overall length of the system. However, the system tends to occupy more space than the EFL value when there is more than one lens . Then, in order to avoid space problems which would make the system too big for OUFTI-NEXT, the EFL is going to be fixed at 100 mm. This decision directly affects the altitude range, which must be reduced to 400-650 km (see table 3.1).

By applying the diffraction limit condition, the entrance pupil diameter can be easily obtained: D_p=65 mm. It is important to remark that it is quite difficult to obtain a good geometrical aberrations performance with a $f/\#$ of 1.54 for a simple configuration of just two or three lens because, in general, the smaller the $f/\#$ the more difficult it is to minimize the geometrical aberrations. For this reason, the first designs are going to be made with D_p=60 mm in order to find a compromise between geometrical aberrations and diffraction limit. If the design is good enough in terms of geometrical aberrations, the entrance pupil diameter will be increased until 65 mm.

Finally, the FoV can be obtained by applying equation (3.2) and equation (3.3) in both directions (n and m). Table 3.2 shows a summary of the optical system design parameters.

Parameter	Value
$\Delta\lambda$	3-5 μm
EFL	100 mm
FoV_n	5.5°
FoV_m	4.4°
D_p	60 mm

Table 3.2: Design values of the optical system

Chapter 4

Materials

While in the visible bandwidth it is possible to choose among a wide range of different materials, only a small set of materials are available in the infrared bandwidth because most of the materials used in the visible are not transparent in the infrared.

1 Analysis of possible materials

In table 4.1, a list of different materials transparent in the MWIR and their most important properties is presented.

Properties	n (@ 4 μm)	dn/dT	Thermal expansion coefficient	Solubility
Barium Fluoride (BaF_2) [36]	1.455	$-15.2 \cdot 10^{-6}$/K	$18.1 \cdot 10^{-6}$/°C @ 20 °C	$0.17 g/100 cm^3$
Cadmium Telluride ($CdTe$) [36]	2.693	$5 \cdot 10^{-5}$/K	$5.9 \cdot 10^{-6}$/°C @ 20 °C	Insoluble
Calcium Fluoride (CaF_2) [36]	1.4096	$-11 \cdot 10^{-6}$/K	$18.85 \cdot 10^{-6}$ /°C	$0.0016 g/cm^3$
Cesium Bromide ($CsBr$) [36]	1.668	$79 \cdot 10^{-6}$ /°C	$47.9 \cdot 10^{-6}$ / °C	Soluble
Cesium Iodide (CsI) [36]	1.743	$-99 \cdot 10^{-6}$/ °C @ 0.6 μm	$50 \cdot 10^{-6}$ /°C	Soluble
AMTIR 1 [36]	2.513	$71 \cdot 10^{-6}$ /K	$12.1 \cdot 10^{-6}$ /K	Insoluble
Gallium Arsenide ($GaAs$) [36]	3.307	$148 \cdot 10^{-6}$ /K	$6 \cdot 10^{-6}$ /K	Insoluble
Germanium (Ge) [36]	4.025	$396 \cdot 10^{-6}$ /K	$2.3 \cdot 10^{-6}$/ K @ 100 K	Insoluble
Lithium Fluoride (LiF) [36]	1.349	$-12.7 \cdot 10^{-6}$/ °C @ 0.6 μm	$37 \cdot 10^{-6}$/ °C	$0.27 g/cm^3$
Magnesium Fluoride (MgF_2) [36]	1.349	$2 \cdot 10^{-6}$ / °C @0.4 μm	$13.7 \cdot 10^{-6}$/ °C	$0.0076 g/cm^3$
Potassium Bromide (KBr) [36]	1.535	$-40.83 \cdot 10^{-6}$/ °C	$43 \cdot 10^{-6}$/ °C	Soluble in water
Potassium Chloride (KCl) [36]	1.472	$-33.2 \cdot 10^{-6}$/ °C	$36 \cdot 10^{-6}$/ °C	Soluble in water
Potassium Iodide (KI) [19]	1.6268	$-50 \cdot 10^{-6}$/ °C	$43 \cdot 10^{-6}$ /K @ 298 K	$127.5 g/100 g water$ @ 273 K
Sapphire (Al_2O_3) [36]	$n_o = 1.768$ $n_e = 1.760$	$13 \cdot 10^{-6}$/ K	$8.4 \cdot 10^{-6}$/ °C	$10^{-6} g/cm^3$
Silicon (Si) [36]	3.4289	$160 \cdot 10^{-6}$/ K	$2.55 \cdot 10^{-6}$ / °C @25 °C	Insoluble
Sodium Chloride ($NaCl$) [36]	1.522	$-36 \cdot 10^{-6}$ / °C @0.7 μm	$44 \cdot 10^{-6}$/ °C	Soluble in water
Thallium Bromoiodide ($KRS-5$) [36]	2.382	$-235 \cdot 10^{-6}$/ °C	$58 \cdot 10^{-6}$/ °C	$0.05 g/100 cm^3 H_2O$ @20 °C

Zinc Selenide ($ZnSe$) [36]	2.4332	$62 \cdot 10^{-6}$/K @3.39 μm	$7.1 \cdot 10^{-6}$/K @273 K	Insoluble
Zinc Sulfide (ZnS) [36]	2.252	$38.5 \cdot 10^{-6}$/K @3.39 μm	$6.3 \cdot 10^{-6}$/K @273 K	$65 \cdot 10^{-6} g/cm^3$
Silver Chloride (AgCl) [19]	1.9998	$-61 \cdot 10^{-6}$/ °C	$31 \cdot 10^{-6}$/K @302 K	$52 \cdot 10^{-6}$/ 100g water @50 °C

Table 4.1: Material Properties

The list of materials available in the MWIR is relatively large. However, some of the materials must be discarded due to their high solubility in water. This is because the lenses will have to be polished in order to have a good performance and this process includes water. Therefore, the lenses could not be polished or they would dissolved when polishing. In order to avoid any problem when polishing, the solubility in water of the materials should be smaller than 10^{-3}g/cm^3 H_2O, which significantly reduces the potential materials list.

The materials that can be used taking this constraint into account for the design are: Cadmium Telluride, Calcium Fluoride, AMTIR-1, Gallium Arsenide, Germanium, Magnesium Fluoride, Sapphire, Silicon, Zinc Selenide, Zinc Sulphide and Silver Chloride. Some extra properties or qualities of these materials are:

A more detailed description of the properties of these materials will be made in the following lines with the aim of analyzing if some of them have other undesired characteristics for our design.

- **Cadmium Telluride, CdTe**:
  Extra handling and safety precautions are required when machining it due to its toxicity. Thus, few companies use it to manufacture lenses. It has one of the highest density of the common infrared materials and it is more expensive than Ge and ZnSe. It is main advantage is that it can also be used in the LWIR bandwidth, where other materials can not be used. However, this characteristic is not of our interest. It is diamond turnable and aspheric lenses can be manufactured with this material.

- **Calcium Fluoride, CaF_2**:
  It has a good transmission in a wide range of bands, from UV to MWIR. It is also diamond turnable and it can be manufactured as aspheric lenses.

- **AMTIR-1**:
  Its composition is 33% Ge, 12% As and 55% Se and it belongs to the family of chalcogenide materials. These materials are optimized for pairing with other IR materials in optical designs. Compared to other materials used in the IR, it has a low dn/dT which makes athermalization of the optical system easier than when using other materials. It can be diamond turnable and manufactured as aspheric lenses as well as diffractive lenses.

- **Gallium Arsenide, GaAs**:
  It is very similar to Ge in hardness, strength and density but it is generally more expensive. It is commonly used in applications where hardness and durability are important. It is diamond turnable and it can be manufactured as aspheric lenses.

- **Germanium, Ge**:
  It has the highest index of refraction among all the materials commonly used in IR. However, it has a high dn/dT, which makes athermalization a difficult issue. In fact, transmission degradation starts at around 100°C and it is a big issue when temperature is around 200°C. It is usually less expensive than ZnSe and ZnS. It is diamond turnable and it can be manufactured as aspheric and diffractive lenses.

- **Magnesium Fluoride, MgF_2**: It has one of the lowest index of refraction for the IR . It is a birefringence material, which must be taken into consideration when manufacturing lenses with this material. It is resistant to thermal and mechanical shock. It is diamond turnable and so aspheric lenses can be manufactured with this material.

- **Sapphire, Al_2O_3**:
  As well as Magnesium Fluoride, it is also a birefringent material. It has low dn/dT, which makes athermalization easier. It is one of the hardest and most durable optical material.

It is not diamond turnable, so it is difficult to polish and to generate aspheric surfaces with it.

- **Silicon, Si**:
  It is one of the most used materials in IR bandwidth. Silicon itself is not very expensive. However it becomes an expensive material when it comes to manufacture it because of its hardness. It is diamond turnable and aspheric and diffractive lenses can be manufactured with it.

- **Zinc Selenide, ZnSe**:
  It has a wide transmission range. It has a high resistance to thermal shock. It is not a very hard material, but some coatings can be used to protect it. Its cost is similar than the one of ZnS and higher than the one of Ge. It is diamond turnable and it can be manufactured as aspheric lenses as well as diffractive.

- **Zinc Sulphide, ZnS**:
  Zinc Sulphide is used in two forms: Clear Grade and Regular Grade. The Clear Grade is purified so that it transmits homogeneously from VIS to LWIR spectral regions. So, for our application it is better to use the Clear Grade as the absorption is lower in the MWIR bandwidth. ZnS Clear Grade is one-third harder than ZnSe. It is diamond turnable and, so, aspheric lenses and diffractive lenses can be manufactured.

- **Silver Chloride, AgCl**:
  It is not a very hard material, so it is easy to polish. However, it can be deformed under heat and pressure.

After analyzing this list of materials, it can be concluded that any of these, except for the Sapphire which is not turnable making and therefore it is not possible to produce aspheric lenses, can be used to build the optical lenses of the system.

2 Abbe diagram

The Abbe diagram gives information about the dispersion of the material and it is very helpful when designing achromat doublets. It consists of plotting the Abbe number (V-number) of a material versus its refractive index. The Abbe Number is expressed as:

$$\mathrm{V-number} = \frac{n-1}{n_S - n_L}, \tag{4.1}$$

where n is the refractive index at the middle wavelength and n_S and n_L are the refractive index of the shortest and longest wavelength of the optical system. The lower the V number, the higher the dispersion of the material. Figure 4.1 shows an Abbe diagram of the considered materials.

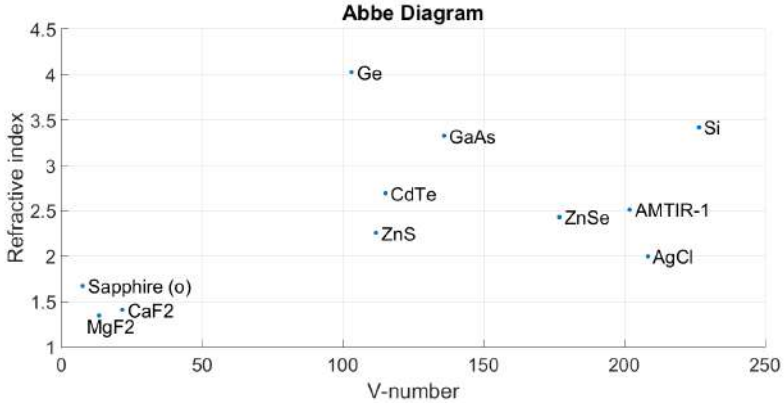

Fig. 4.1: Abbe Diagram of the available materials for the optical design

Chapter 5

Camera optical design and layout solutions

The simplest solution configuration of an optical system is the singlet lens. However, this configuration would not be enough for our system as it would not reduce the aberrations down to a desired level. The final solution for our system must be simple at the same time that it reduces the spot size down to the pixel size.

Therefore, the procedure followed to find the best solution is to start by the simplest optical system and see if it is enough to fulfill the requirements. If not, another lens will be added. And so on until finding a configuration that will perform as desired. This procedure will ensure that the found solution will be the simplest. Moreover, the use of hybrid lenses will be also studied. It will be seen that hybrid lenses might allow to achieve the performance of two lenses with only one lens. Therefore, using this relatively new technology helps to keep simplicity in the design.

The software used for the optical design is *Code V* [31]. This program allows the user to optimize an already existing optical design. Therefore, before starting optimizing with *Code V*, it is necessarily to do a literature research in order to find a good starting point for the optimization of the optical design.

1 State of the art

The goal of the state of the art is to find some optical configurations with similar characteristics than the ones required for the optical system (summarized in table 3.2). After a deep research not only refractive systems have been found but also reflective systems. The most interesting configurations are presented below.

1.1 Reflective systems

Concerning a reflective solution, there are two interesting designs for the camera. The first one is Cassegrain telescope (see figure 5.1) [30] and the second one is the Three Mirror Anastigmat (TMA) (see figure 5.2) [20].

Cassegrain telescope has a parabolic primary mirror and a hyperbolic secondary mirror. The secondary mirror reflects the light back through a hole in the primary (see figure 5.1). It works quite well on-axis but the aberrations considerably increase with the field of view. However, there exist some improved configurations that use this one as a base, such as the Schmidt-Cassegrain configuration which uses also refractive elements [30].

The TMA uses three mirrors in order to reduce the three main aberrations: spherical aberration, coma and astigmatism (remember there is no chromatic aberration in reflective

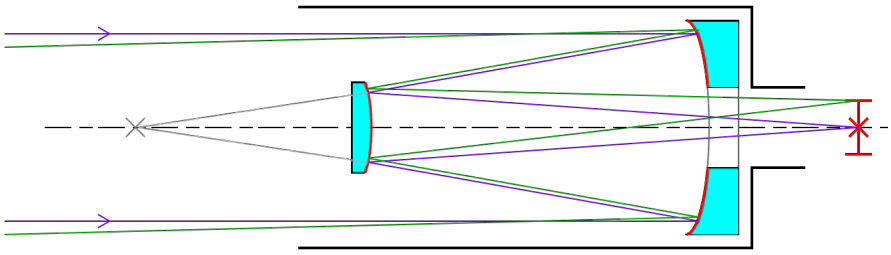

Fig. 5.1: Cassegrain configuration [37]

systems). This allows to use wider fields of views than with the Cassegrain configurations. However, it has the disadvantage that the detector is placed between the mirrors (see figure 5.2), which makes the cooling of the detector complicated (and maybe not feasible).

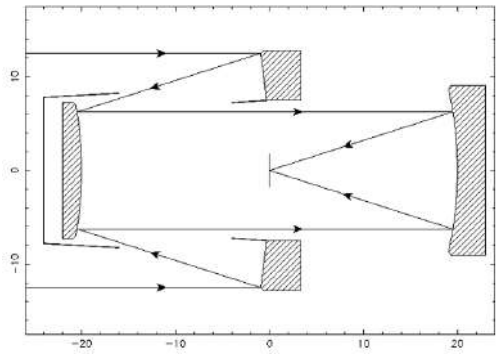

Fig. 5.2: TMA configuration [37]

1.2 Refractive systems

There are different articles proposing optical designs with similar characteristics than the desired optical system. In general, it is easy to find configurations with EFL = 100 mm, but the FoV is usually smaller and the f/# larger. Sometimes, some of the designs are also thought to work for a wider bandwidth (for example from 1 μm to 5 μm or from 3 μm to 12 μm). Therefore, none of the designs that are summarized here below matches directly the desired specifications. However, they serve as a starting point.

In [15], different material combinations of both doublet and triplet configurations are proposed for a bandwidth from 3 μm to 12 μm (such as Zns/KBr). However, there are not any detailed values for the design (such as lens curvature, lens thickness or distance between lenses). Something similar happens in [38], where the comparison of the performance of a SiGe doublet and a Si hybrid lens is discussed (see figure 5.3).

Despite there are no precise values in [38], during the course [10] the characteristics of a configuration of an optical system with EFL=100 mm are given for both SiGe doublet and Si hybrid lens (see figure 5.4)

Despite the silicon germanium doublet is the most commonly used, it would be also interesting to study if other material combination are also useful. In [17], the author develops some steps to calculate the lens curvature for a doublet achromat given the refractive index of the material and the focal length. Despite it is based on thin lens theory (therefore, the lens has no thickness), once obtained the curvatures the thickness may be intuitively guessed to have a starting point.

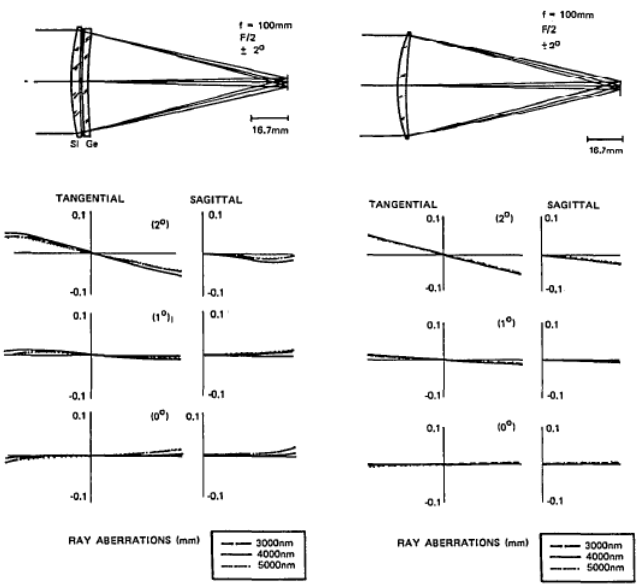

(a) Design and performance of a SiGe doublet

(b) Design and performance of a Si hybrid lens

Fig. 5.3: Comparison of the performance of a SiGe doublet and a Si hybrid lens [38]

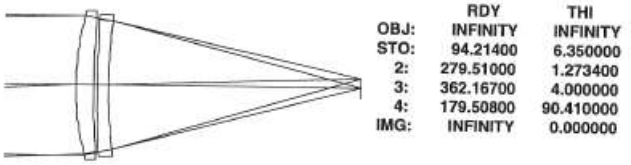

	RDY	THI
OBJ:	INFINITY	INFINITY
STO:	94.21400	6.350000
2:	279.51000	1.273400
3:	362.16700	4.000000
4:	179.50800	90.410000
IMG:	INFINITY	0.000000

(a) Design data of a SiGe doublet

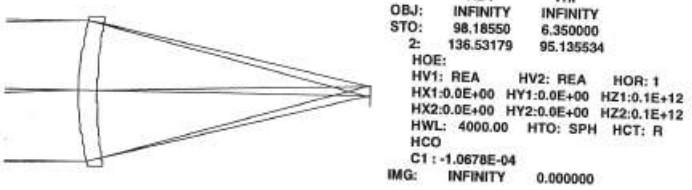

	RDY	THI
OBJ:	INFINITY	INFINITY
STO:	98.18550	6.350000
2:	136.53179	95.135534
HOE:		
HV1: REA	HV2: REA	HOR: 1
HX1:0.0E+00	HY1:0.0E+00	HZ1:0.1E+12
HX2:0.0E+00	HY2:0.0E+00	HZ2:0.1E+12
HWL: 4000.00	HTO: SPH	HCT: R
HCO		
C1 : -1.0678E-04		
IMG:	INFINITY	0.000000

(b) Design data of a Si hybrid lens

Fig. 5.4: Design data of a SiGe doublet and a Si hybrid lens

Regarding triplet configurations, [2] presents a triplet design using Amtir-1, germanium and zinc Selenide with its performance, again with no design data specified. There is also another design using Silicon, germanium and silicon in [7] where the layout, the performance and the data design are specified (see figure 5.5). This design should be adapted to the OUFTI-NEXT requirements given that the overall length of this design is 134 mm.

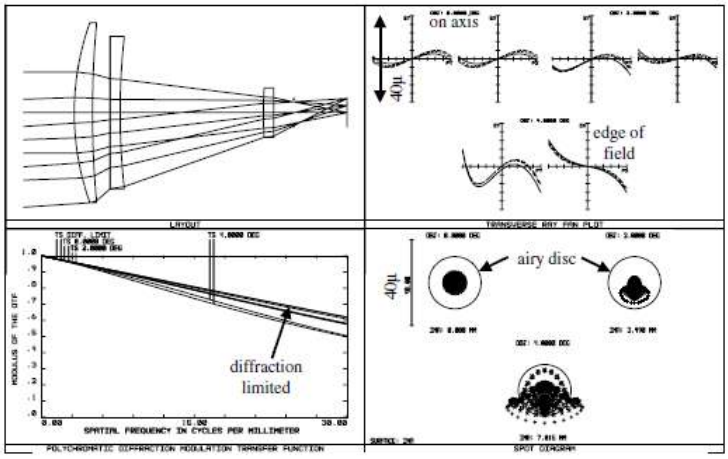

Surface		Radius	Thickness	Material
1		132.661 cx	9	silicon
2		480.403 cc	8.671	
3		Infinity	5	germanium
4		340.888 cc	70.846	
5		242.243 cx	5	silicon
6		Infinity	10	
7	stop	Infinity	26.3	
8		Image, infinity		

Fig. 5.5: Silicon germanium silicon triplet with its performance and data surface [7]

2 The doublet achromat

As already explained in section 1.4.1, the doublet achromat is the combination of two lenses with the aim of removing of chromatic spherical aberrations. The material combinations are multiple regarding the list of materials presented in chapter 4.

The method developed by Laikin in *Lens Design* [17] for thin lenses has been implemented in *Matlab* in order to obtain the radius of curvature for all 4 surfaces for a basic design before optimizing it with the optical software. In appendix A the method is detailed. Some of the results obtained are physically impossible, since the radius of curvature is smaller than the lens radius. However, the ones that do have sense have been implemented and optimized in *Code V*. As expected from the literature research, the silicon germanium doublet achromat is the one that gives better results in terms of reducing chromatic aberrations. Thus, all the efforts have been focused on optimizing this doublet.

The design data of the best configuration of silicon and germanium doublet achromat is shown in table 5.1 and its layout in figure 5.6. It is seen that the first surface performs as the aperture stop.

Table 5.1: Surface Data of SiGe doublet achromat with all surfaces sphere (UNIT: mm)

Surface	Surface Type	Y Radius	Thickness	Glass	Y Semi-Aperture
Object	Sphere	Infinity	Infinity		
Stop	Sphere	97.1236	8.8791	Silicon	30
2	Sphere	292.4626	0.5208		29.0470
3	Sphere	410.4532	5.5000	Germanium	28.9930
4	Sphere	192.4458	89.3447		27.8556
Image	Sphere	Infinity	0.0000		6.2005

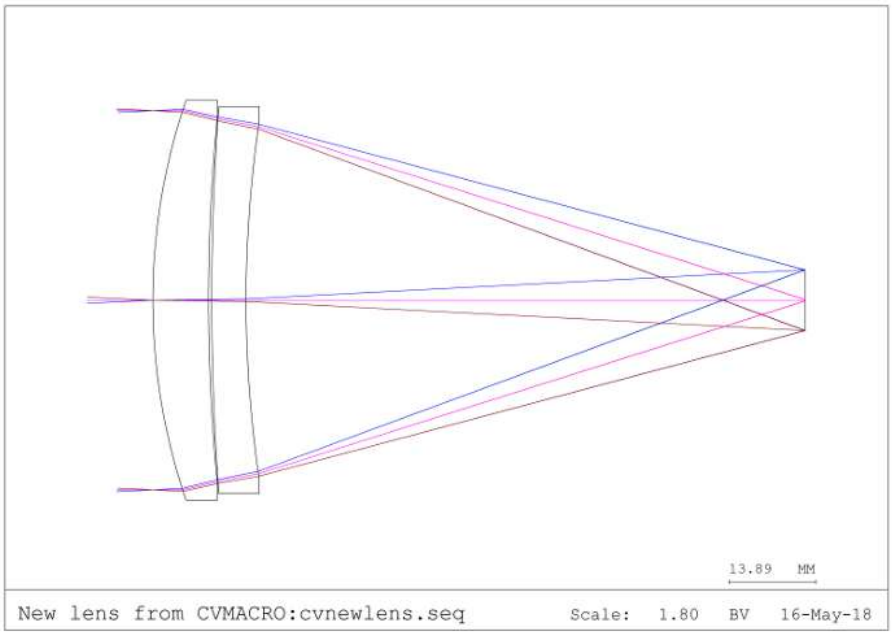

Fig. 5.6: Layout of SiGe doublet achromat with all surfaces sphere

The aberration curves (figure 5.7) and the spot diagram (figure 5.8) of this configuration are shown below. From the shape of the ray aberration curves, it can be concluded that spherical aberration dominates. It is also seen in figure 5.11 that the spot size is not small enough, being the highest RMS radius of 0.134357 mm.

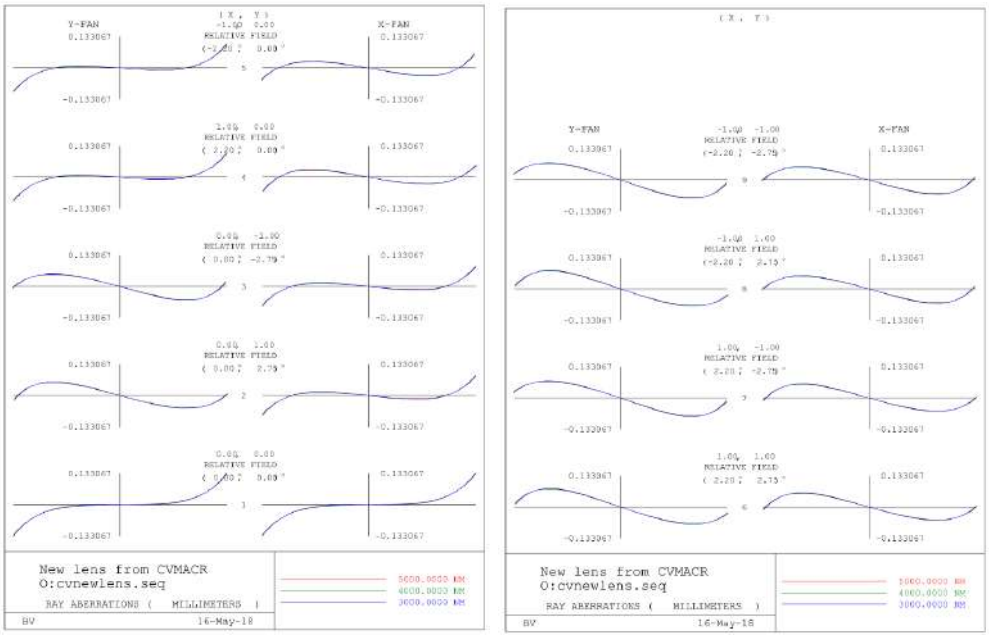

(a) Ray Aberration Curves (1) (b) Ray Aberration Curves (2)

Fig. 5.7: Ray Aberration Curves of the SiGe doublet achromat with all surfaces sphere

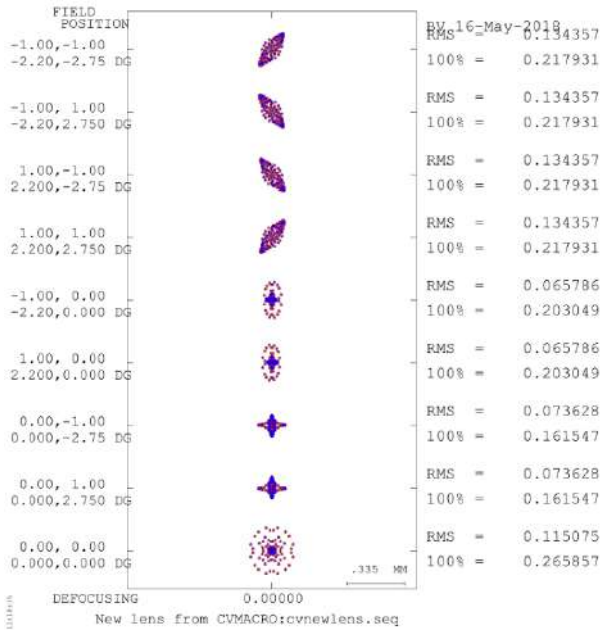

Fig. 5.8: Spot Diagram of SiGe doublet achromat with all sphere surfaces

Given that the main aberration is the spherical one, aspheric surfaces are used in order to minimize it. The surface data of the best design obtained after the optimization process is shown in table 5.2 and the layout in figure 5.9. Again, the aperture stop is at the first surface. It is seen that the first surface is an asphere surface.

Table 5.2: Surface Data of SiGe doublet achromat with first surface asphere (UNIT: mm)

Surface	Surface Type	Y Radius	Thickness	Glass	Y Semi-Aperture
Object	Sphere	Infinity	Infinity		
Stop	Asphere	99.62410	8.8570	Silicon	30
	K=-0.0337 A=-1.3278e-08	B=4.1200e-11	C=-1.6982e-14		
2	Sphere	315.1671	0.5727		29.0470
3	Sphere	546.6650	5.5000	Germanium	28.9930
4	Sphere	221.1643	89.6811		27.8556
Image	Sphere	Infinity	0.0000		6.2005

It can be concluded from the ray aberration curves (see figure 5.10) that there is no longer third order spherical aberration. However, the spot size is not reduced enough (see figure 5.11).

Similar results are obtained when changing all the rest of sphere surface to asphere. Therefore, it would be useless to use more aspheric surfaces as they would add cost to the design without improving the solution. The system suffers from field curvature. This can be seen in the layout. The rays of the extreme FoV focus earlier in the image plane than the on-axis rays. *Code V* places the focal plane in a compromised place between the best focus on-axis and the best focus off-axis.

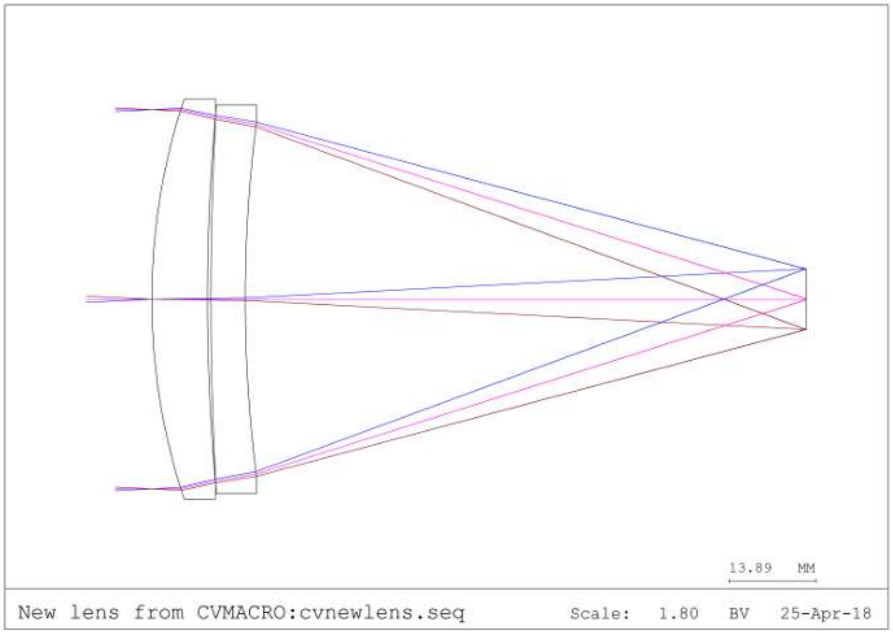

Fig. 5.9: Layout of SiGe doublet achromat with the first surface asphere

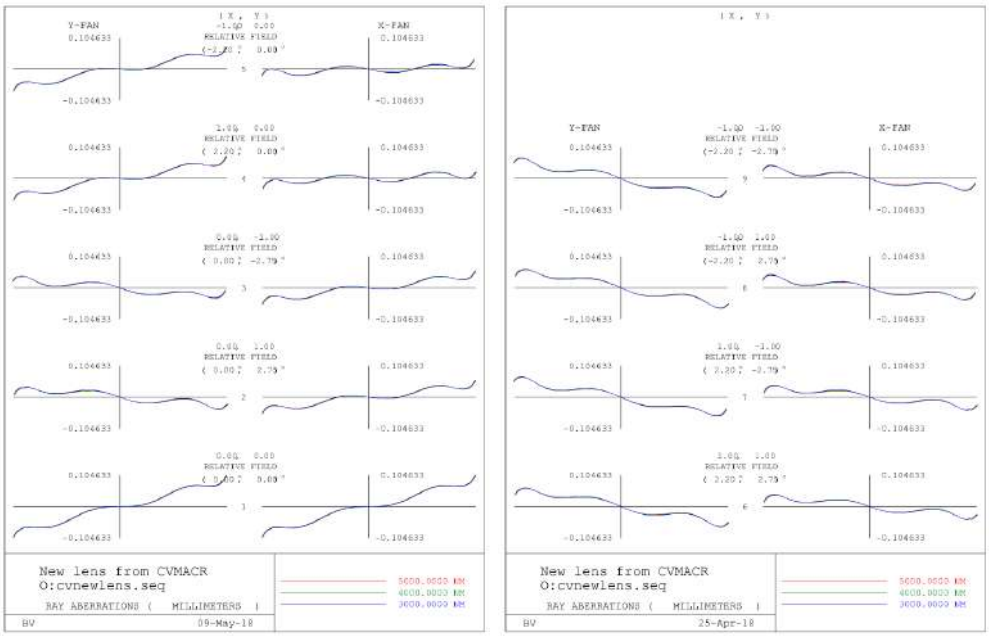

(a) Ray Aberration Curves (1) (b) Ray Aberration Curves (2)

Fig. 5.10: Ray Aberration Curves of the SiGe dobulet achromat with the first surfce asphere

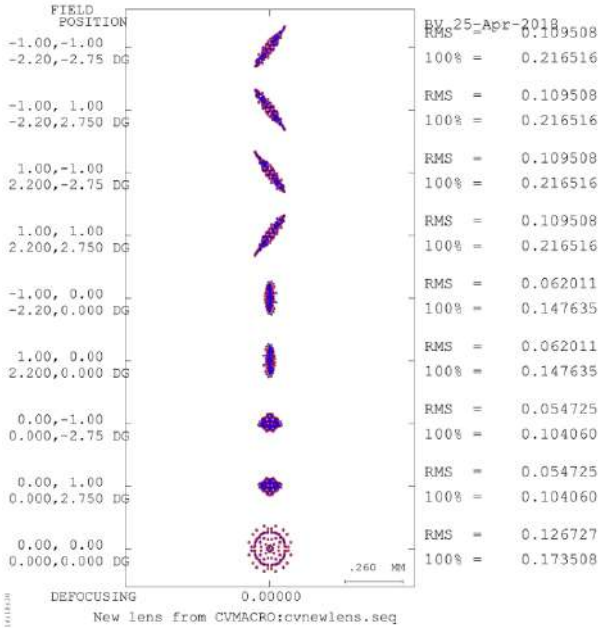

Fig. 5.11: Spot Diagram of SiGe doublet achromat with the first surfce asphere

3 Triplet

Since the system suffers from field curvature, an extra lens near the image plane needs to be added so that the on axis rays advance meanwhile the off-axis retard. The material of this lens can be any of those listed in chapter 4. In order to have a basic design to start from, the thickness of this third lens can be computed as follows:

$$OPD = (n-1)d \tag{5.1}$$

where the Optical Path Difference (OPD) is the distance difference between the best focus on-axis and the best focus off-axis, n is the refractive index of the material and d is the difference of thickness between on-axis and off-axis parts of the lens. Starting from this point with different materials, the obtained results are multiple and the best ones are presented in the following lines.

From all the possible materials, gallium arsenide (GaAs) is the one that gives better results when used for the third lens. Two different designs are presented. The data of the first design is shown in table 5.3. Again, the first surface is asphere while all the other ones are sphere. It can be seen in the layout (figure 5.12) that silicon and germanium lens are more separated than in the silicon germanium doublet achromat. This leads to an increase of chromatic aberration, which is verified when comparing both spots diagrams: meanwhile in figure 5.11 blue spots (corresponding to 3 μm wavelength) and red spots (corresponding to 3 μm wavelength) are practically indistinguishable, in figure 5.13 they can easily be differentiated. Despite this increase of chromatic aberration, the field curvature is highly reduced leading to a 100% spot size smaller than 15 μm for all the values of the FoV. Ray aberrations curves are added in appendix B1.1 for further information.

Table 5.3: Design data of SiGeGaAs (1) triplet (UNIT: mm)

Surface	Surface Type	Y Radius	Thickness	Glass	Y Semi-Aperture
Object	Sphere	Infinity	Infinity		
Stop	Asphere	98.3189	12.0000	Silicon	30.0000
	K=0.0639 A=5.1527e-09	B=1.9873e-12	C=7.8301-16		
2	Sphere	261.4657	8.6941		28.3558
3	Sphere	750.8694	8.0000	Germanium	24.5677
4	Sphere	194.5496	80.0000		23.3289
5	Sphere	18.8754	3.0882	Gallium Arsenide	9.0046
6	Sphere	18.4621	8.4097		7.9293
Image	Sphere	Infinity	0.0000		6.1601

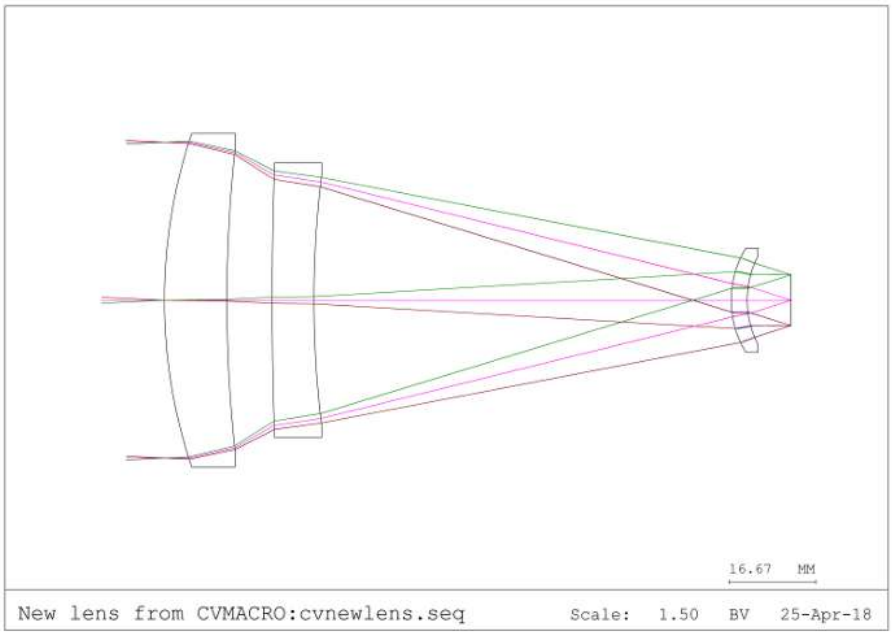

Fig. 5.12: Layout of SiGeGaAs (1) triplet

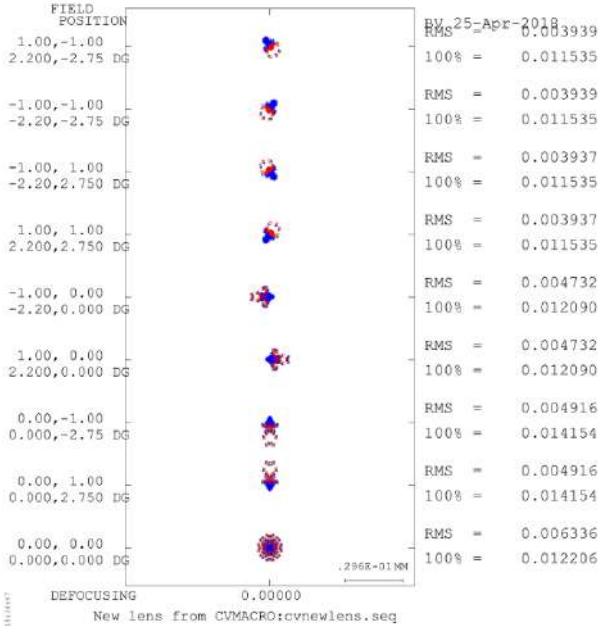

Fig. 5.13: Spot Diagram of SiGeGaAs (1)

The main different between the first and second design using GaAs as a third lens is the distance of this one to the detector. Meanwhile in the first design this value is 8.4097 mm (see table 5.3), in the second design the value is 20 mm (see table 5.4 and table 5.3). It is important to consider a design like this because the detector will be cooled down and some restriction due to thermal issued may appear. Therefore, the goal of this design is to demonstrate that there exist an optical design where the lens is far enough from the detector with acceptable results. It can be seen from figure 5.15 that the chromatic aberrations are larger in this design, as well as the spot size. Despite on the corners of the detector the 100% of the rays fall within a diameter

of 0.016286 mm, the RMS radius is 0.005491mm and, consequently, acceptable. If desired, ray aberrations curves of this configuration can be seen in appendix B1.2.

Table 5.4: Design data of SiGeGaAs (2) triplet (UNIT: mm)

Surface	Surface Type	Y Radius	Thickness	Glass	Y Semi-Aperture
Object	Sphere	Infinity	Infinity		
Stop	Asphere	59.5930	12.0000	Silicon	30.0000
	K=-0.1322 A=-5.5846e-08	B=-9.8737e-12	C=-4.1446e-15		
2	Sphere	97.1144	5.0000		27.4562
3	Sphere	50.9943	6.5000	Germanium	23.3836
4	Sphere	34.6458	61.7253		19.6539
5	Sphere	58.6119	4.3110	Gallium Arsenide	11.8329
6	Sphere	80.2396	20.0000		11.1313
Image	Sphere	Infinity	0.0000		6.1564

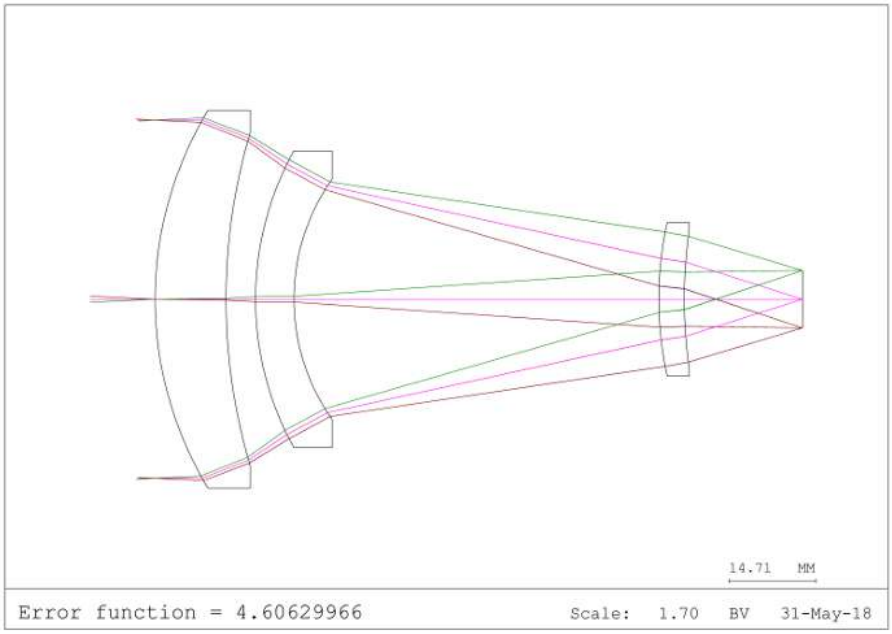

Fig. 5.14: Layout of SiGeGaAs (2) triplet

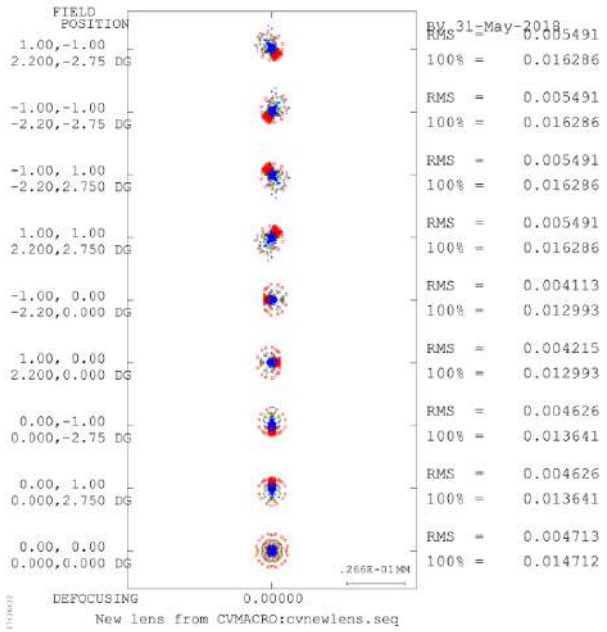

Fig. 5.15: Spot diagram of SiGeGaAs (2)

Another design using Zinc Sulphide (ZnS) for the third lens has also a good performance. The data of the system is shown in table 5.5 and the layout in figure 5.16. The third lens is much closer to the detector than the two previous designs. This is because the refractive index of GaAs is higher than that of ZnS (see figure 4.1). Therefore, the lens needs to be closer to the detector to have a similar effect on it. The results obtained are acceptable, given that maximum spot size is about 12μm (see figure 5.17). For further information on the design's performance, please see the ray aberration curves on appendix B1.3.

Table 5.5: Design data of SiGeZnS triplet (UNIT: mm)

Surface	Surface Type	Y Radius	Thickness	Glass	Y Semi-Aperture
Object	Sphere	Infinity	Infinity		
Stop	Asphere	67.6894	9.7774	Silicon	30.0000
	K=-0.2216 A=-3.9097e-08	B=-5.2160e-12	C=-1.0145e-15		
2	Sphere	132.7726	8.3324		28.4776
3	Sphere	63.3700	5.1212	Germanium	22.7701
4	Sphere	43.1879	75.2357		20.2001
5	Sphere	24.0577	7.6430	Zinc Sulphide	8.5893
6	Sphere	24.7866	3.3727		6.7400
Image	Sphere	Infinity	0.0000		6.1850

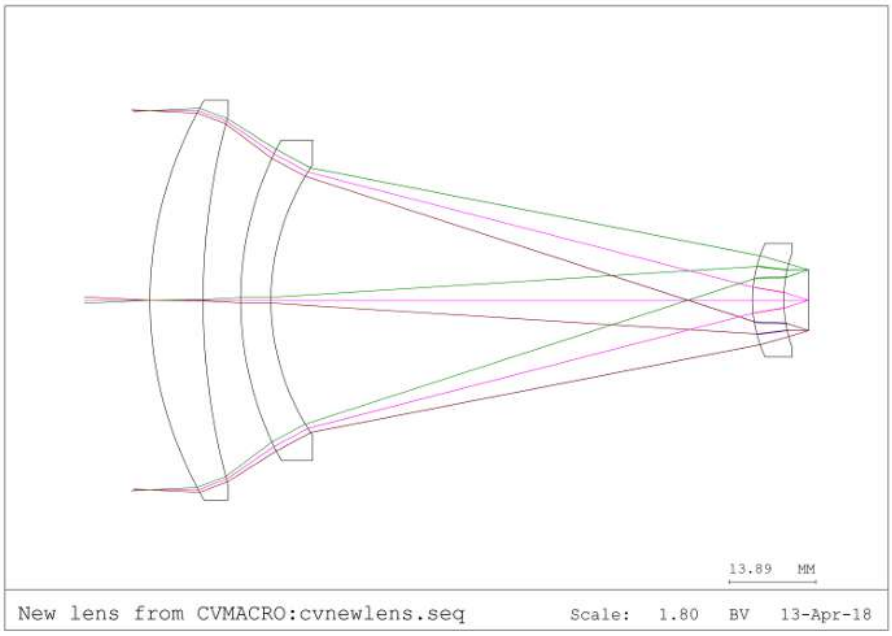

Fig. 5.16: Layout of SiGeZnS triplet

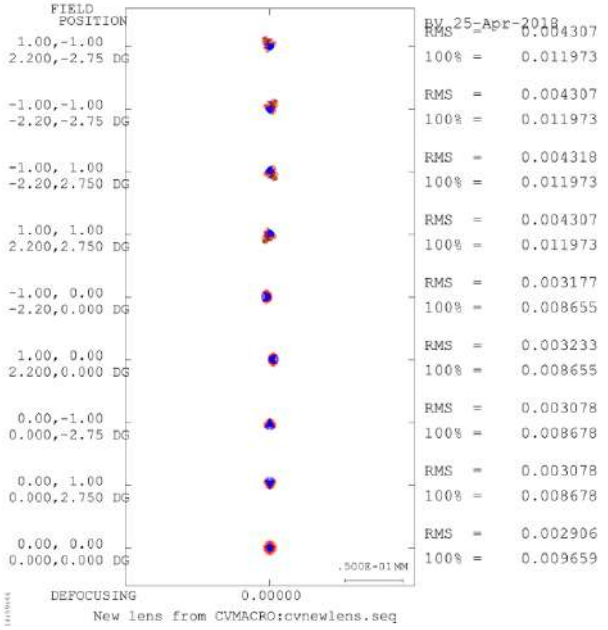

Fig. 5.17: Spot Diagram of SiGeZnS

As commented in section 2, the entrance pupil diameter of the system should be 65 mm in order to avoid diffraction limit. The three design presented above have been slightly re-optimized with D_p=65 mm and the data of these and the results obtained are exposed in appendix 1.4. When increasing the entrance pupil, the first design using GaAs exceeds the overall length by 0.425 mm and the total spot size is larger than 15 μm in almost all FoVs. However, the results are still acceptable given that the RMS radius is not larger than 7.5 μm. Regarding the two other designs, the spot size fairly increases and the 100% spot size does not exceed 15 μmu diameter in all FoVs.

4 Refractive-diffractive lenses: hybrid configuration

The goal of using hybrid lenses is to reduce the number of elements of the system. Therefore, it is going to be studied if it is possible to substitute the silicon germanium doublet by a hybrid lenses. If this works, it will be possible to have a simpler design with only two lenses (a hybrid lens and a meniscus lens relatively near the detector).

Before dealing with the final configuration, it is important to design a hybrid lens with a similar performance than that obtained with the doublet achromat. Table 5.6 shows the lens data of the design and figure 5.18 shows its layout. It is seen that the first surface of the lens is asphere and the second surface is a Holographic Optical Element (HOE). There are multiple parameters that define the HOE surface. All the parameters ended in 1 define the object while the ones ended in 2 define the reference of the construction. HV=REA, for both object and reference, means that the reference point source is real (REA). HX, HY and HZ define the x,y,z coordinates of the object/reference point source. HWL is the construction wavelength (in nm). HCT=R indicates that the coefficients for describing the phase function are rotationally symmetric. BLT refers to the type of blazed grating structure, which is specified as ideal here. Finally, C1, C2 and C3 are the polynomial coefficients of the phase function (see equation (2.4)).

Table 5.6: Data of silicon hybrid lens (UNIT: mm)

Surface	Surface Type	Y Radius	Thickness	Glass	Y Semi-Aperture
Object	Sphere	Infinity	Infinity		
Stop	Asphere	91.9309	8.0439	Silicon	30.0000
	K=2.8508				
	A=-5.1407e-07	B=-5.3564e-11	C=-1.0826-13		
2	Sphere (HOE)	138.1779	93.8045		28.8776
	HV1=REA	HV2=REA	HOR=1		
	HX1=0.0000	HY1=0.0000	HZ1=1e10		
	HX2=0.0000	HY2=0.0000	HZ2=1e10		
	HWL=4000	HCT=R	BLT=IDEAL		
	C1=-4.3911e-05	C2=-7.0925e-09	C3=4.9529e-12		
Image	Sphere	Infinity	0.0000		6.2353

Comparing the ray aberration curves for the silicon hybrid lens (figure 5.19) and for the silicon germanium doublet achromat (shown in figure 5.10), it can be seen that chromatic aberrations are larger in the hybrid solution, given that the the ray aberration curves for the three wavelengths do not coincide (4 μm is deviated from the rest), meanwhile in the doublet achromat solution the ray aberration curves are the same for the whole range of wavelengths. Nevertheless, the shape is quite similar: there is no aberration that dominates so the design is well optimized. As expected from the ray aberration curves, the spot size is also larger for the hybrid solution (see figure 5.20).

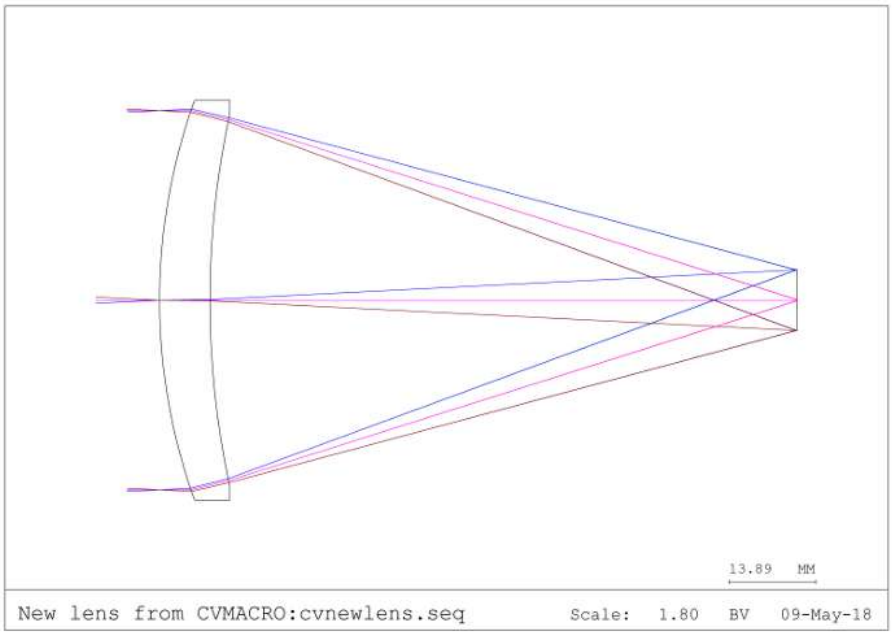

Fig. 5.18: Layout of hybrid silicon singlet

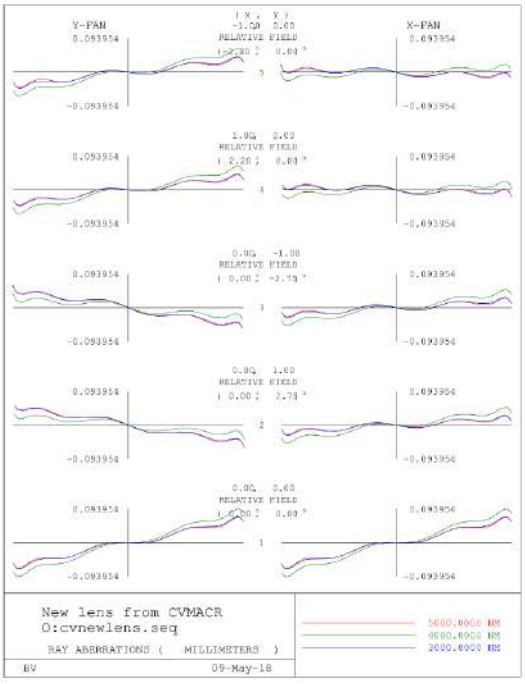

(a) Ray Aberration Curves (1)

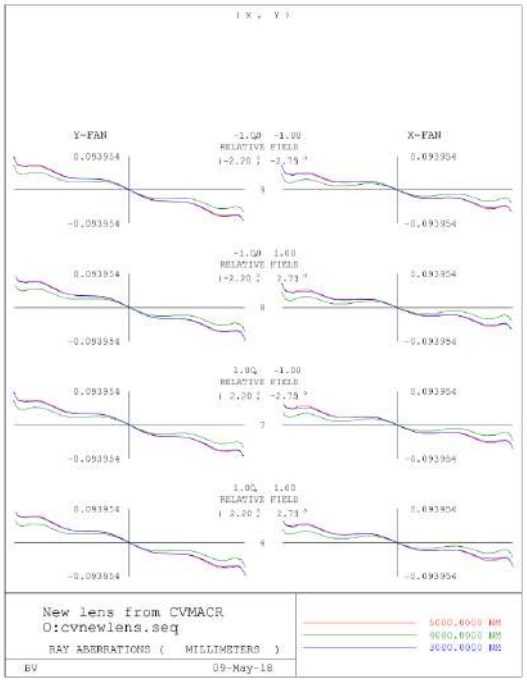

(b) Ray Aberration Curves (2)

Fig. 5.19: Ray Aberration Curves of the silicon hybrid singlet

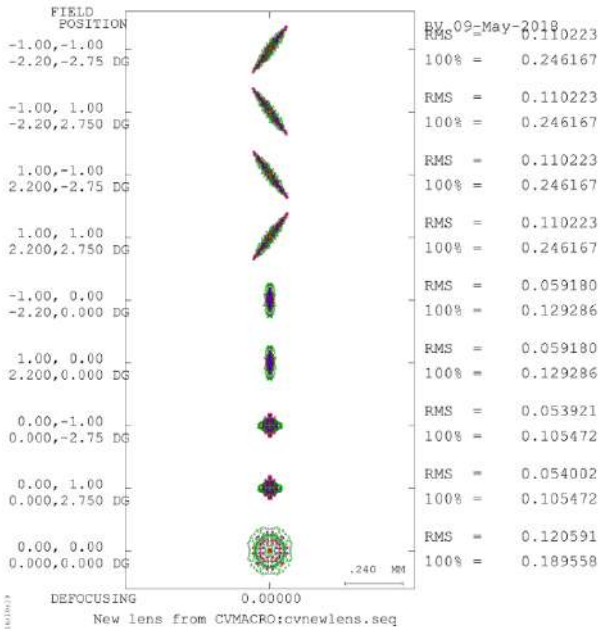

Fig. 5.20: Spot Diagram of hybrid silicon singlet

Similarly to what has been done for the triplet solutions, another lens is added near the detector. As seen previously, the chromatic aberrations are larger in the hybrid singlet than in the achromatic doublet. For this reason, it is not possible to get any acceptable solution for the whole range of the bandwidth (from 3 to 5 μm). Chromatic aberrations will decrease if the bandwidth is reduced. Looking at figure 2.21, it can be seen that from 3 to 3.4 μm the energy reaching the detector is very low and it can be neglected. With a bandwidth from 3.4 to 5 μm (in some cases from 3.5 to 5 μm) it is possible to obtain a good design.

Three different designs are presented using a silicon hybrid lens as the first element. The second lens material is changed in all designs: cadmium telluride (CdTe), GaAs and ZnS. The bandwidth of the first design goes from 3.5 to 5 μm meanwhile in the two other designs goes from 3.4 to 5μm. The designs data are presented in table 5.7, table 5.8 and table 5.9 with their layouts (figure 5.21, figure 5.22 and figure 5.23).

Table 5.7: Design data of Si(h)CdTe (UNIT: mm)

Surface	Surface Type	Y Radius	Thickness	Glass	Y Semi-Aperture
Object	Sphere	Infinity	Infinity		
Stop	Asphere	89.3277	10.0000	Silicon	30.0000
	K=0.932123				
	A=-1.7870e-07	B=-2.8846e-11	C=-9.3440e-15		
2	Sphere (HOE)	121.27594	88.7554		28.3414
	HV1=REA	HV2=REA	HOR=1		
	HX1=0.0000	HY1=0.0000	HZ1=1e10		
	HX2=0.0000	HY2=0.0000	HZ2=1e10		
	HWL=4000	HCT=R	BLT=IDEAL		
	C1=-3.4502e-05	C2=5.2099e-09	C3=-4.0683e-12		
3	Asphere	29.7888	4.8534	Cadmium Telluride	9.2470
	K=-2.7060				
	A=7.2089e-06	B=-1.8026e-08	C=0.0000		
4	Asphere	27.5114	10.9394		8.0414
	K=-0.5832				
	A=-2.0415-06	B=0.0000	C=0.0000		
Image	Sphere	Infinity	0.0000		6.2353

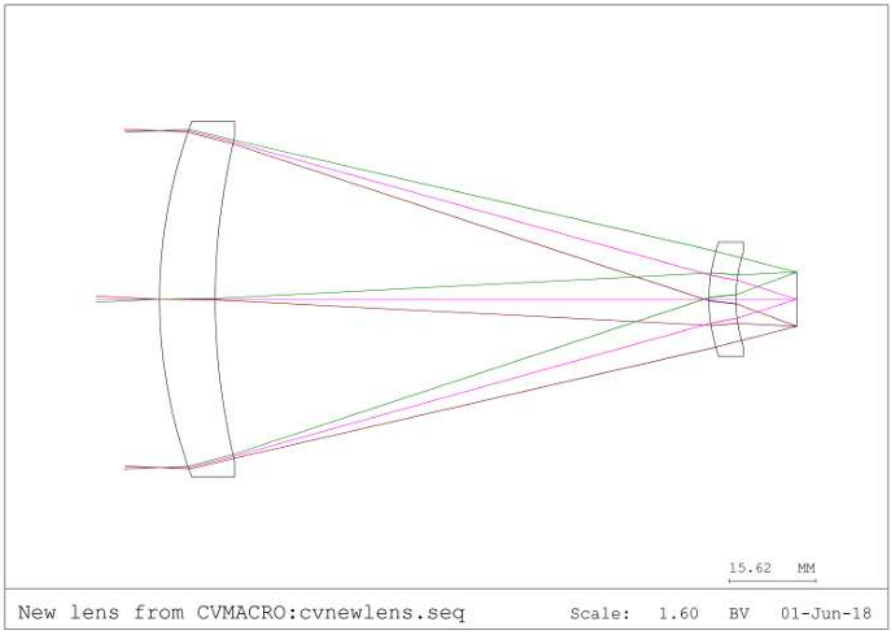

Fig. 5.21: Layout of Si(h)CdTe

Table 5.8: Design data of Si(h)GaAs (UNIT: mm)

Surface	Surface Type	Y Radius	Thickness	Glass	Y Semi-Aperture
Object	Sphere	Infinity	Infinity		
Stop	Asphere	97.6121	12.0000	Silicon	30.0000
	K=2.0111				
	A=-2.8511e-07	B=-4.9499e-11	C=-2.2486e-14		
2	Sphere (HOE)	135.4466	93.5824		28.0671
	HV1=REA	HV2=REA	HOR=1		
	HX1=0.0000	HY1=0.0000	HZ1=1e10		
	HX2=0.0000	HY2=0.0000	HZ2=1e10		
	HWL=4000	HCT=R	BLT=IDEAL		
	C1=-3.4699e-05	C2=4.5936e-09	C3=-3.6470e-12		
3	Asphere	31.2343	5.0000	Gallium Arsenide	8.8944
	K=-0.9378				
	A=1.4057e-06	B=-9.1162e-09	C=0.0000		
4	Asphere	29.2192	8.6212		7.6917
	K=-0.9104				
	A=3.8030-06	B=0.0000	C=0.0000		
Image	Sphere	Infinity	0.0000		6.2145

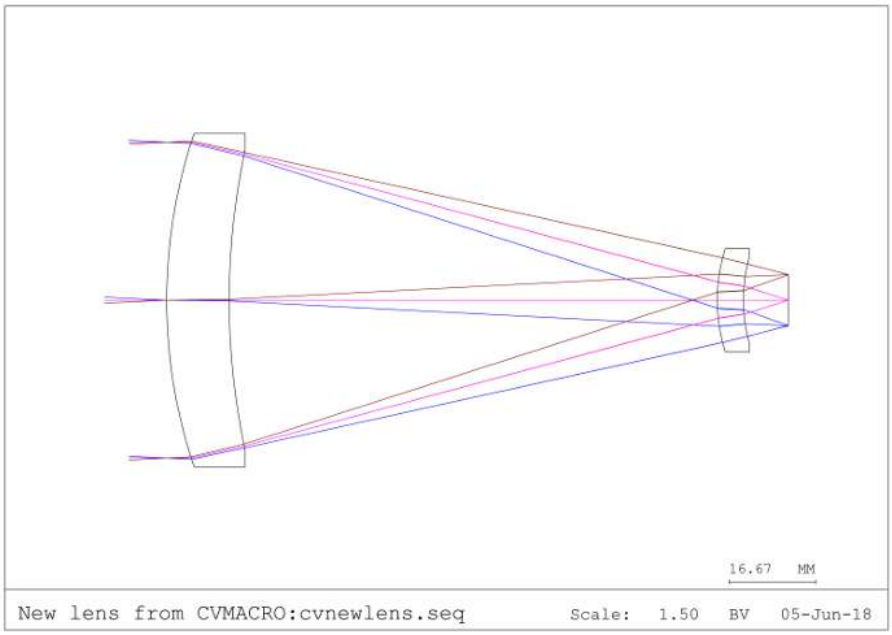

Fig. 5.22: Layout of Si(h)GaAs

Table 5.9: Design data of Si(h)ZnS (UNIT: mm)

Surface	Surface Type	Y Radius	Thickness	Glass	Y Semi-Aperture
Object	Sphere	Infinity	Infinity		
Stop	Asphere	98.5328	10.0000	Silicon	30.0000
	K=2.3338				
	A=-3.2249e-07	B=-5.6085e-11	C=-3.0145e-14		
2	Sphere (HOE)	143.4283	95.0000		28.0701
	HV1=REA	HV2=REA	HOR=1		
	HX1=0.0000	HY1=0.0000	HZ1=1e10		
	HX2=0.0000	HY2=0.0000	HZ2=1e10		
	HWL=4000	HCT=R	BLT=IDEAL		
	C1=-3.2464e-05	C2=4.3700e-10	C3=-4.5120e-13		
3	Asphere	29.4885	5.0000	Zinc Sulphide	7.9163
	K=-2.3171				
	A=-7.0295e-08	B=-7.0055e-e08	C=0.0000		
4	Asphere	27.7656	4.7988		6.8786
	K=-0.3899				
	A=-2.7942-06	B=0.0000	C=0.0000		
Image	Sphere	Infinity	0.0000		6.2544

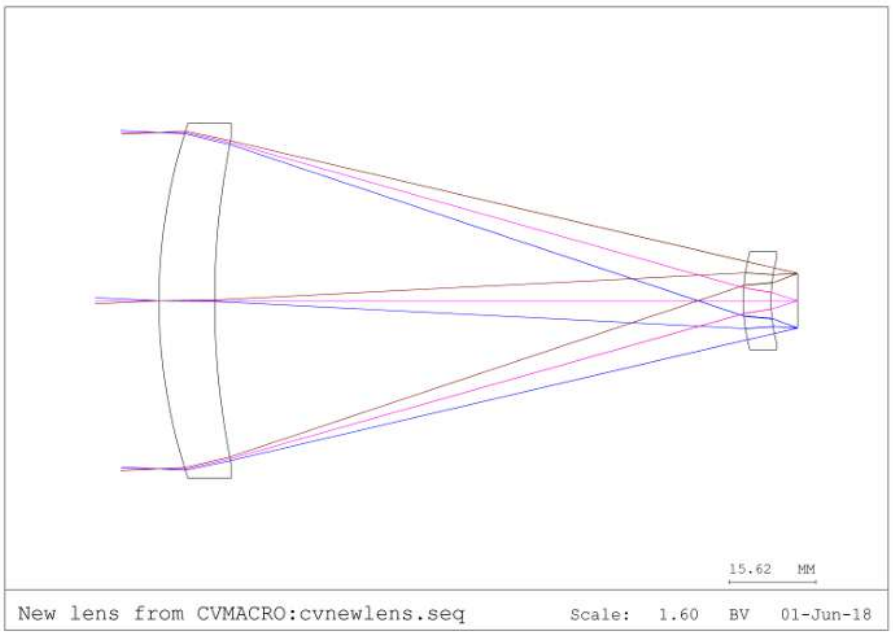

Fig. 5.23: Layout of Si(h)ZnS

From the ray aberration curves (figure 5.24, figure 5.26 and figure 5.28), it can be seen that in all cases there is some achromatic aberration given that the ray curves do not coincide for the different wavelengths. However, the magnitude of the aberrations is significantly reduced comparing to the singlet silicon hybrid lens (see figure 5.19). This is seen in the spot diagrams (figure 5.25, figure 5.27 and figure 5.29) where, although 100% spot size is larger in diameter than 15μm, the RMS radius is always smaller than 7.5μm in the three cases for all FoVs.

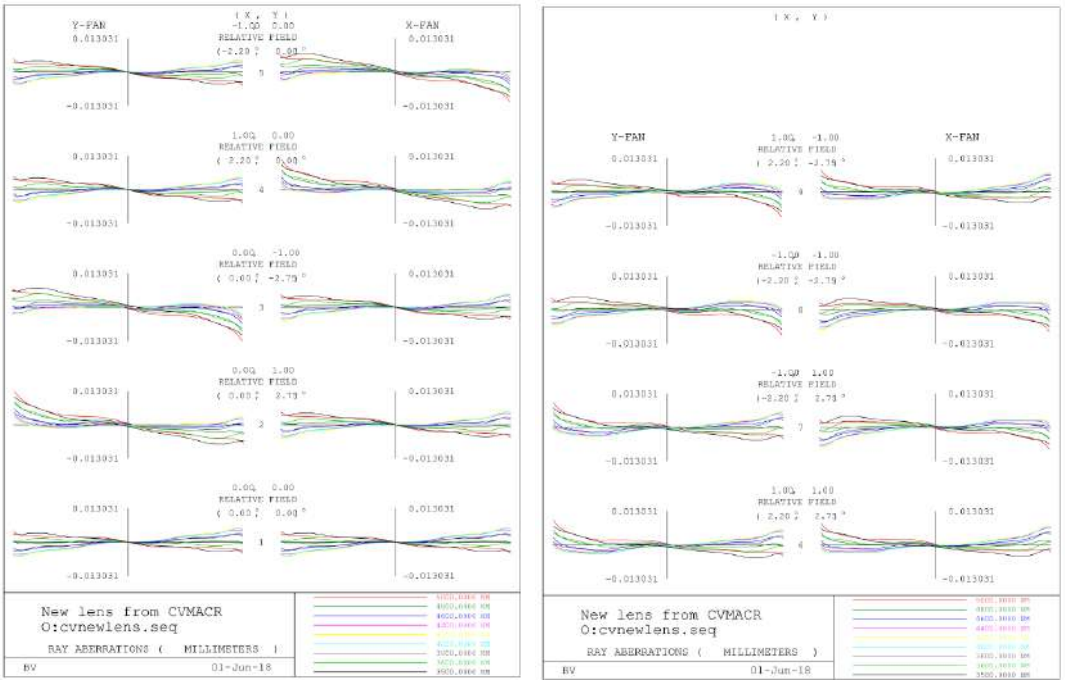

(a) Ray Aberration Curves (1)

(b) Ray Aberration Curves (2)

Fig. 5.24: Ray aberration curves of Si(h)CdTe

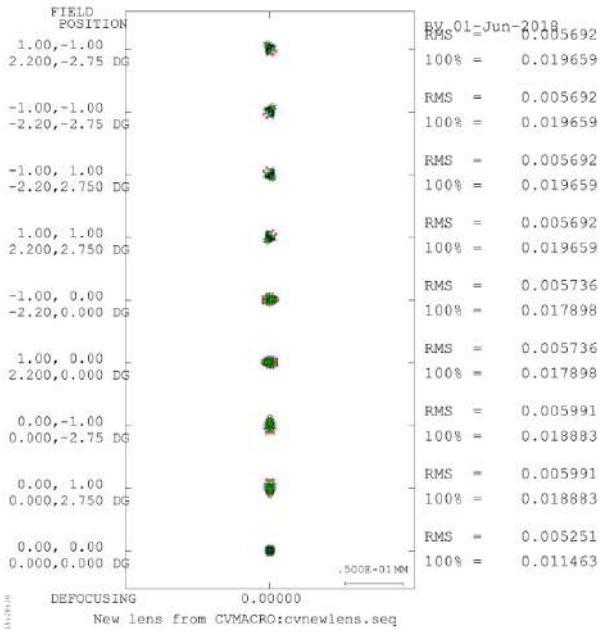

Fig. 5.25: Spot diagram of Si(h)CdTe

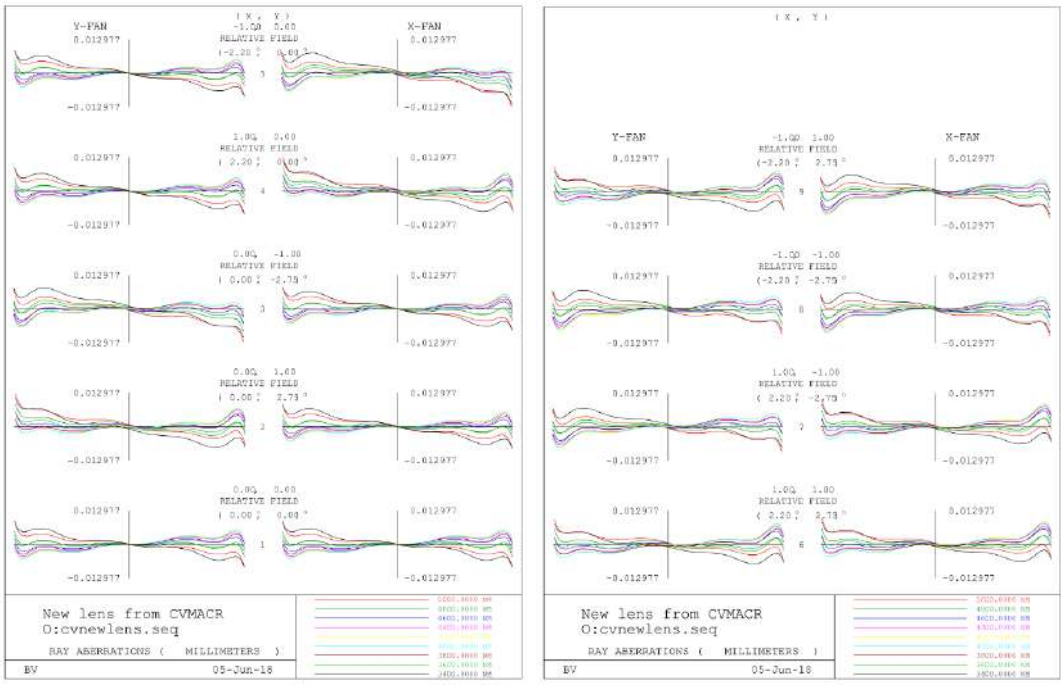

(a) Ray Aberration Curves (1) (b) Ray Aberration Curves (2)

Fig. 5.26: Ray aberration curves of Si(h)GaAs

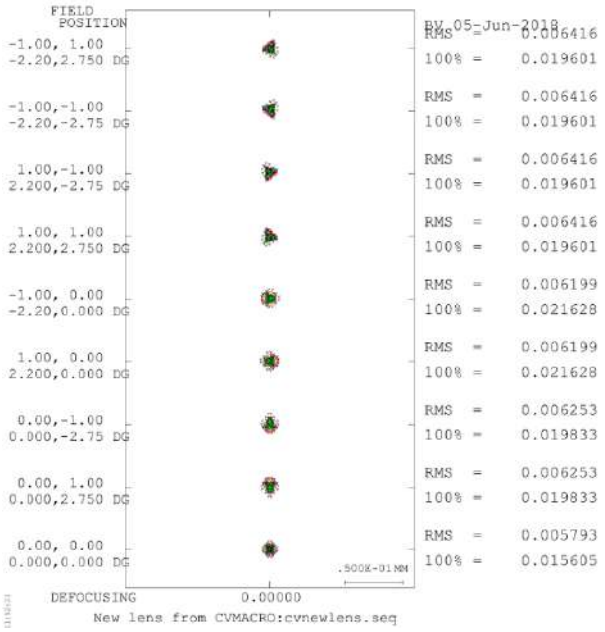

Fig. 5.27: Spot diagram of Si(h)GaAs)

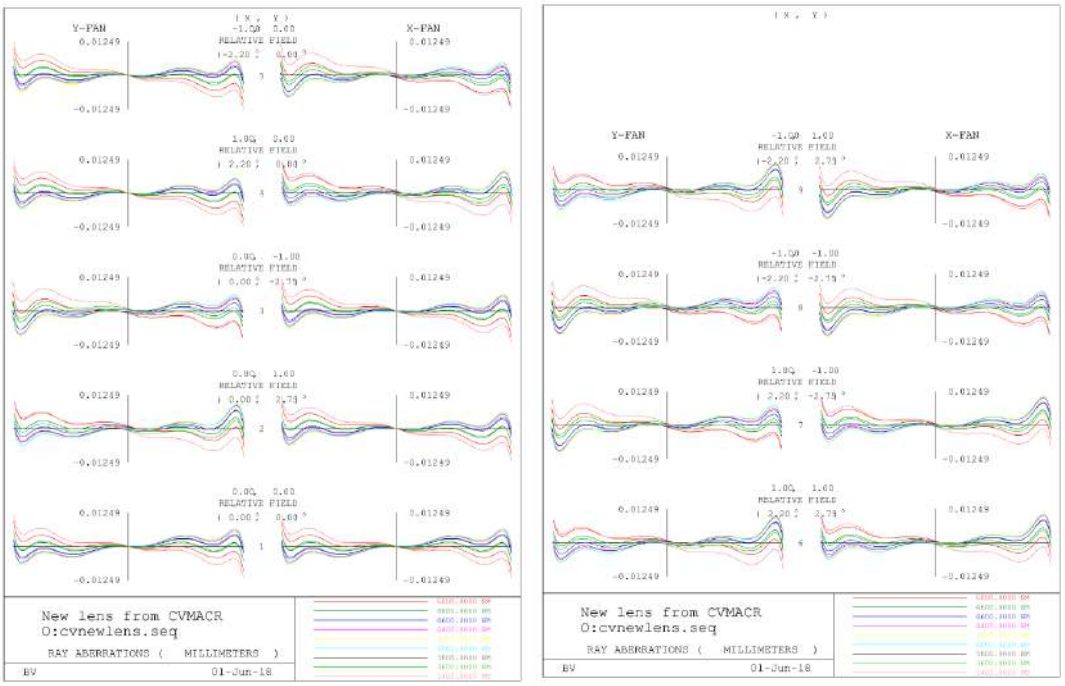

(a) Ray Aberration Curves (1)

(b) Ray Aberration Curves (2)

Fig. 5.28: Ray aberration curves of Si(h)ZnS

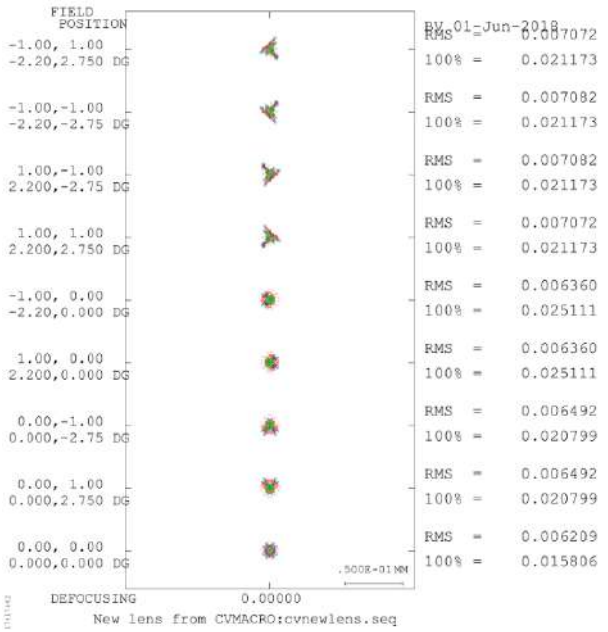

Fig. 5.29: Spot diagram of Si(h)ZnS

If it is of interest for the reader, the designs presented above have been modified increasing its entrance pupil diameter up to 65 mm. The results obtained are acceptable (RMS radius size is smaller than 7.5 μm) when using CdTe and GaAs for the second lens in all FoVs. The data and results of both designs are presented in appendix 2.1. However, with a ZnS second lens the design does no longer meet the desired requirements for this application.

Chapter 6

Temperature effects on the designs

The payload will be highly affected by the change of temperatures at which the CubeSat will be exposed. The temperature variation affects the optical system in a large number of ways. The effects are in general unpredictable unless some assumptions are made: the temperature variation is uniform and the temperature gradients are radial. Then, the changes that an optical system suffers due to a temperature change, dT, can be summarized and modeled as follows [14]:

- Change of radius, R, of the lenses due to the thermal expansion of the lenses material:

$$R + dR = R(1 + x_l)dT \tag{6.1}$$

- Change of thickness, D, of the lenses due to the thermal expansion of the lenses material:

$$D + dD = D(1 + x_l)dT \tag{6.2}$$

- Change of the distance between the lenses, L, due to the thermal expansion of the mount:

$$L + dL = L(1 + x_m)dT \tag{6.3}$$

- Change of the refractive index, n, of the lenses materials:

$$n + dn = n + \frac{dn}{dT}dT \tag{6.4}$$

x_l is the thermal expansion coefficient of the material of the lens, x_m is the thermal expansion coefficient of the mount and $\frac{dn}{dT}$ is the refractive index temperature gradient. For diffractive lenses, other equations must be added given that the surface relief also changes with temperature. In [9], the equation (6.5) that takes into account the variation of the phase function coefficients (remember equation (2.4)) is stated:

$$\frac{dC_i}{dT} = -2\ i\ x_l\ C_i \tag{6.5}$$

i indicates the phase function coefficient number (1, 2, 3...). Then, being T_f the final temperature and T_0 initial temperature, the variation of the phase function coefficients as a function of the temperature can be expressed as:

$$C_i + dC_i = C_i e^{-2\ i\ x_l(T_f - T_0)} \tag{6.6}$$

Concerning the temperature at which the CubeSat will be exposed, it is still not known in exactitude. However, figure 6.1 shows a first estimation of the expected temperature at which

the optical system will be during the mission. It shows the temperature variations of an orbit in both coldest and hottest cases and for 400 and 800 km altitude orbits. By now, it is known that 800 km altitude orbit is not feasible if GSD must be smaller than 100 m (see section 2). However, this was not known at the beginning and this is the reason why the considered orbit altitude range is wider. From figure 6.1, it can be seen that the maximum temperature at which the payload will be exposed is 0°C meanwhile the minimum temperature will be -45°C.

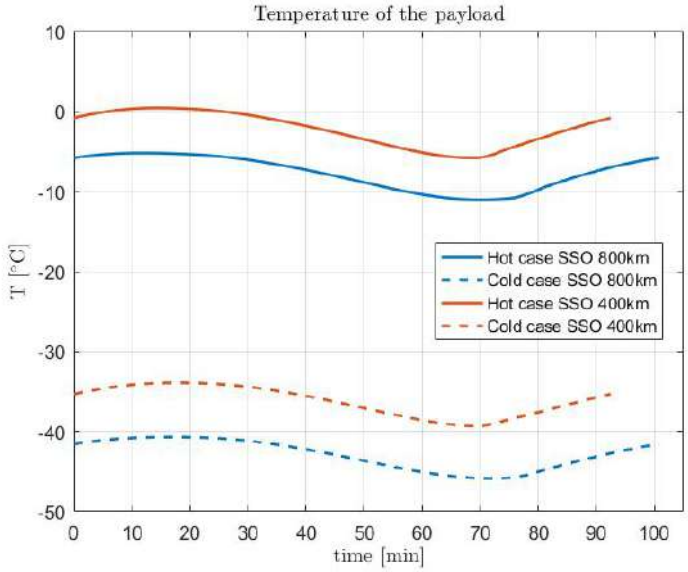

Fig. 6.1: estimation of temperature values for the hottest and coldest case for 400km and 800km altitude orbits

The thermal study carried out is not a deep study. A deep study at this stage of the project is not possible given that there are still many unknowns (the exact temperature range, the altitude of the orbit, the mount material, ...). However, it is good to know to what extent the temperature variation is a critical point for the optical system and which is the performance tendency it has when the temperature changes. Therefore, the goal of this analysis is not to obtain quantitative results but to obtain qualitative results in order to guide the designer in more advanced design stages.

Before applying the equations that model the changes with temperature (6.1, 6.2, 6.3 and 6.4), it is necessary to know the coefficients they use. x_l and $\frac{dn}{dT}$ are already defined in table 4.1 for each material. The material of the mount is still not known. Two materials, with very different thermal expansion coefficients, are considered in order to study how the choice of the mount material affects the system: aluminum and invar. In table 6.1 the thermal expansion coefficients are shown and it can be seen that aluminum's is ten times larger than invar's [35]:

Table 6.1: Thermal expansion coefficients of aluminum and invar [35]

Material	Thermal expansion coefficient, x_m (K^{-1})
Aluminium	$22.5 \cdot 10^{-6}$
Invar	$1.5 \cdot 10^{-6}$

1 Re-optimized optical designs

The performance of the system with the temperature changes has been calculated for all the optical systems shown in chapter 5 with acceptable results. This is three triplet configurations and three doublet hybrid configurations. However, only the two best results obtained for triplet and doublet hybrid configurations are discussed: the triplet SiGeGaAs (2) (see table 5.4), the triplet SiGeZnS (see table 5.5), the doublet hybrid Si(h)GaAs (see table 5.8) and the doublet hybrid Si(h)ZnS (see table 5.9). In this section, the procedure of the thermal study is explained for the first system, meanwhile for the other systems only few results are shown since the most relevant results for the analysis are presented in section 2, as well as its discussion. Despite this, if the reader wants more detailed information, it can be found in appendix C.

So far, the optical systems are designed for room temperature. However, room temperature is not even between the temperature range that must be considered. For this reason, the designs are re-optimized for -22.5°C. Then, equations 6.1, 6.2, 6.3, 6.4 and 6.5 (if needed) have been applied for minimum and maximum temperature values and for aluminum and invar materials in each design.

1.1 SiGeGaAs (2)

The first design re-optimized is the SiGeGaAs (2) triplet for -22.5°C. Its design data is shown in table 6.2 and the layout is shown in figure 6.2.

Table 6.2: Design data of SiGeGaAs (2) triplet re-optimized for -22.5°C (UNIT: mm)

Surface	Surface Type	Y Radius	Thickness	Glass	Y Semi-Aperture
Object	Sphere	Infinity	Infinity		
Stop	Asphere	59.4835	12.0000	Silicon	30.0000
	K=-0.14202 A=-5.0809e-08	B=-8.1078e-12	C=-3.8363e-15		
2	Sphere	96.8917	5.0000		27.4563
3	Sphere	50.9870	6.5000	Germanium	23.3925
4	Sphere	34.6079	61.6676		19.6586
5	Sphere	57.8370	4.5194	Gallium Arsenide	11.8588
6	Sphere	78.2738	20.0000		11.1114
Image	Sphere	Infinity	0.0000		6.1559

The spot diagram for its design temperature is shown in figure 6.3. Figure 6.4 and figure 6.5 show the spot diagrams for both maximum and minimum temperatures and for aluminum and invar materials.

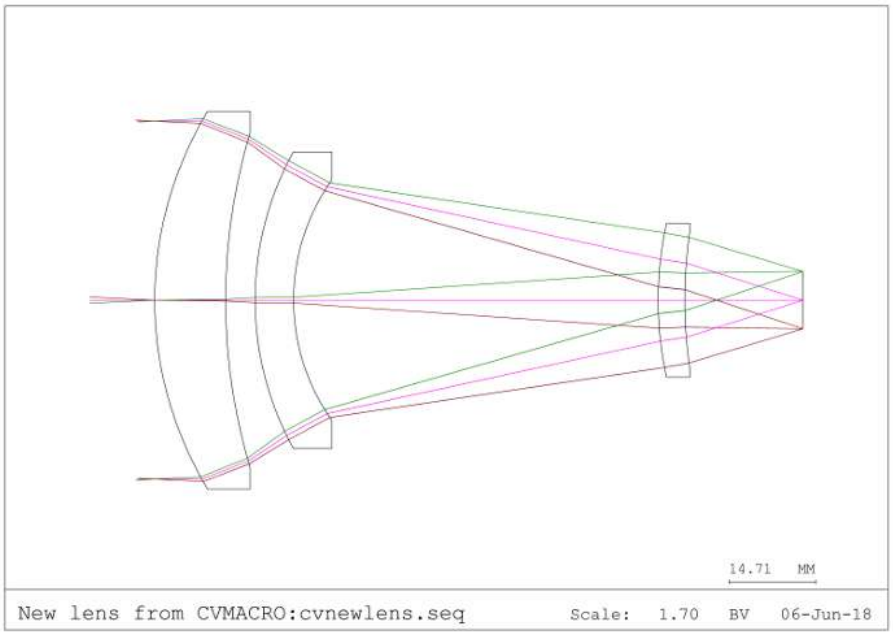

Fig. 6.2: Layout of the SiGeGaAs (2) optical design re-optimized for -22.5°C

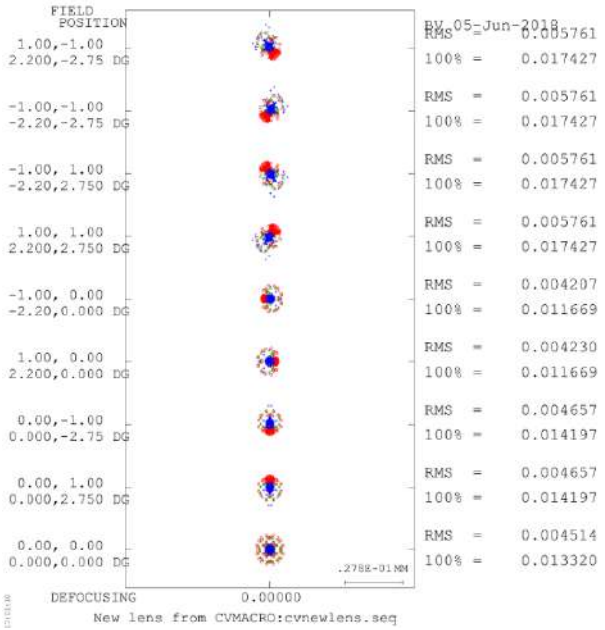

Fig. 6.3: Spot diagram of the SiGeGaAs (2) optical design re-optimized for -22.5°C

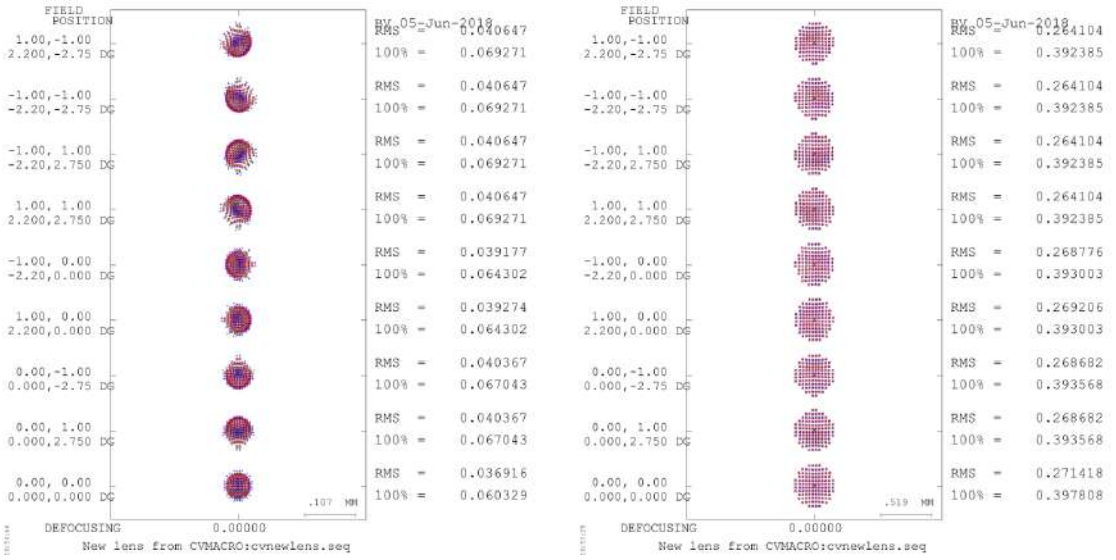

(a) T=0°C (b) T=-45°C

Fig. 6.4: Spot Diagrams of the SiGeGaAs (2) optical design re-optimized for -22.5°C at maximum and minimum temperatures for aluminum mount

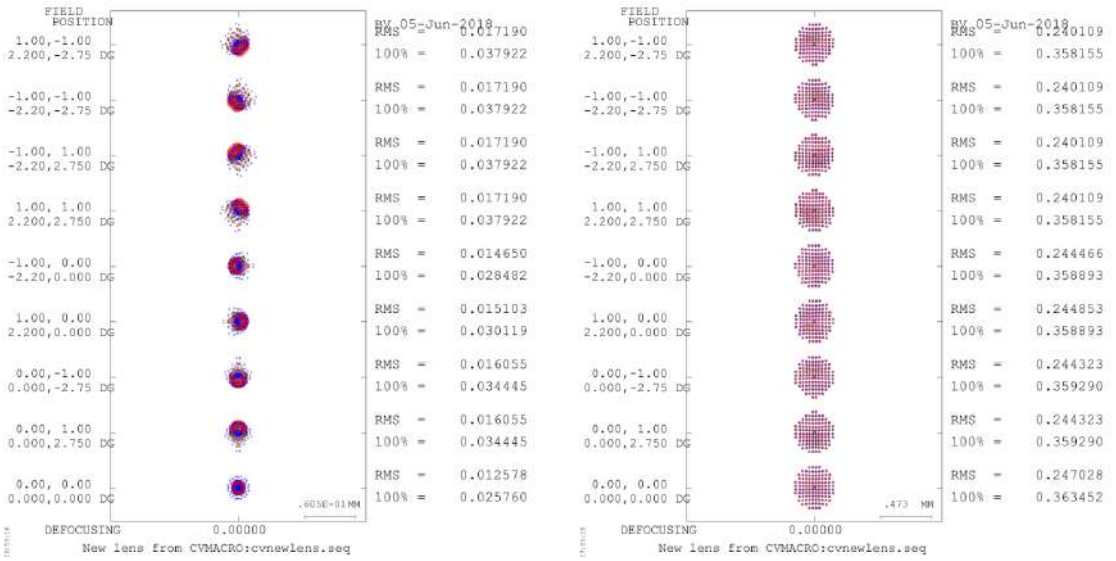

(a) T=0°C (b) T=-45°C

Fig. 6.5: Spot Diagrams of the SiGeGaAs (2) optical design re-optimized for -22.5°C at maximum and minimum temperatures for invar mount

The performance of the re-optimized system for its design temperature is good (figure 6.3) but when the temperature is increased or decreased the results are no longer good, being the ones obtained for the aluminum material little worse (see figure 6.4 and figure 6.5). Given the symmetric shape of the spots and its expansion in all cases, it seems that the main problem is defocus. In order to prove it, it is studied what happens if the image plane is positioned at the focus plane of the optical system affected by the temperature (figure 6.6 and figure 6.7):

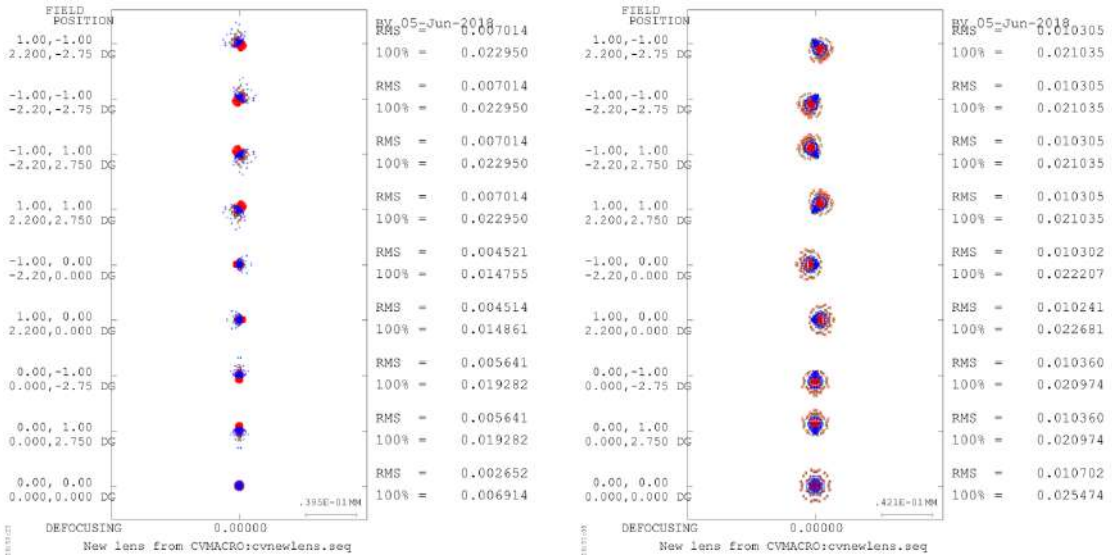

(a) T=0°C (b) T=-45°C

Fig. 6.6: Spot Diagrams of the SiGeGaAs (2) optical design re-optimized for -22.5°C at maximum and minimum temperatures for aluminum mount with the image plane focused

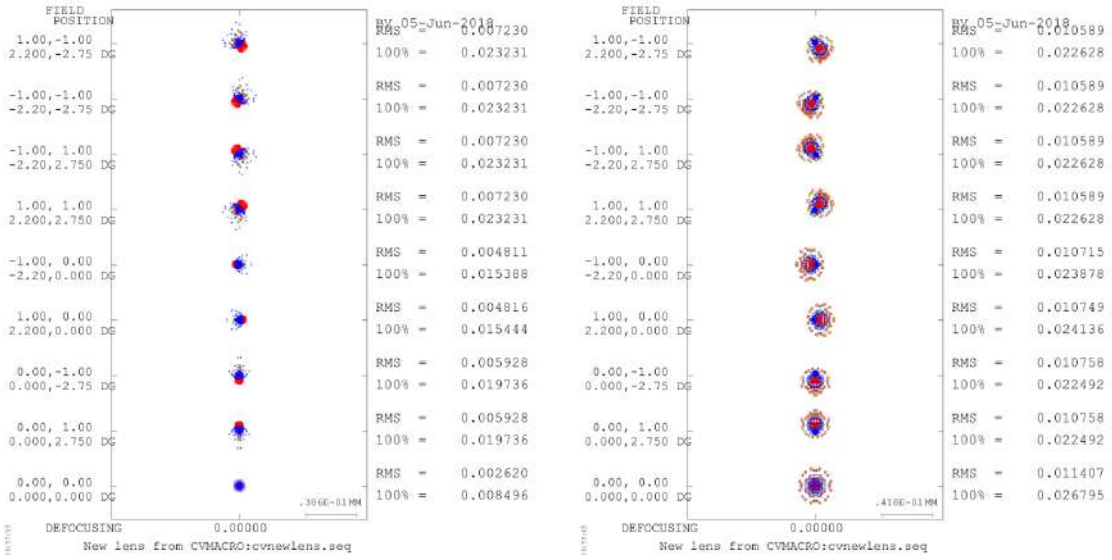

(a) T=0°C (b) T=-45°C

Fig. 6.7: Spot Diagrams of the SiGeGaAs (2) optical design re-optimized for -22.5°C at maximum and minimum temperatures for invar mount with the image plane focused

From figure 6.6 and figure 6.7 it is seen that the RMS radius value for a T=0°C is smaller than 7.5μm for both materials and for all FoVs. However, the results are not so good for T=-45°C even though the spot size has been considerably reduced and it is now closer to an acceptable result. From all this, it can be concluded that, if the image plane could be somehow moved to the ideal focus plane the performance of optical design could still be good. The exact distance values that the image plane needs to be moved to focus are shown in table 6.3, where negative values mean that the focal plane is closer to the lens than the image plane while positive values

mean that the focal plane is situated after the image plane.

Table 6.3: Distances from real image plane to ideal for SiGeGaAs(2) (UNIT:mm)

Material	Distance (T=0°C)	Distance (T=-45°C)
Aluminum	-0.0850	0.5957
Invar	-0.0274	0.5386

1.2 SiGeZnS

The same procedure used for the SiGeGaAs(2) triplet has been applied to the SiGeZnS triplet (see table 5.5). The design data once re-optimized the system for -22.5°C is shown in table 6.4 and the layout in figure 6.8.

Table 6.4: Design data of SiGeZnS triplet re-optimized for -22.5°C (UNIT: mm)

Surface	Surface Type	Y Radius	Thickness	Glass	Y Semi-Aperture
Object	Sphere	Infinity	Infinity		
Stop	Asphere	69.1126	10.0000	Silicon	30.0000
	K=-0.2178 A=-3.5589e-08	B=-5.3413e-12	C=-7.6461e-16		
2	Sphere	137.29127	7.7172		28.4326
3	Sphere	68.7426	5.0000	Germanium	23.2242
4	Sphere	46.9851	75.0000		20.8187
5	Sphere	19.7200	5.0000	Zinc Sulphide	8.3259
6	Sphere	20.0485	4.5407		6.9458
Image	Sphere	Infinity	0.0000		3.1786

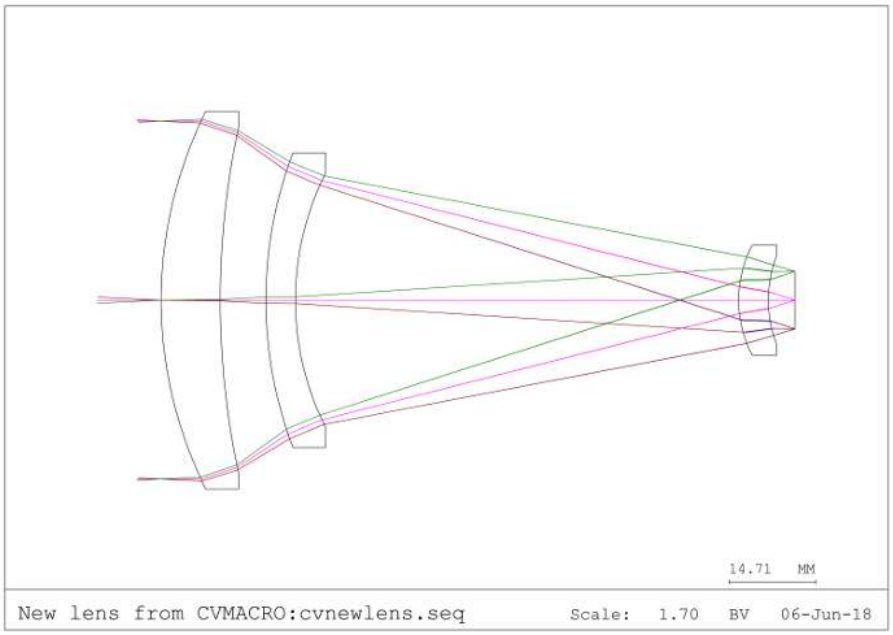

Fig. 6.8: Layout of the SiGeZnS optical design re-optimized for -22.5°C

The distances between the focal plane and the image plane are summarized in table 6.5.

Table 6.5: Distances from real image plane to ideal for SiGeZnS (UNIT:mm)

Material	Distance (T=0°C)	Distance (T=-45°C)
Aluminum	-0.0923	0.0928
Invar	-0.03181	0.0326

For further information of the performance of this design, see appendix C1.

1.3 Si(h)GaAs

The Si(h)GaAs optical system shown in table 5.8 is re-optimized for -22.5°C. The data of this new design is shown in table 6.6 and the layout in figure 6.9.

Table 6.6: Design data of Si(h)GaAs hybrid doublet re-optimized for -22.5°C(UNIT: mm)

Surface	Surface Type	Y Radius	Thickness	Glass	Y Semi-Aperture
Object	Sphere	Infinity	Infinity		
Stop	Asphere	98.0044	12.0000	Silicon	30.0000
	K=1.9958				
	A=-2.7963-07	B=-4.8207e-11	C=-2.1418e-14		
2	Sphere (HOE)	136.3482	93.9700		28.0782
	HV1=REA	HV2=REA	HOR=1		
	HX1=0.0000	HY1=0.0000	HZ1=1e10		
	HX2=0.0000	HY2=0.0000	HZ2=1e10		
	HWL=4000	HCT=R	BLT=IDEAL		
	C1=-3.5046e-05	C2=4.8179e-09	C3=-3.81930e-12		
3	Asphere	30.7904	5.0000	Gallium Arsenide	8.9052
	K=-0.9085				
	A=1.6369e-06	B=-9.0331e-09	C=0.0000		
4	Asphere	28.8022	8.5755		7.6883
	K=-0.9553				
	A=4.4868-06	B=0.0000	C=0.0000		
Image	Sphere	Infinity	0.0000		6.2138

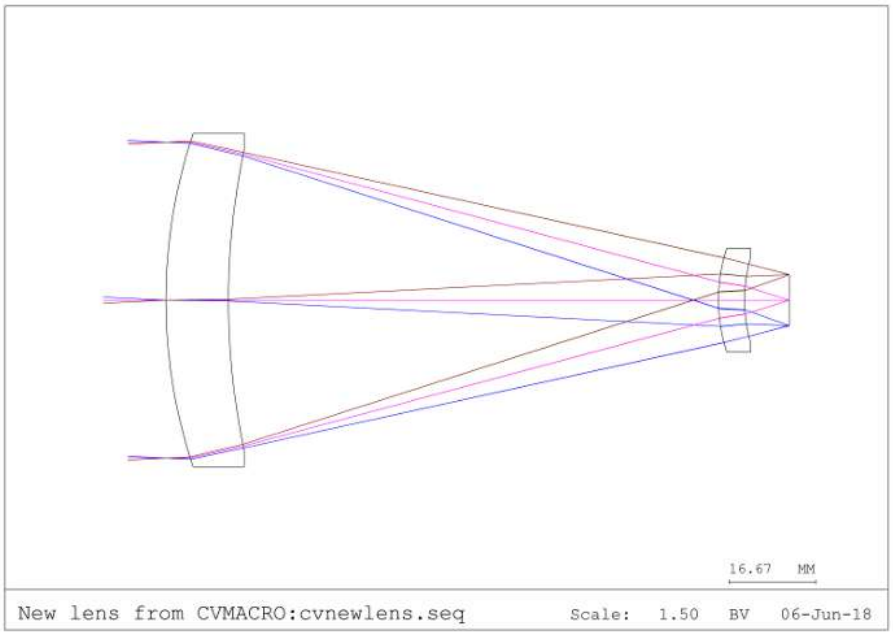

Fig. 6.9: Layout of the Si(h)GaAs optical design re-optimized for -22.5°C

The distance from focal plane would need to the image plane are shown in table 6.7.

Table 6.7: Distances from real image plane to ideal for Si(h)GaAs (UNIT:mm)

Material	Distance (T=0°C)	Distance (T=-45°C)
Aluminum	-0.1832	0.1442
Invar	-0.1350	0.1101

In case it is of interest, spot diagrams can be seen in appendix C2.

1.4 Si(h)ZnS

Finally, the performance with the variation of temperature of Si(h)ZnS designed is studied. Similarly to what has been done for the other systems, the configuration has been re-optimized for -22.5°C. The design data is presented in table 6.8 and the layout is shown in figure 6.10.

Table 6.8: Design data of Si(h)ZnS hybrid doublet re-optimized for -22.5°C(UNIT: mm)

Surface	Surface Type	Y Radius	Thickness	Glass	Y Semi-Aperture
Object	Sphere	Infinity	Infinity		
Stop	Asphere	98.1085	10.0000	Silicon	30.0000
	K=2.2785				
	A=-3.1804e-07	B=-5.6700e-11	C=-2.8937e-14		
2	Sphere (HOE)	142.6438	94.5000		28.5119
	HV1=REA	HV2=REA	HOR=1		
	HX1=0.0000	HY1=0.0000	HZ1=1e10		
	HX2=0.0000	HY2=0.0000	HZ2=1e10		
	HWL=4000	HCT=R	BLT=IDEAL		
	C1=-3.3584e-05	C2=1.7506e-09	C3=-1.3405e-12		
3	Asphere	30.1026	5.0000	Zinc Sulphide	8.0019
	K=-3.3585				
	A=6.9140e-06	B=7.1057e-08	C=0.0000		
4	Asphere	28.6424	5.2052		6.9551
	K=-1.3075				
	A=-7.0954-06	B=0.0000	C=0.0000		
Image	Sphere	Infinity	0.0000		6.2543

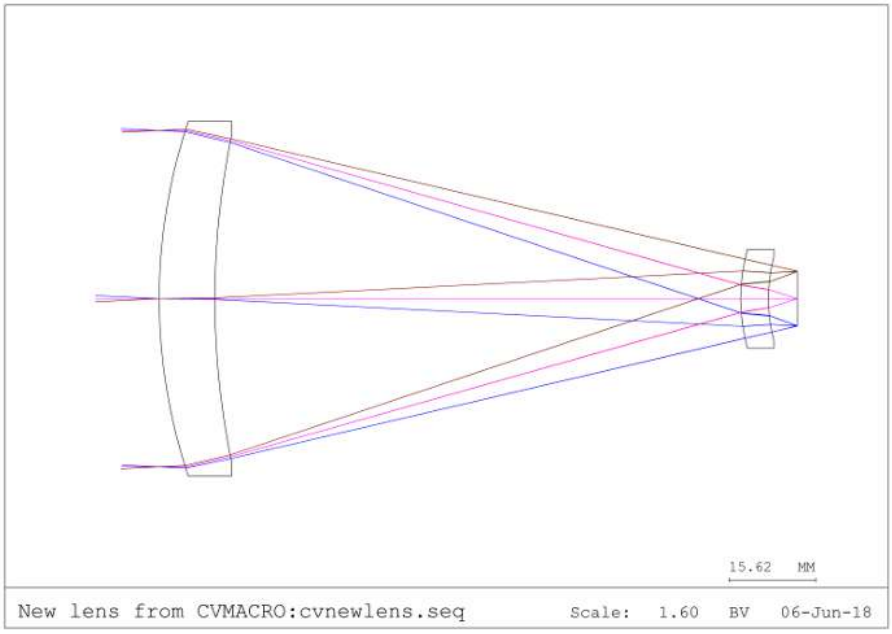

Fig. 6.10: Layout of the Si(h)ZnS optical design re-optimized for -22.5°C

The defocus values for this design are shown in table 6.9.

Table 6.9: Distances from real image plane to ideal for Si(h)ZnS (UNIT:mm)

Material	Distance (T=0°C)	Distance (T=-45°C)
Aluminum	-0.1580	0.1859
Invar	-0.1132	0.1411

In appendix C3, the spot diagrams are shown in case more of desiring more details about the performance.

2 Results discussion

In order to analyze the results obtained, table 6.10 shows a summary of the distance between the real image plane and the ideal one for all the designs. It is seen that the distance is always negative for 0°C given that the system is re-optimized at a lower temperature. When temperature increases, the system expands and, as a result, the image plane goes further away the lens. Therefore, in an ideal system, the image plane should be closer to the lens in order to avoid this expansion. On the contrary, at -45°C, the decrease of the temperature produces contraction. As a consequence, the image plane is situated closer to the lens than it should be and some distance must be added to the real image plane to get better results. It is also seen that the absolute distance to be corrected is larger for the hybrid designs than for the triplets. Comparing the effect of the two mounting materials, the distance is always smaller when using invar than when using aluminum. This is due to the low thermal expansion coefficient of the invar.

Table 6.10: Defocus distances in the different designs (mm)

Design	Mount Material	Defocus distance at 0°	Defocus distance at -45°
SiGeGaAs (2)	Aluminum	-0.0850	0.5957
	Invar	-0.0274	0.5386
SiGeZnS	Aluminum	-0.0923	0.0928
	Invar	-0.0318	0.0326
Si(h)GaAs	Aluminum	-0.1832	0.1442
	Invar	-0.1350	0.1101
Si(h)ZnS	Aluminum	-0.1580	0.1859
	Invar	-0.1132	0.1411

Table 6.11 analyzes the optical performance of the designs affected by the temperature in the case the image plane is at the focal plane. It shows, for each design, the highest RMS radius among all FoV at the design, minimum and maximum temperatures. From this, it can be seen that only the Si(h)GaAs has a smaller RMS radius than 7.5 μm. In addition, table 6.11 also shows the percentage of increase of the highest RMS radius for each case. By comparing them, it can be concluded that the increase of the spot size in doublet hybrid configurations is always smaller than in only refractive triplet configurations. The reason of this lies on two reasons. First of all, the only refractive systems use one more lens than the hybrid systems, which adds more changes of variables: one more lens curvature and thickness changes, one more space in between lenses change and one more refractive index changes. Therefore, all these additional changes contribute to a worse performance of the system. Secondly, since in an hybrid lens the

refractive surface has negative power and the diffractive surface has positive power, the effects of temperature variation are compensated.

Table 6.11: Comparison of the highest RMS radius of spot in the different designs (mm)

Design	RMS radius at -22.5°C	Mount Material	RMS radius at 0°C	RMS radius at -45°C	% Increase at 0°C	% Increase at -45°C
SiGeGaAs (2)	0.0058	Aluminum	0.0070	0.0107	21.75%	85.77%
		Invar	0.0072	0.0114	25.50%	98.04%
SiGeZnS	0.0045	Aluminum	0.0058	0.0076	28.27%	67.51%
		Invar	0.0064	0.0085	39.74%	85.92%
Si(h)GaAs	0.0064	Aluminum	0.0074	0.0074	15.14%	15.20%
		Invar	0.0069	0.0069	8.36%	7.33%
Si(h)ZnS	0.0073	Aluminum	0.0106	0.0089	46.42%	21.93%
		Invar	0.0098	0.0092	35.16%	26.96%

From all this illustrative analysis, it can be concluded that, with an appropriate thermo-mechanical assembly, the optical design using hybrid silicon and gallium arsenide lens could be athermalized with good performance. Also, the SiGeZnS triplet might work if it is slightly re-optmized, given that the results obtained are very close to the desirable ones. Concerning the two other configurations with quite bad performance, SiGeGaAs (2) and Si(h)ZnS, it is that they can not be directly discarded for our application, but their design must be deeply re-optimized so that it works. As said before, this is only a guiding study.

Chapter 7

Final proposal

This chapter proposes a design based on the results obtained so far and a study of the SNR using the data of this design.

1 Optical performance of the proposed design

Based on the results obtained in chapter 6, the final proposal is the doublet configuration using a silicon hybrid lens and a gallium arsenide lens. The proposed configuration is the one before the thermal re-optimization, given that the thermal study is only illustrative despite it has proved that it is easy to re-optimize to obtain good results. In the following pages, the data and the performance of this design is presented. Some of the information has already been seen but, it is good to have all the information about the system together.

The design data is presented again in table 7.1 and its layout in figure 7.1. The parameters of the diffractive surface (remember section 1.4.2) are summarized in table 7.2.

Table 7.1: Design data of Si(h)GaAs (UNIT: mm)

Surface	Surface Type	Y Radius	Thickness	Glass	Y Semi-Aperture
Object	Sphere	Infinity	Infinity		
Stop	Asphere	97.6121	12.0000	Silicon	30.0000
	K=2.0111				
	A=-2.8511e-07	B=-4.9499e-11	C=-2.2486e-14		
2	Sphere (HOE)	135.4466	93.5824		28.0671
	HV1=REA	HV2=REA	HOR=1		
	HX1=0.0000	HY1=0.0000	HZ1=1e10		
	HX2=0.0000	HY2=0.0000	HZ2=1e10		
	HWL=4000	HCT=R	BLT=IDEAL		
	C1=-3.4699e-05	C2=4.5936e-09	C3=-3.6470e-12		
3	Asphere	31.2343	5.0000	Gallium Arsenide	8.8944
	K=-0.9378				
	A=1.4057e-06	B=-9.1162e-09	C=0.0000		
4	Asphere	29.2192	8.6212		7.6917
	K=-0.9104				
	A=3.8030-06	B=0.0000	C=0.0000		
Image	Sphere	Infinity	0.0000		6.2145

Table 7.2: Characteristics of the diffractive surface

Characteristics	Value
Radius of the first zone, r_1	10.7367 mm
Maximum number of zones m_{max}	7
Depth of the zones d_{max}	1.7 μm

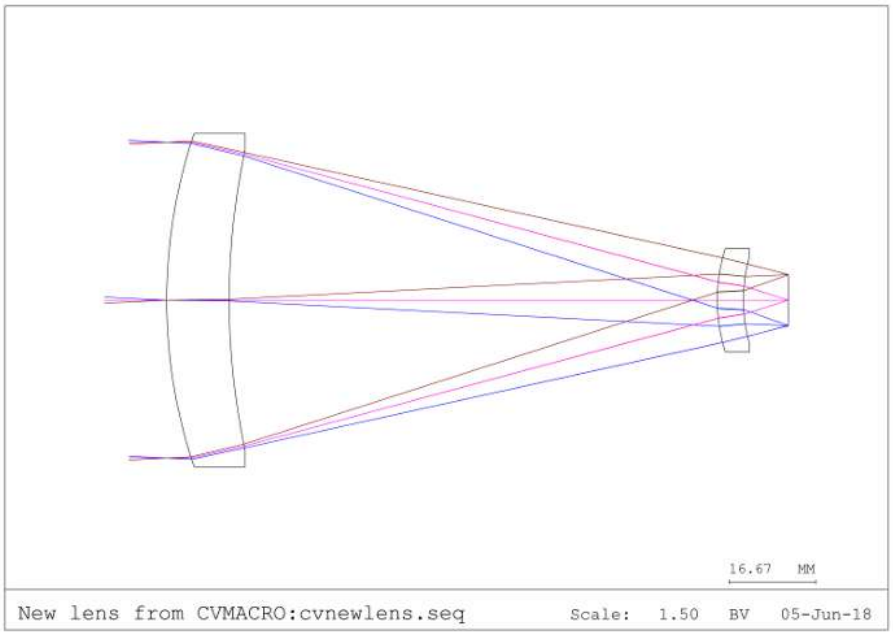

Fig. 7.1: Layout of Si(h)GaAs

The spot diagram is shown in figure 7.2. It is seen that the RMS is smaller than 6.5 μm for all FoVs.

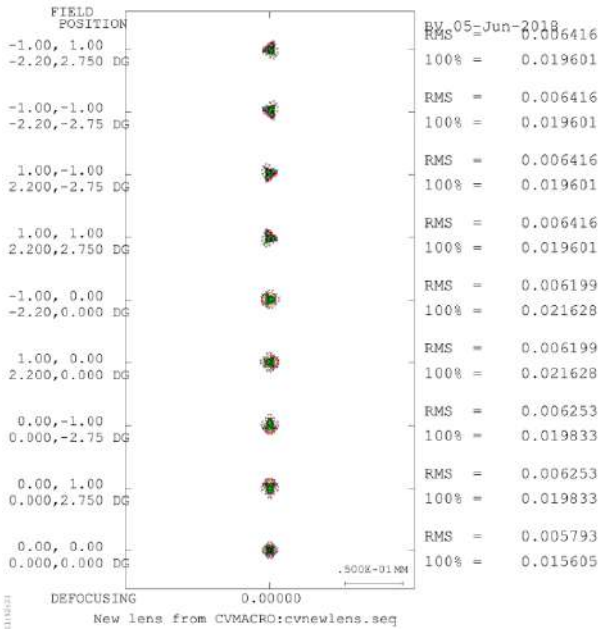

Fig. 7.2: Spot Diagram of Si(h)GaAs)

Figure 5.26 shows the ray aberration curves. Since the ray aberrations for each wavelength can be distinguished, it can be deduced that there is some chromatic aberrations. However, this is not a critical point given that the order of the magnitude of them is small enough.

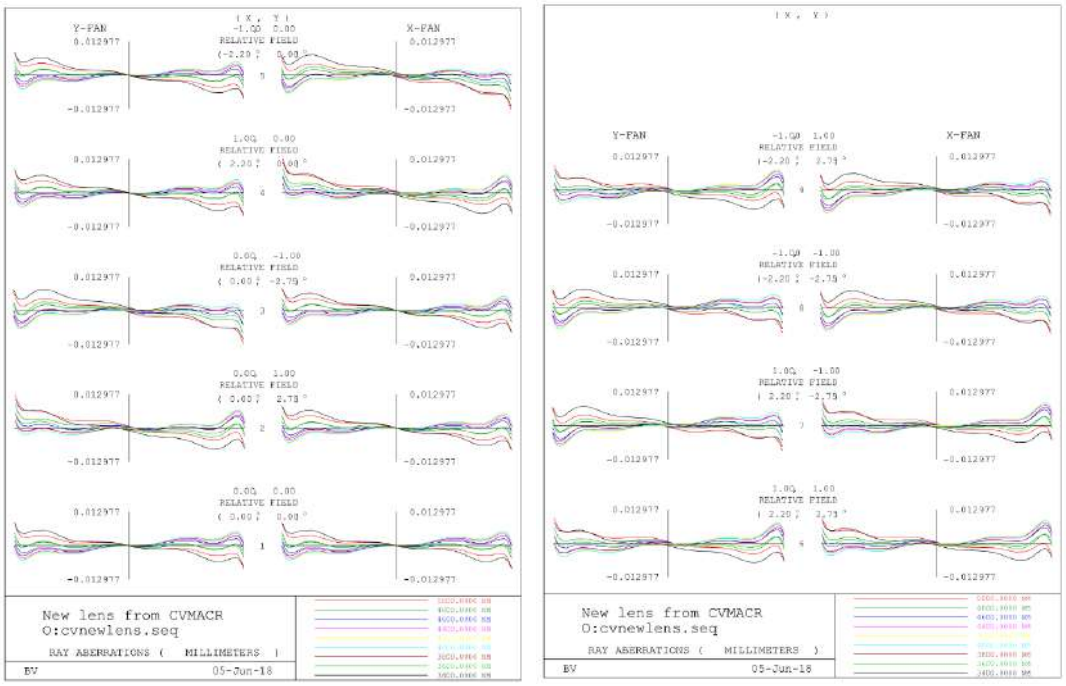

(a) Ray Aberration Curves (1)

(b) Ray Aberration Curves (2)

Fig. 7.3: Ray Aberration Curves of Si(h)GaAs

The MTF plot is shown in figure 7.4. It is seen that, for all FoVs, the curve approaches the diffraction limit diffraction performance. Consequently, the performance of the design is very

good.

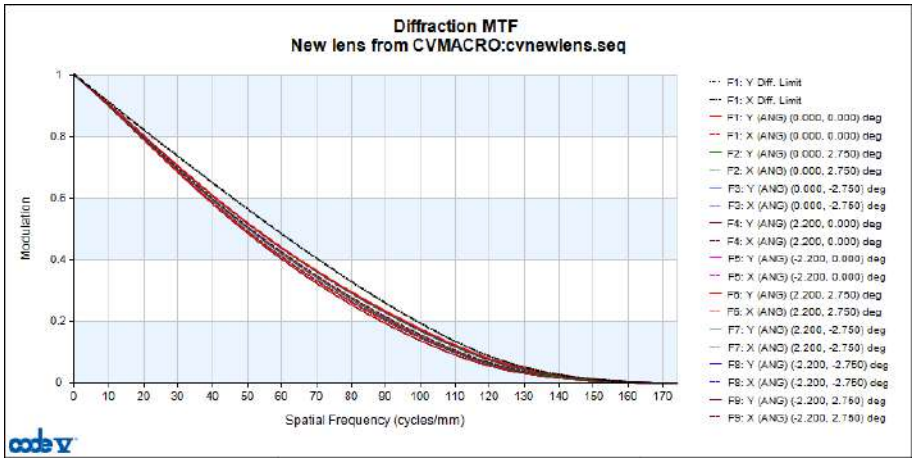

Fig. 7.4: MTF of Si(h)GaAs)

A very useful plot for systems using pixels is the encircled energy plot, which is shown in figure 7.5. It can be seen that at 0.015 mm diameter, the encircled energy is approximately 78%. As explained in section 1.3, about 80% of the energy should fall within the pixel area so that a system can be considered good, which is almost the value got for this optical design.

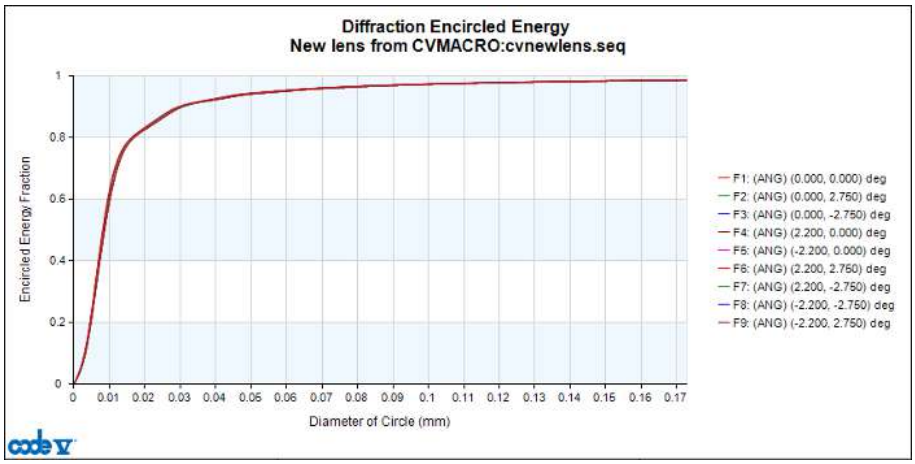

Fig. 7.5: Encircled energy plot of Si(h)GaAs)

Finally, figure 7.6 shows both astigmatism and distortion values of the system. It is seen that astigmatism reaches values up to 12 μm at the highest FoV. The maximum distortion value is also at the highest FoV with 0.5%. This is an acceptable value, since distortion can be corrected by calibration (unless it has very high values, which is not the case).

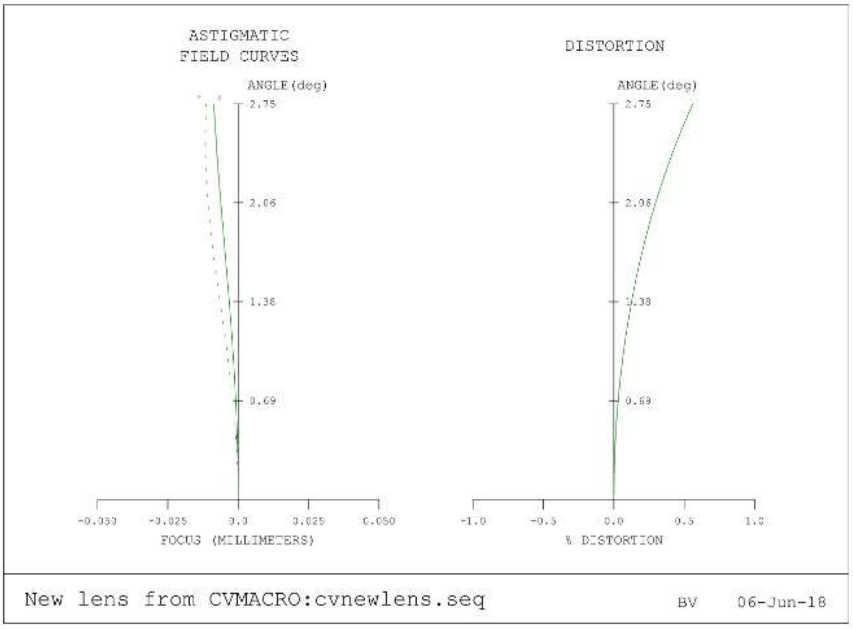

Fig. 7.6: Astigmatism and distortion graphics of Si(h)GaAs)

2 Study of the camera performance with the proposed design

Having an optical design with a very good performance is useless if, when coupled with the detector, the global thermal imaging system does not work properly. Although before starting the design a parametric study was done to avoid this, it is important to check if the SNR of the detector is good. This study is also interesting to see if the detector's needs any specific characteristics that might not be considered at the moment.

In section 2, some characteristics of the detector are stated. As a reminder, the SNR is expressed as:

$$SNR = \frac{D^* \sqrt{d_n d_m} W}{4(f/\#)^2 \sqrt{\Delta f}} \tag{7.1}$$

where D^* is the specific detectivity, expressed in cm $\mathrm{Hz}^{1/2}$/W, d_n and d_m are the detector's dimensions, expressed in cm, W is the radiance emittance reaching the detector, expressed in $\mathrm{W/cm}^2$, f/# is the f-number of the optical system and Δf is the frequency bandwidth considered, expressed in Hz. The computation of this parameters is:

- Detectivity, D^*. The specific detectivity depends on the detector. Different options of detectors are being considered which use different materials substrate for the Focal Plane Array (FPA): Indium Antimonide (InSb), Mercury Cadmium Telluride (MCT) and Indium Arsenide Antimonide (InAsSb). Despite there is still no specific data sheet from the manufacturer yet, [11] show graphs of the detectivity of detectors using InSb and MCT. However, there is not yet any graphic for InAsSb, but it is thought to be similar to that of InSb given that both use the same base materials. Figure 7.7 shows the detectivity of InSb and MCT with the wavelength.

  As seen, and because are quantum detectors, the detectivity depends on the wavelength. For this study, a mean value is going to be used. Thus, D^*_{InSb}=1.3·10^{11} cm $\mathrm{Hz}^{1/2}$/W and D^*_{MCT}=1.76·10^9 cm $\mathrm{Hz}^{1/2}$/W.

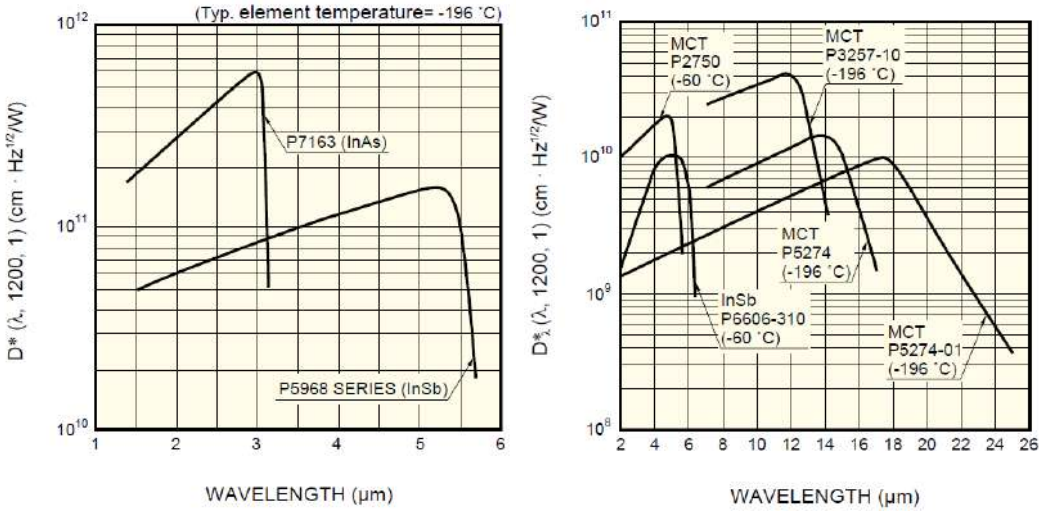

(a) InSb detector (b) MCT detector

Fig. 7.7: Detectivity of the detectors as a function of the wavelength

- Detector dimensions, d_n and d_m. It is known that the detector has a 15 μm pixel size and that the array is 640 $\times$ 512. Therefore, d_n= 0.96 cm and d_m=0.768 cm.
- Radiant emittance, W. The radiant emittance can be related to the radiance, L_T, by the expression

$$W = \pi * L_T \tag{7.2}$$

  At the same time, L_T is

$$L_T = L_{sat} * \tau_{opt} \tag{7.3}$$

  where L_{sat} is the total radiance that reaches the CubeSat and τ_{opt} is the transmission of the optical system. Regarding the total radiance reaching the satellite, it is the contribution of both Earth's spectral emittance and the Earth's reflectance of the Sun's spectral emittance (as explained in section 3.2) from 3.4 μm to 5 μm (since the bandwidth has been reduced for this design). This is the integral from 3.4 μm to 5 μm of the total spectral radiance showed in figure 2.21. Table 7.3 shows the results for different ground temperatures. By comparing table 2.1 showed in section 3.2 and table 7.3, it can be appreciated that the loss of radiance due to the bandwidth reduction (table 2.1 shows radiance results from 3 μm to 5 μm wavelengths) is almost negligible.

Table 7.3: Total radiance reaching the satellite for different temperature values, $\Delta\lambda$=3.4-5 μm

Temperature	Total radiance L_T(W/m$_2$ sr)
270	0.2891
280	0.3950
290	0.5455
300	0.7545
310	1.0383
320	1.4159

The lens transmission is affected by both reflectivity and absorptivity of the lens. The

reflectivity of the lens is avoided with an AR coating, as already explained in section 3.3. Figure 2.23 shows the transmission percentage of a silicon lens [34]. It is seen that the transmission varies with the wavelength, but from 3.4 to 5 μm the mean transmission value is 95%. In [3], there is AR coating for GaAs with 98% of transmissivity from 3.4 μm to 5 μm. Probably, the manufacturers consulted may not be the ones that would manufacture the lens, but it gives an illustrative idea of the transmission values. Since it is difficult to find a reliable value of the absortivity coefficient for both Si and GaAs, the transmission values for the lens computed by *Code V* are used. Table 7.4 shows the transmission for both lenses due to reflectivity and absorptivity.

Table 7.4: Transmission through the lenses

Lens	Transimission due to reflectivity	Transmission due to absorptivity
Silicon	0.95	0.9079
Gallium Arsenide	0.98	0.9170

Therefore, τ_{opt}, the multiplication of all the transmissions, is 0.7751.

- f-number, $f/\#$. It is 1.67 as established in section 2.
- Frequency bandwidth, Δf. Since the bandwidth goes from 3.4 μm to 5 μm, and knowing that $f = 1/\lambda$, Δf=1.33·10^5 Hz.

Once established all these parameters, it is possible to determine the SNR. Table 7.5 show the different values that SNR takes for each temperature considered (from 270 K to 320 K) and for the two detectors (InSb or MCT).

Table 7.5: SNR values depending on the temperature and the detector type

Detector type Temperature	InSb	MCT
270 K	1929.09	26.12
280 K	2635.73	35.68
290 K	3639.73	49.28
300 K	5034.58	68.16
310 K	6928.30	93.80
320 K	9447.93	127.91

The critical value of the SNR is for the lowest temperature considered, given that it increases with the temperature. In table 7.5, it is seen that SNR is 1929.09 for 270 K with the InSb detector and 26.12 with the MCT detector. The exact value that the SNR must be in order to have an acceptable sensitivity is still not known, but in [8] is stated that at least must be of the order of 100. As a result of this, MCT could be not used while InSb would be good. In other words, according to this not very accurate study, the detectivity should be at least 7·10^9 cm Hz$^{1/2}$/W.

Chapter 8

Conclusions

The goal of this work has been studying the feasibility of an optical system using lenses. In the following lines, a review of all the followed steps to carry out this master thesis is done, as well as the conclusions obtained.

First of all, in order to establish the parameters of the optical system, a parametric study of the whole camera has been done. From this, it has been concluded that, given the reduced dimensions of the CubeSat, the orbit altitude can not be higher than 650 km to obtain a GSD smaller than 100 m. This reduces the initial proposed orbit altitude, which was 400 - 800 km. Another critical parameter is the f/#. In order to avoid diffraction limit, f/# should be 1.54. However, this is a quite low number for the required good performance on geometrical aberrations and thus it is increased up to 1.67 in order to balance both diffraction and geometrical aberrations.

The design started from the simplest configuration in order to ensure the proposed solution is as simple as possible. According to what has been found in the literature research, it has been seen that the silicon germanium doublet combination gives the best performance in terms of reducing chromatic aberrations. However, even when it is used with an aspheric lens to reduce the spherical aberrations, the performance is not good enough and the system suffers from field curvature.

In order to avoid field curvature, an extra lens relatively near the image plane is added. Multiple materials have been tested. The best results are obtained with gallium arsenide and zinc sulphide. For gallium arsenide, two different designs are presented. The first one has a very good performance and the last lens is about 8.5 mm far from the detector. Since this proximity might cause a problem due to the interaction with the detector (the detector must be at very low temperatures to work properly), in the second design the gallium arsenide lens is situated 20 mm away from the image plane to prove that a system with the lens relatively far from the image plane is feasible. Its performance is little worse, but the spot size is still within the pixel size. Regarding the third design, it is seen that zinc sulphide needs to get closer to the image plane to get a similar performance than the previous designs because its refractive index is lower than that of gallium arsenide.

The use of hybrid lenses is considered in order to reduce the number of lenses and keep the simplicity. The performance of an hybrid silicon singlet is compared to that of the silicon germanium doublet: the chromatic aberrations increase but the spot size is quite similar. An extra lens of different materials is added to the hybrid silicon singlet. The performance obtained is not as good as desired. Since chromatic aberrations are the most dominating aberrations, the bandwidth is reduced from 3-5 μm to 3.4-5 μm. By doing this, the results are acceptable. Three different designs using cadmium telluride, gallium arsenide and zinc sulphide are presented. The performance of these designs are not as good as the ones got with the triplet configuration, but

still the RMS radius is always smaller than 7.5 μm.

Given that the temperature highly affects the optical and mechanical properties of materials and that the CubeSat will be exposed to high temperature variations, an illustrative study of the temperature effects on the optical systems is carried out. For doing this, two different materials with very different thermal expansion coefficients have been considered for the mount: invar and aluminum. It is seen that, if a good optic-mechanic-thermal design for the mounting is designed, some of the presented designs could work with a small re-optimization. More in detail, it is concluded that the performance of triplet configurations using only refractive lens obtain worse results than that of doublet hybrid configurations. From all the systems presented, the doublet using silicon hybrid lens and gallium arsenide lens has the best performance when temperature varies.

Based on the obtained results from the thermal study, the hybrid doublet using silicon and gallium arsenide is proposed as the final design. With the data of this system, the SNR of the detector is computed. From this study, it is concluded that the detectivity of the detector should be, at least, D^*=7·10^9 cm Hz$^{1/2}$/W.

Despite there is a proposed design, this is not a closed solution given that the project is still in initial stage. There is still a lot of work to be done in the following phases:

- To adapt the design to the new conditions (if so) given by the rest of the systems of the CubeSat
- To re-optimize the design in order to athermalize it
- To design the mount for the lenses
- To adapt the design to the restrictions (if so) of the lens manufacturer and to define the manufacturing tolerances

In conclusion, this master thesis proposes an optical design that proves the feasibility of using a refractive-diffractive optical system for the OUFTI-NEXT CubeSat, although the design will have to be re-optimized in the future.

Bibliography

[1] *Aperture and Stops*. Acces date: 25-May-2018. URL: http://electron9.phys.utk.edu/optics421/modules/m3/Stops.htm.

[2] Erwin E. Cooper. "Wide Band Color Correcting Infrared Lens System". In: *US Patent* 4,871,219 (1989).

[3] Isp Optics Corp. *IR ANTI-REFLECTION COATINGS*. Acces date: 06-June-2018. URL: http://www.ispoptics.com/articles/34/IR%20ANTI-REFLECTION%20COATINGS.

[4] Nikon Corporation. *Structure and Optical Technologies. Aberrations*. Acces date: 26-May-2018. URL: http://imaging.nikon.com/lineup/sportoptics/how_to/guide/binoculars/technologies/technologies_08.htm.

[5] David Darling. *David Darling. achromatic*. Acces date: 17-Apr-2018. URL: http://www.daviddarling.info/encyclopedia/A/achromatic.html.

[6] NASA Goddard Space Flight Center Dr. David R. Williams. *Sun Fact Sheet*. Acces date: 24-May-2018. URL: https://nssdc.gsfc.nasa.gov/planetary/factsheet/sunfact.html.

[7] Yoder P.R. Fischer R.E. Tadic Galeb B. *Optical System Design*. 2nd ed. McGraw Hill, 2008. ISBN: 0071472487.

[8] Enrico Ghidoli. "Feasibility of Earth CubeSat Observation in MWIR window". MA thesis. Belgium: Université de Liège, 2017.

[9] John P. Bowen Gregory P. Behrmann. "Influence of temperature on diffractive lens performance". In: *Applied Optics* 32 (14 1993), pp. 2483–2489.

[10] Serge Habraken. *Coherent and incoherent optics*. University Lecture. 2017-2018.

[11] Hamamatsu. *Characteristics and use of infrared detectors*. Brochure. 2011. URL: https://www.hamamatsu.com/resources/pdf/ssd/infrared_kird9001e.pdf.

[12] Edmund Optics Inc. *Anti-Reflection (AR) Coatings*. Acces date: 23-May-2018. URL: https://www.edmundoptics.com/resources/application-notes/optics/anti-reflection-coatings/.

[13] Sunex Inc. *Sunex. Partner for optical solutions. Achromatic Doublet*. Acces date: 17-Apr-2018. URL: http://www.optics-online.com/ach.asp.

[14] Thomas H. Jamieson. "Thermal effects in optical systems". In: *Optical Engineering* 20 (02 1981), pp. 156–160.

[15] Thomas H. Jamieson. "Ultra-Wide Waveband Optics". In: *Optical Enineering* 23.2 (1984), p. 111. DOI: https://doi.org/10.1117/12.7973396.

[16] David A. Kubalak. "Design and Analysis of a Hybrid Diffractive/Refractive Achromat for use in Optical Data Storage". MA thesis. Rochester, New York: University of Rochester, 1993.

[17] Milton Laikin. *Lens Design*. 4th ed. Boca Raton, FL 33487-2742: CRC Press. Taylor & Francis Group, 2007. ISBN: 0-8493-8278-5.

[18] Photography Life. *What is Spherical Aberration?* Acces date: 26-May-2018. URL: https://photographylife.com/what-is-spherical-aberration.

[19] Crystan Ltd. *CRYSTAN. UV·VISIBLE·IRSPECIALISTS*. Acces date = 22-Feb-2018. URL: https://www.crystran.co.uk/optical-materials.

[20] M. Sholl M. Lampton. "Comparison of On-Axis Three-Mirror-Anastigmat Telescopes". In: *Space Sciences Laboratory* ().

[21] Physical Measurement Laboratory of NIST. *CODATA Internationally recommended 2014 values of the Fundamental Physics Constants*. Acces date: 03-June-2018. URL: https://physics.nist.gov/cuu/Constants/.

[22] Physics in a nutshell. *Different Formulations of Planck's Law*. Acces date: 03-June-2018. URL: https://www.physics-in-a-nutshell.com/article/24/different-formulations-of-plancks-law.

[23] Edmund Optics. *Comparison of Optical Aberrations*. Acces date: 26-May-2018. URL: https://www.edmundoptics.com/resources/application-notes/optics/comparison-of-optical-aberrations/.

[24] Edmund Optics. *Glossary*. Acces date: 2-May-2018. URL: https://www.edmundoptics.com/resources/glossary/e/.

[25] Mikhail Polyanskiy. *Refractive index database*. Acces date: 23-May-2018. URL: https://refractiveindex.info/.

[26] et al. Rakesh G.Mote S.F.Yu. "Near-field focusing properties of zone plates in visible regime - New insights". In: *Optics Express* 16 (13 2008), pp. 9554–9564. DOI: https://doi.org/10.1364/OE.16.009554.

[27] Max J. Riedl. *Optical Design Fundamentals for Infrared Systems*. Bellingham, Washington 98227-0010: SPIE - The International Society for Optical Engineering, 1995. ISBN: 0-8194-1935-4.

[28] Dimitri Schklar. "OUFTI-Next Nanosatellite: Feasibility Study and Mission Assessment". MA thesis. Belgium: Université de Liège, 2017.

[29] Warren J. Smith. *Modern Optical Engineering*. 3rd ed. McGraw Hill, 2000. ISBN: 0-07-136360-2.

[30] Cyber Space. *Optical Configurations*. Acces date: 28-May-2018. URL: http://www.tyler.net/lphilpot/optics.html.

[31] Inc Synopsys. *CODE V Optical Design Software*. Acces date: 28-May-2018. URL: https://www.synopsys.com/optical-solutions/codev.html.

[32] telescopeOptics. *RAY (GEOMETRIC) ABERRATIONS*. Acces date: 27-May-2018. URL: http://www.telescope-optics.net/ray_geometric_aberrations.htm.

[33] Nicholas George Thomas Stone. "Hybrid diffractive-refractive lenses and achromats". In: *APPLIED OPTICS* 27.14 (1988), pp. 2960–2971. DOI: https://doi.org/10.1364/AO.27.002960.

[34] Inc Thorlabs. *Silicon Windows*. Acces date: 24-May-2018. URL: https://www.thorlabs.com/NewGroupPage9.cfm?ObjectGroup_ID=3979.

[35] The Engineering Toolbox. *Coefficients of Linear Thermal Expansion*. Acces date: 05-June-2018. URL: https://www.engineeringtoolbox.com/linear-expansion-coefficients-d_95.html.

[36] Jeffrey L. Tosi and Janos Technology Kumar M. Khajurivala. *Common Infrared Optical Materials and Coatings: A Guide to Properties, Performance and Applications*. Acces date: 22-Feb-2018. URL: https://www.photonics.com/a25495/Common_Infrared_Optical_Materials_and_Coatings_A.

[37] *Wikipedia*. Acces date: 28-May-2018. URL: https://www.wikipedia.org/.

[38] A. P. Wood. "Design of infrared hybrid reffractive-diffractive lenses". In: *APPLIED OPTICS* 31.13 (1992), pp. 2253–8. DOI: 10.1364/AO.31.002253.

Appendix A

The doublet achromat: methodology for a first approximation

Before listing all the steps of the method, it is important to define the notation that it uses:

- Focal length, f
- Power of the lens, ϕ:the reciprocal of the focal (1/f)
- Index of refraction, n
- Radius of curvature, r
- Curvature, c: reciprocal of the radius, equal to 1/r
- The Abbe number, V

There are two constraints when considering a doublet achromat:

1. The power has the same power as the singlet $\phi = \phi_a + \phi_b$
2. By forcing F and C light together, we obtain: $\frac{\phi_a}{\nu_a} + \frac{\phi_b}{\nu_b} = 0$

By combining 1 and 2, the expressions A.1 and A.2 are obtained:

$$\phi_a = \frac{V_a}{V_a - V_b}\phi \tag{A.1}$$

$$\phi_b = -\frac{V_b}{V_a - V_b}\phi \tag{A.2}$$

If focal length is used instead of power, equations A.1 and A.2 lead to:

$$f_a = \frac{V_a - \nu_b}{V_b} f \tag{A.3}$$

$$f_b = \frac{V_b - \nu_a}{V_b} f \tag{A.4}$$

The algorithm for a thin lens achromatic doublet is [17]:

1. Select materials: V_a, n_a, V_b, n_b and system focal length f;
2. Determine f_a and f_b from above equations

3. $C_a = \frac{1}{f_a(n_a-1)}$; $C_b = \frac{1}{f_b(n_b-1)}$
4. $H = G8b \cdot C_b^2 - G8a \cdot C_a^2 - G7b \cdot C_b/f$
5. $XI = G5a \cdot C_a/4$; $XK = G5b \cdot C_b/4$
6. $A = G1a \cdot C_a^3 + G1b \cdot C_b^3 - G3b \cdot C_b^2/f + G6b \cdot C_b/f^2$
7. $B = -G2a \cdot C_a^2$; $E = G4a \cdot C_a$; $XJ = G4b \cdot C_b$
8. $D = G2b \cdot C_b^2 - G5b \cdot C_b/f$; $P = A + H(XJ \cdot H/XK - D)/XK$
9. $Q = B + XI(2 \cdot XJ \cdot H/XK - D)/XK$; $R = E + XJ(XI/XK)^2$
10. $ROOT = Q^2 - 4 \cdot P \cdot R$ (checking for a negative root)
11. $C_1 = \frac{-Q+sqrt(ROOT)}{2R}$ (King 1993)
12. $C_4 = -(H + XI \cdot C1)/XK$; $C_2 = C_1 - C_a$; $C_3 = C_b + C_4$

C_1, C_2, C_3 and C_4 are the surface curvatures. From [29], the G values are obtained:

$$G1 = \frac{n^2(n-1)}{2} \tag{A.5}$$

$$G2 = \frac{(2n+1)(n-1)}{2} \tag{A.6}$$

$$G3 = \frac{(3n+1)(n-1)}{2} \tag{A.7}$$

$$G4 = \frac{(n+2)(n-1)}{2n} \tag{A.8}$$

$$G5 = \frac{2(n+1)(n-1)}{n} \tag{A.9}$$

$$G6 = \frac{(3n+2)(n-1)}{2n} \tag{A.10}$$

$$G7 = \frac{(2n+1)(n-1)}{2n} \tag{A.11}$$

$$G8 = \frac{n(n-1)}{2} \tag{A.12}$$

Appendix B

Camera optical design and layout solutions:some additional results

1 Triplet

1.1 SiGeGaAs (1)

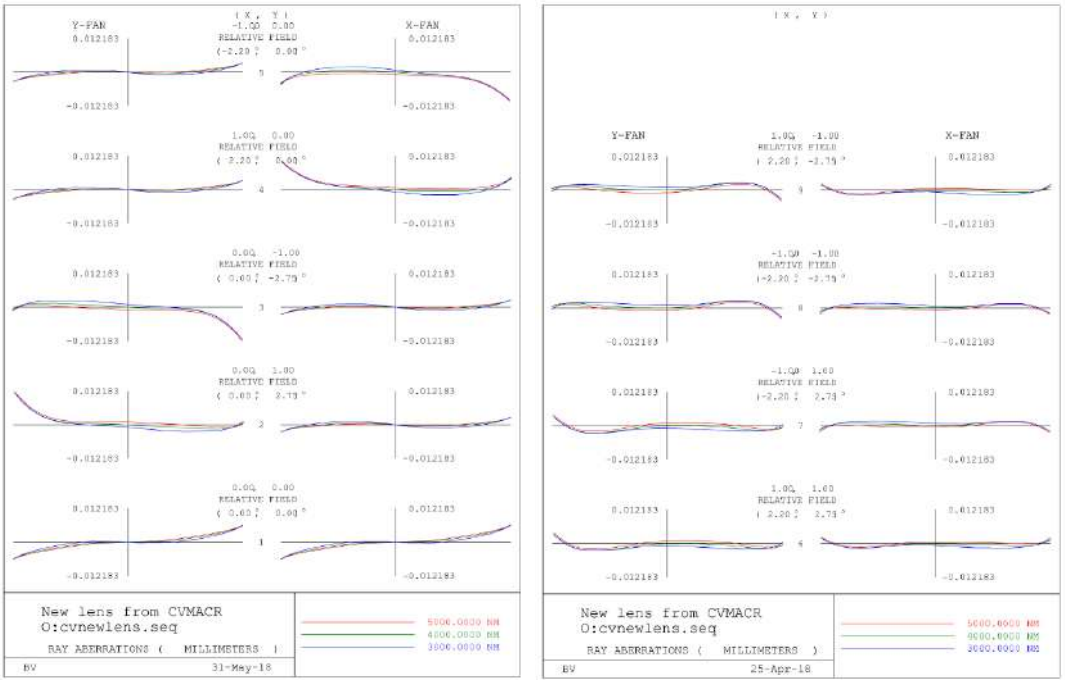

(a) Ray Aberration Curves (1) (b) Ray Aberration Curves (2)

Fig. B.1: Ray Aberration Curves of the SiGeGaAs (1)

1.2 SiGeGaAs (2)

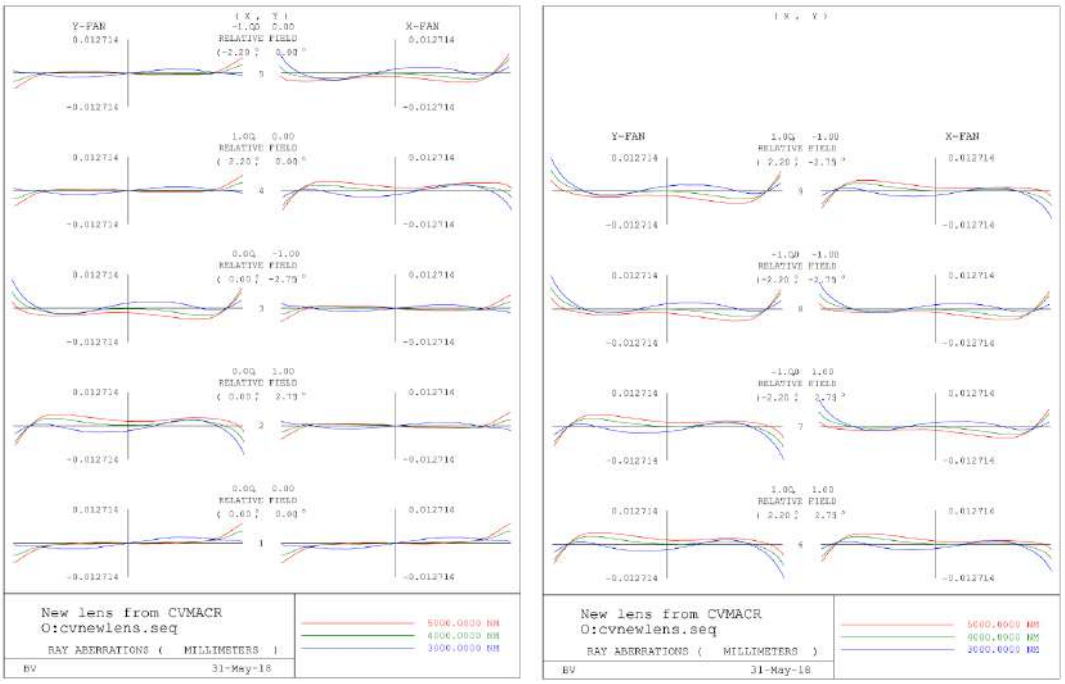

(a) Ray Aberration Curves (1)

(b) Ray Aberration Curves (2)

Fig. B.2: Ray Aberration Curves of the SiGeGaAs (2)

1.3 SiGeZnS

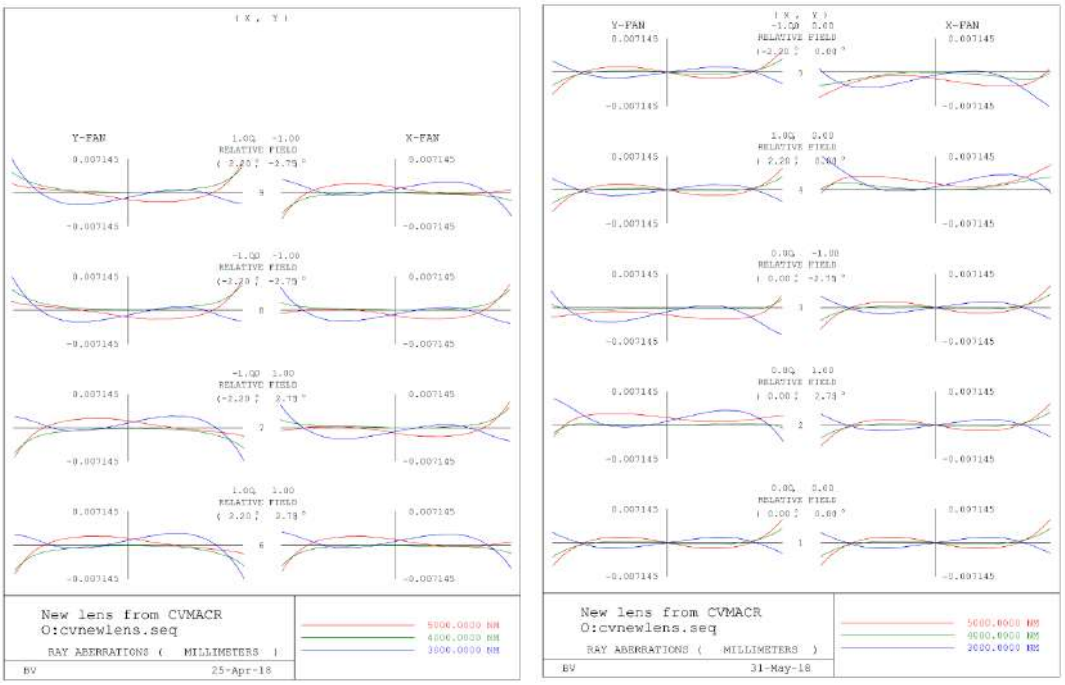

(a) Ray Aberration Curves (1)

(b) Ray Aberration Curves (2)

Fig. B.3: Ray Aberration Curves of the SiGeZnS

1.4 Increasing D_p up to 65 mm

1.4.1 SiGeGaAs (1) (D_p=65 mm)

Table B.1: Design data of SiGeGaAs (1) triplet with D_p=65 mm (UNIT: mm)

Surface	Surface Type	Y Radius	Thickness	Glass	Y Semi-Aperture
Object	Sphere	Infinity	Infinity		
Stop	Asphere	95.3566	10.0000	Silicon	32.5000
	K=0.0214				
	A=-2.7676e-09	B=7.2884e-14	C=-3.9311e-17		
2	Sphere	235.0811	9.000		31.2617
3	Sphere	351.6683	8.000	Germanium	26.9527
4	Sphere	149.5222	80.0000		25.3108
3	Sphere	20.2111	3.4000	Gallium Arsenide	9.7311
4	Sphere	19.8043	10.0250		8.5260
Image	Sphere	Infinity	0.0000		6.1486

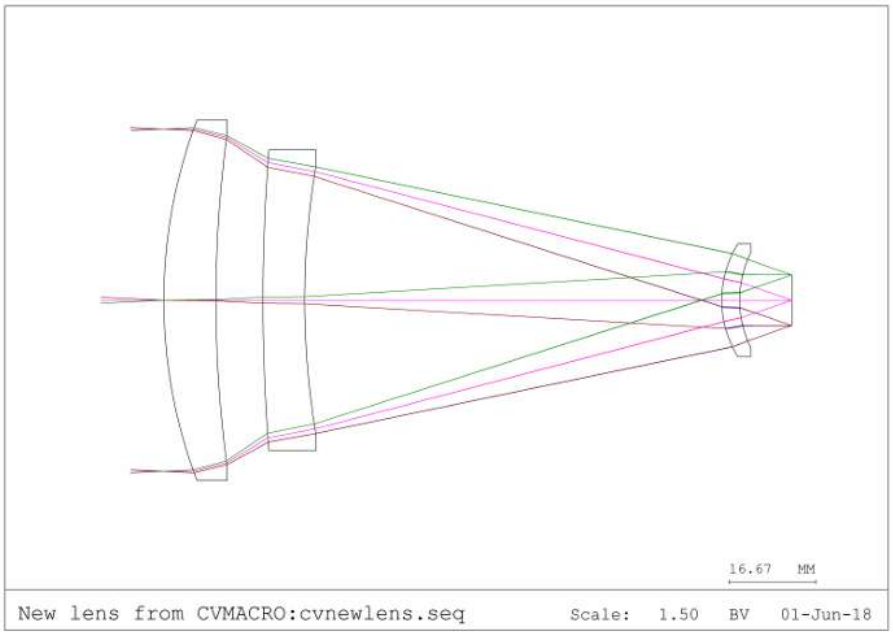

Fig. B.4: Layout of SiGeGaAs (1) triplet with D_p=65 mm

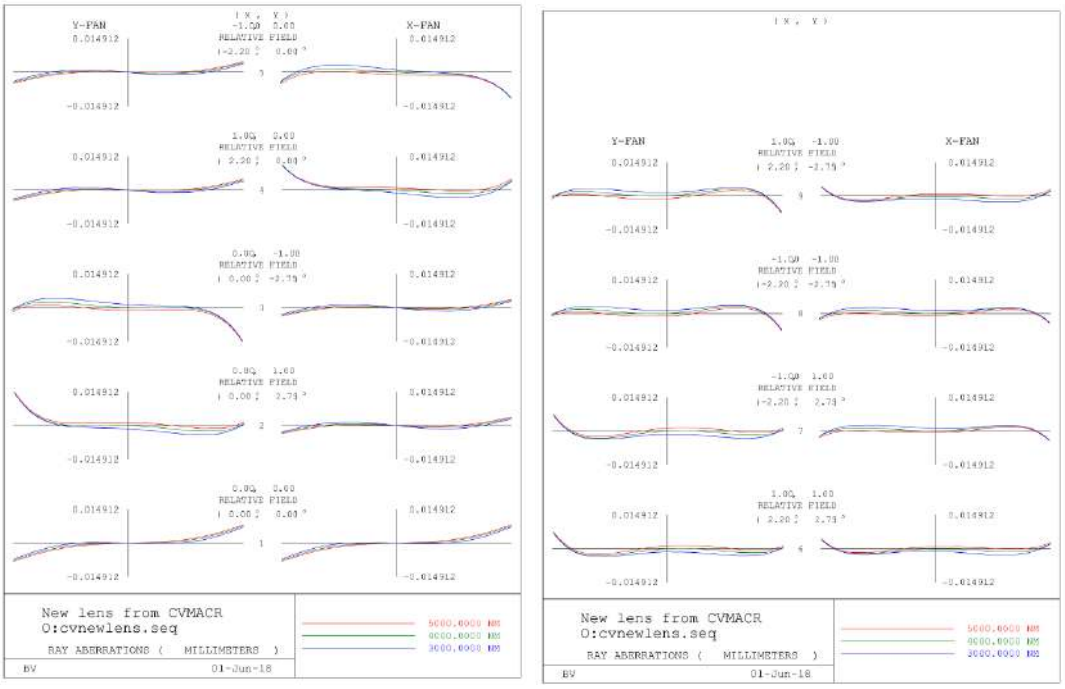

(a) Ray Aberration Curves (1)

(b) Ray Aberration Curves (2)

Fig. B.5: Ray Aberration Curves of the SiGeGaAs (1) with D_p=65 mm

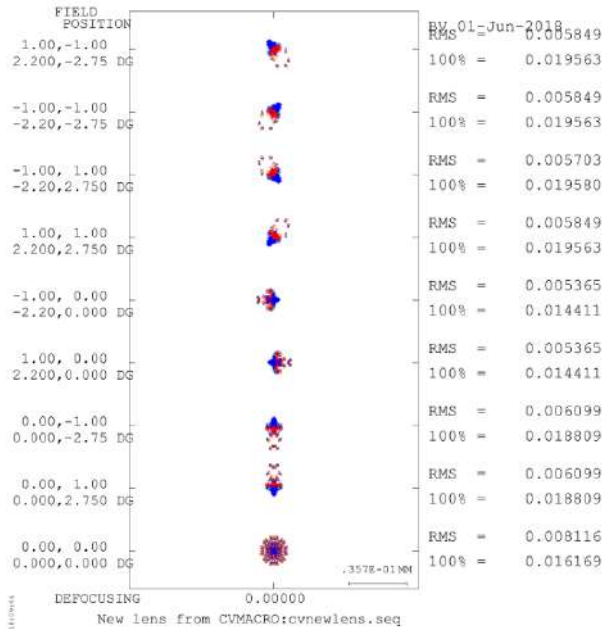

Fig. B.6: Spot Diagram of SiGeGaAs (1) with D_p=65 mm

1.4.2 SiGeGaAs (2) (D_p=65 mm)

Table B.2: Design data of SiGeGaAs (2) triplet with D_p=65 mm (UNIT: mm)

Surface	Surface Type	Y Radius	Thickness	Glass	Y Semi-Aperture
Object	Sphere	Infinity	Infinity		
Stop	Asphere	54.9480	12.0000	Silicon	32.5000
	K=-0.1347				
	A=-4.6847e-08	B=-8.1346e-12	C=-5.4417e-15		
2	Sphere	84.4487	5.000		29.8842
3	Sphere	46.5784	6.2479	Germanium	24.9648
4	Sphere	31.1982	50.0767		20.5544
3	Sphere	127.5706	3.9783	Gallium Arsenide	15.1844
4	Sphere	332.5330	31.2018		14.7802
Image	Sphere	Infinity	0.0000		6.1542

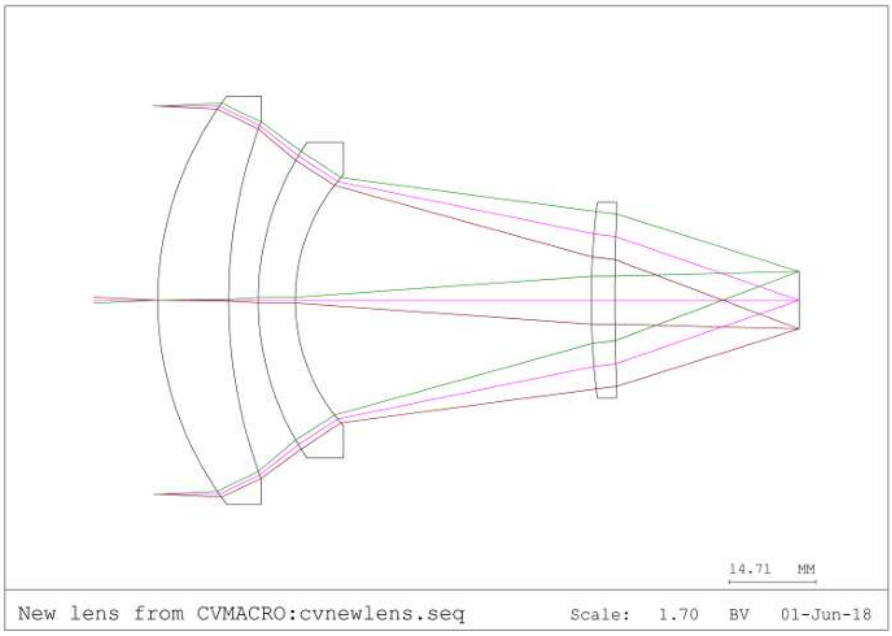

Fig. B.7: Layout of SiGeGaAs (2) triplet with D_p=65 mm

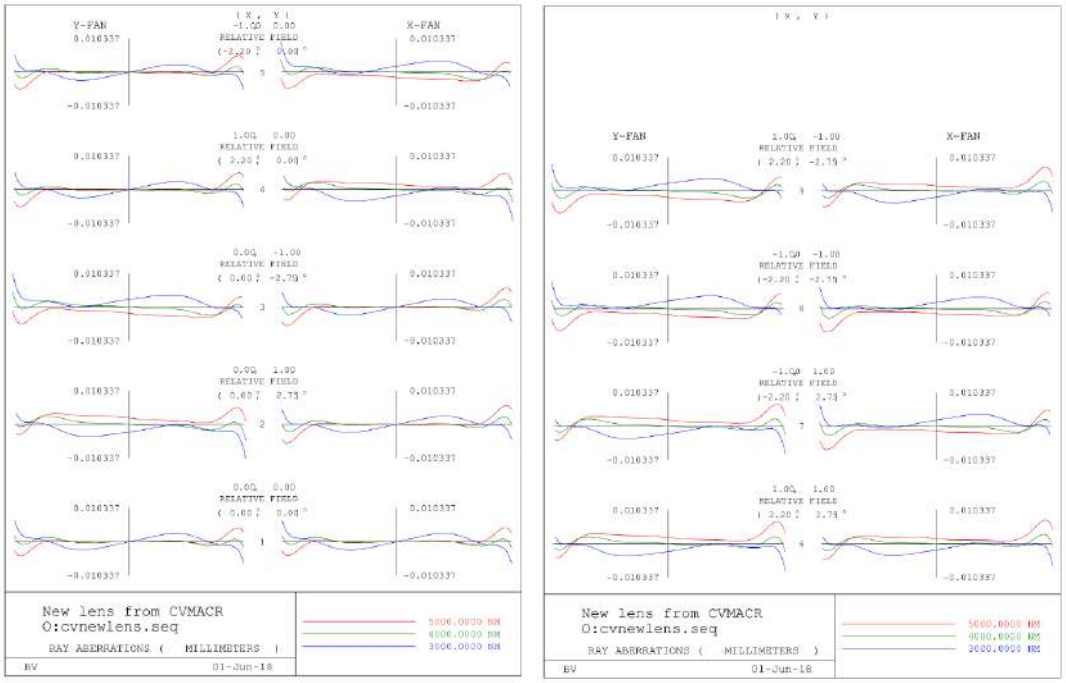

(a) Ray Aberration Curves (1)

(b) Ray Aberration Curves (2)

Fig. B.8: Ray Aberration Curves of the SiGeGaAs (2) with D_p=65 mm

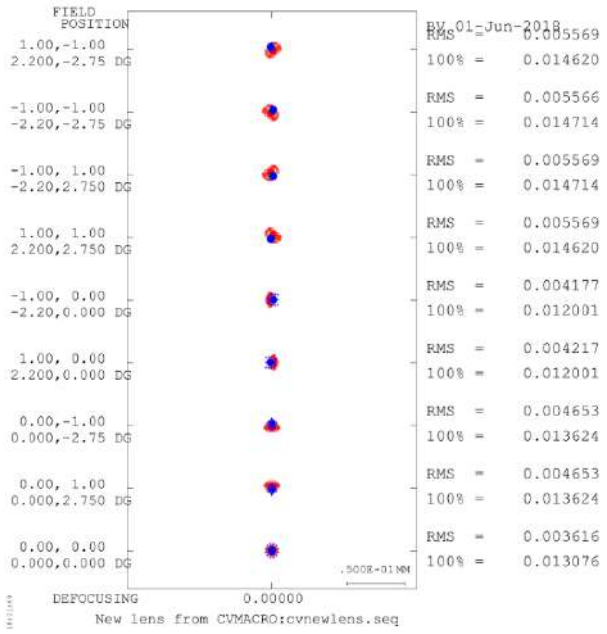

Fig. B.9: Spot Diagram of SiGeGaAs (2) with D_p=65 mm

1.4.3 SiGeZnS (D_p=65 mm)

Table B.3: Design Data of SiGeZnS triplet with D_p=65 mm (UNIT: mm)

Surface	Surface Type	Y Radius	Thickness	Glass	Y Semi-Aperture
Object	Sphere	Infinity	Infinity		
Stop	Asphere	67.9764	9.9981	Silicon	32.5000
	K=-0.2239				
	A=-3.3731e-08	B=-5.1814e-12	C=-9.7830e-16		
2	Sphere	134.4235	7.6219		31.0374
3	Sphere	66.1895	5.3766	Germanium	25.0050
4	Sphere	44.7916	75.0279		22.0586
5	Sphere	21.3054	5.9094	Zinc Sulphide	8.5124
6	Sphere	21.8925	3.9574		6.9098
Image	Sphere	Infinity	0.0000		6.1862

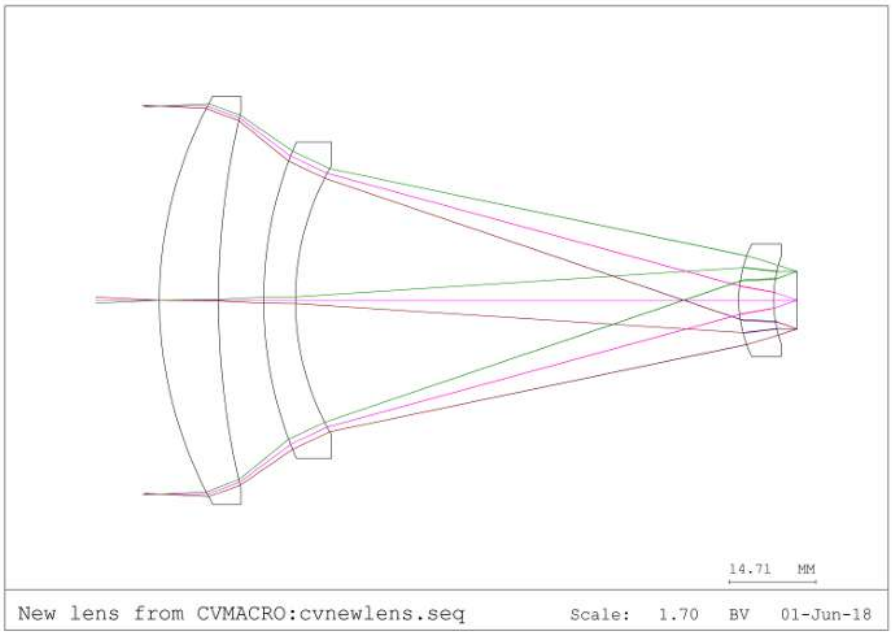

Fig. B.10: Layout of SiGeZnS triplet with D_p=65 mm

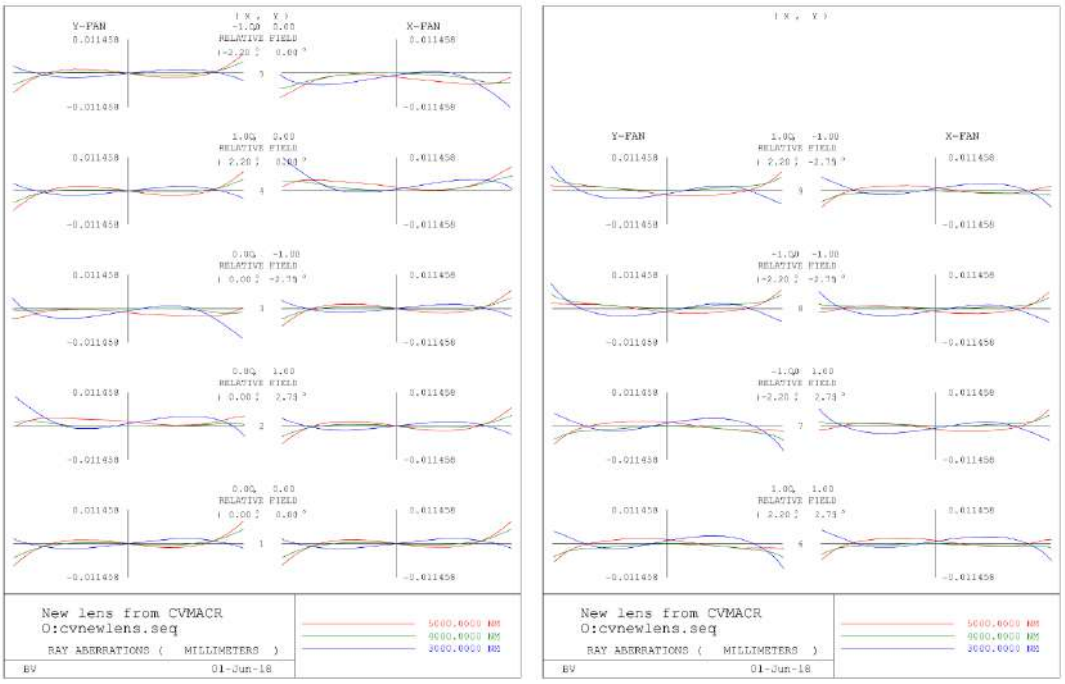

(a) Ray Aberration Curves (1) (b) Ray Aberration Curves (2)

Fig. B.11: Ray Aberration Curves of the SiGeZnS with D_p=65 mm

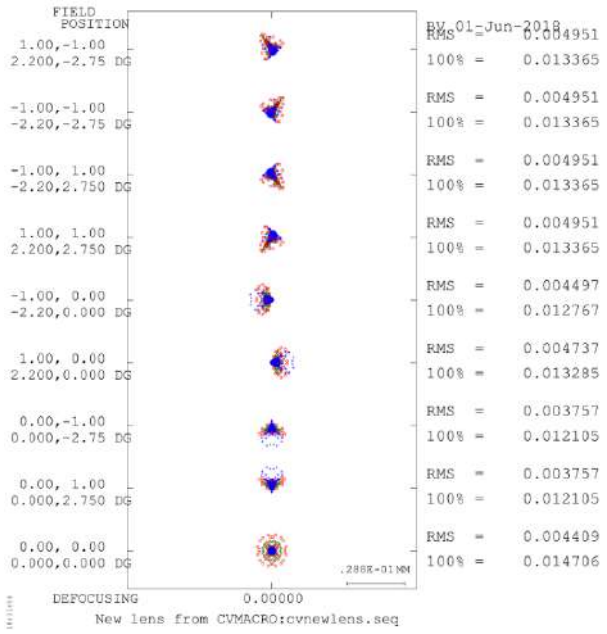

Fig. B.12: Spot Diagram of SiGeZnS with D_p=65 mm

2 Hybrid

2.1 Increasing D_p up to 65 mm

2.1.1 Si(h)CdTe (D_p=65 mm)

Table B.4: Design data of Si(h)CdTe with D_p=65 mm (UNIT: mm)

Surface	Surface Type	Y Radius	Thickness	Glass	Y Semi-Aperture
Object	Sphere	Infinity	Infinity		
Stop	Asphere	89.5296	11.1008	Silicon	32.5000
	K=0.9339				
	A=-1.7803e-07	B=-2.7708e-11	C=-9.67520-15		
2	Sphere (HOE)	120.1063	87.9786		30.5120
	HV1=REA	HV2=REA	HOR=1		
	HX1=0.0000	HY1=0.0000	HZ1=1e10		
	HX2=0.0000	HY2=0.0000	HZ2=1e10		
	HWL=4000	HCT=R	BLT=IDEAL		
	C1=-33.5329-05	C2=5.5309e-09	C3=-3.7104e-12		
3	Asphere	29.8394	4.8928	Cadmium Telluride	9.6650
	K=-2.9325				
	A=9.0291e-06	B=-1.8480e-08	0.0000		
4	Asphere	27.7843	11.3010		8.3748
	K=-0.695911				
	A=-4.1628-07	B=0.0000	C=0.0000		
Image	Sphere	Infinity	0.0000		6.1970

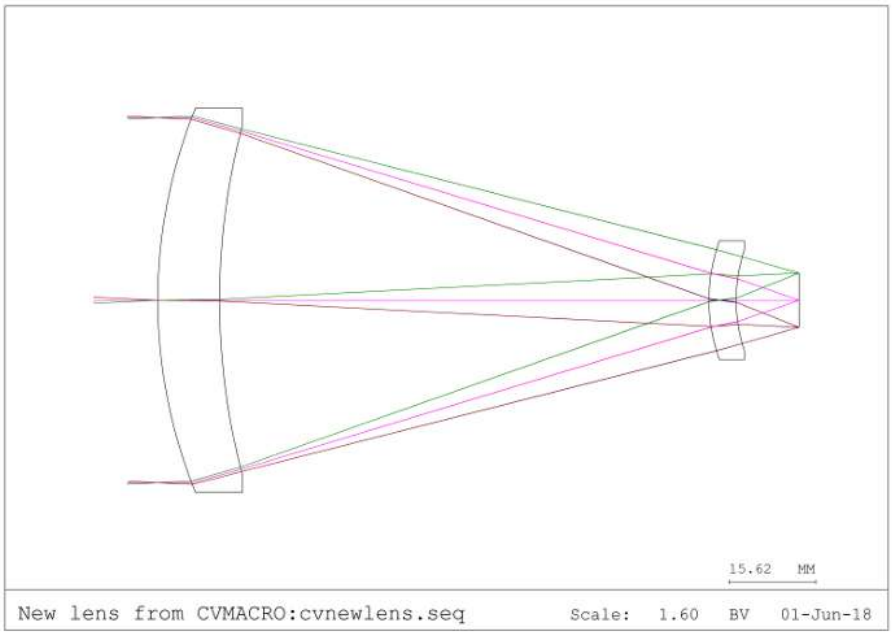

Fig. B.13: Layout of Si(h)CdTe (D_p=65 mm)

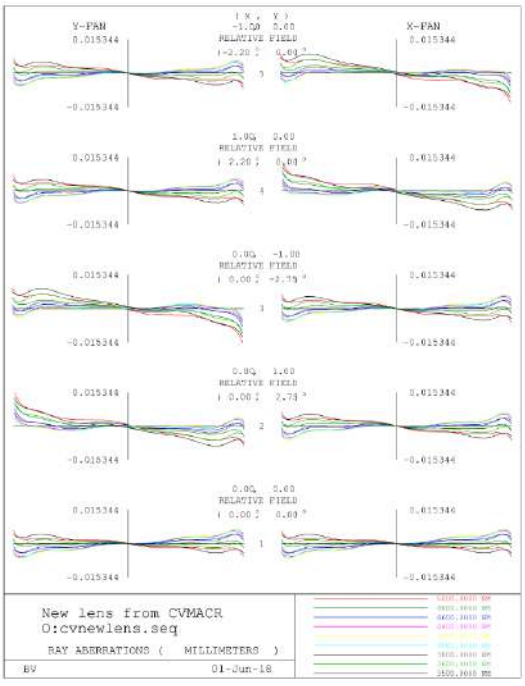

(a) Ray Aberration Curves (1)

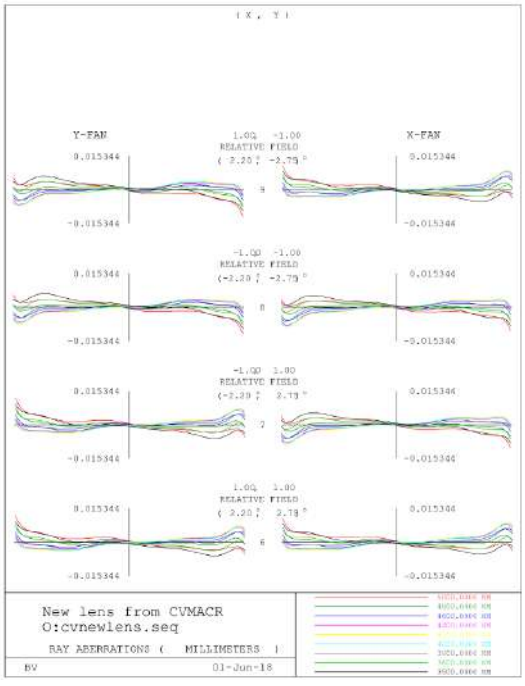

(b) Ray Aberration Curves (2)

Fig. B.14: Ray Aberration Curves of Si(h)CdTe (D_p=65 mm)

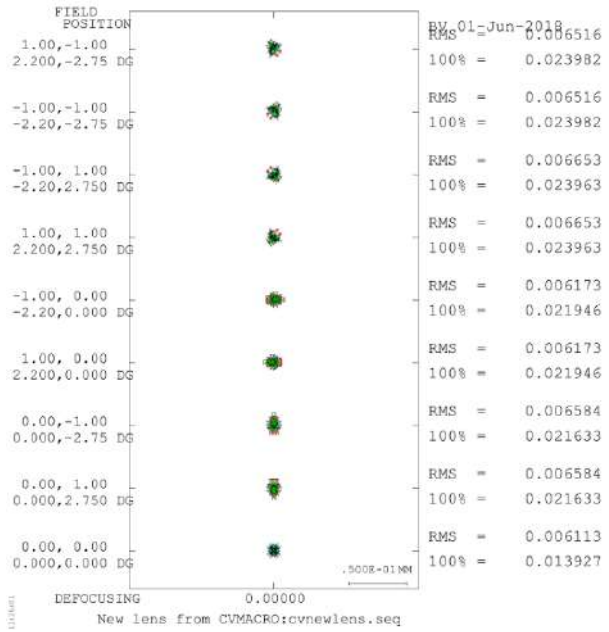

Fig. B.15: Spot Diagram of Si(h)CdTe (D_p=65 mm)

2.1.2 Si(h)GaAs (D_p=65 mm)

Table B.5: Data design of Si(h)GaAs with D_p=65 mm (UNIT: mm)

Surface	Surface Type	Y Radius	Thickness	Glass	Y Semi-Aperture
Object	Sphere	Infinity	Infinity		
Stop	Asphere	97.6955	10.5000	Silicon	32.5000
	K=1.4879				
	A=-2.1363e-07	B=-3.2224e-11	C=-1.2244-14		
2	Sphere (HOE)	136.5106	95.0000		30.8150
	HV1=REA	HV2=REA	HOR=1		
	HX1=0.0000	HY1=0.0000	HZ1=1e10		
	HX2=0.0000	HY2=0.0000	HZ2=1e10		
	HWL=4000	HCT=R	BLT=IDEAL		
	C1=-3.3853e-05	C2=3.8920e-09	C3=-2.5432e-12		
3	Asphere	30.6174	5.0000	Gallium Arsenide	9.3406
	K=-0.9574				
	A=2.3797e-06	B=-6.8893e-09	C=0.0000		
4	Asphere	28.7262	9.2535		8.0387
	K=-1.0459				
	A=5.2413e-06	B=0.0000	C=0.0000		
Image	Sphere	Infinity	0.0000		6.2062

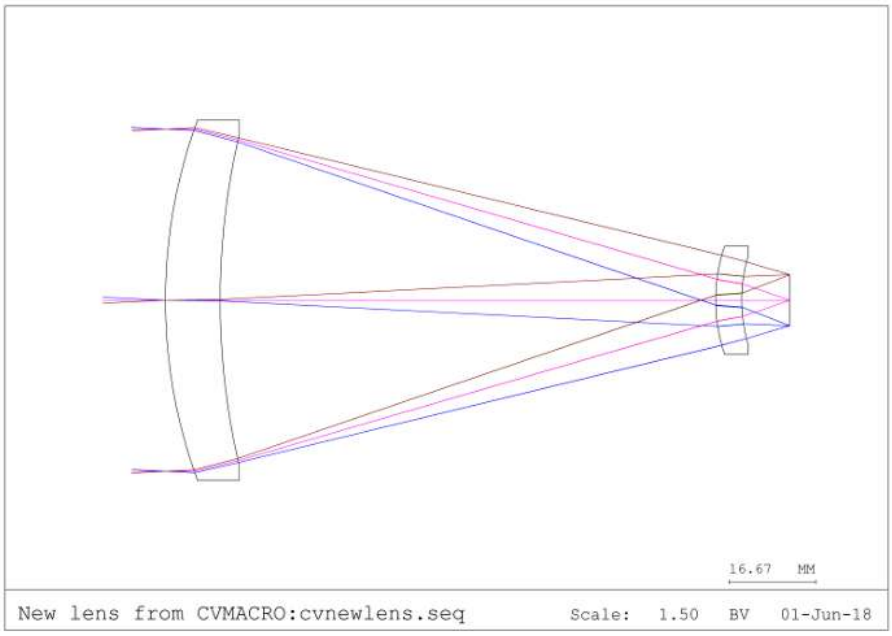

Fig. B.16: Layout of Si(h)GaAs (D_p=65 mm)

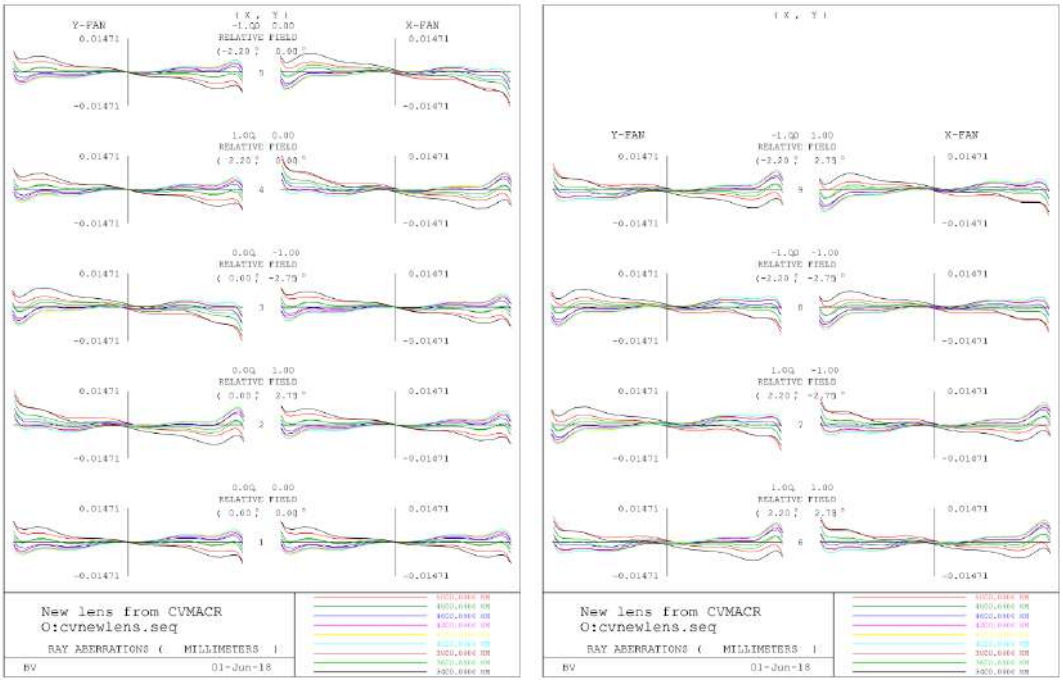

(a) Ray Aberration Curves (1) (b) Ray Aberration Curves (2)

Fig. B.17: Ray Aberration Curves of Si(h)GaAs (D_p=65 mm)

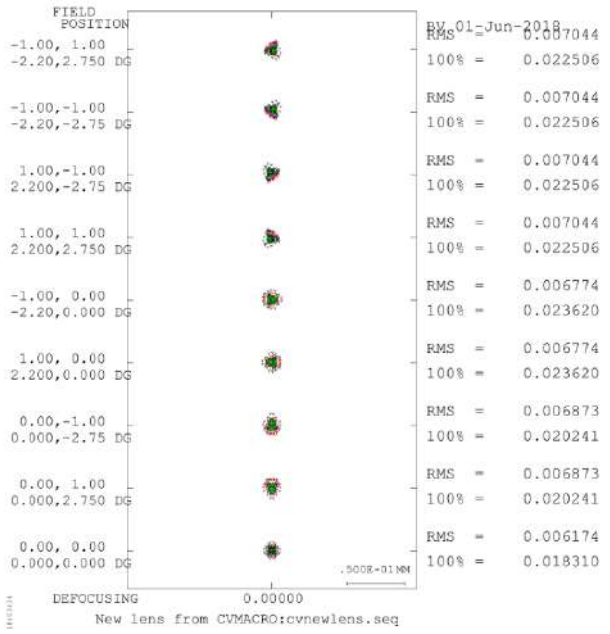

Fig. B.18: Spot Diagram of Si(h)GaAs (D_p=65 mm)

Appendix C

Temperature effects on the designs: some additional results

In this appendix, the spot diagrams for SiGeZnS, Si(h)GaAs and Si(h)Zns are provided and commented in case it is of the interest of the reader.

1 SiGeZnS: spot diagrams at 0°C and -45°C

The spot diagram at the design temperature is shown in figure C.1 meanwhile figure C.2 and figure C.3 show the spot diagrams of a system using aluminum and invar materials for its mount. This has been computed considering that the system is at the minimum and maximum temperatures, considering the image plane is situated at the focal plane.

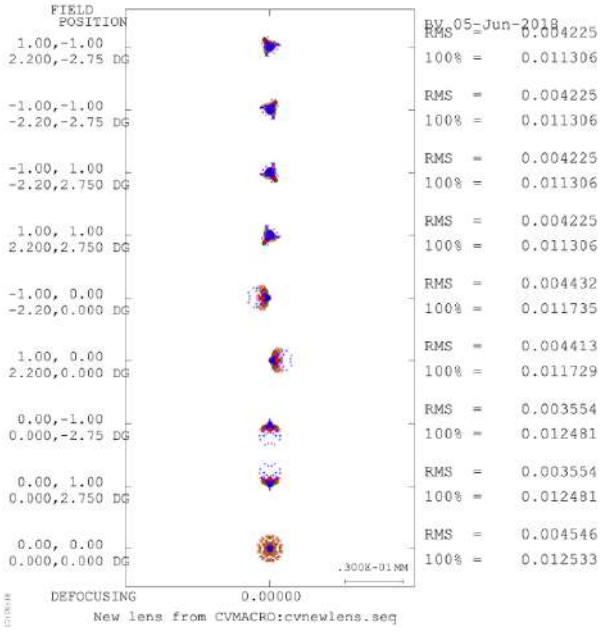

Fig. C.1: Spot diagram of the SiGeZnS optical design re-optimized for -22.5°C

From figure C.1, figure C.2 and figure C.3, it can be seen that when the optical system is at a different temperature from the one for which is designed, the spot size increases but always within the limits, except for the on-axis FoV when temperature is -45°C (in this case RMS radius spot size value is 8.452 μm). Therefore, it can be claimed that the performance of this optical

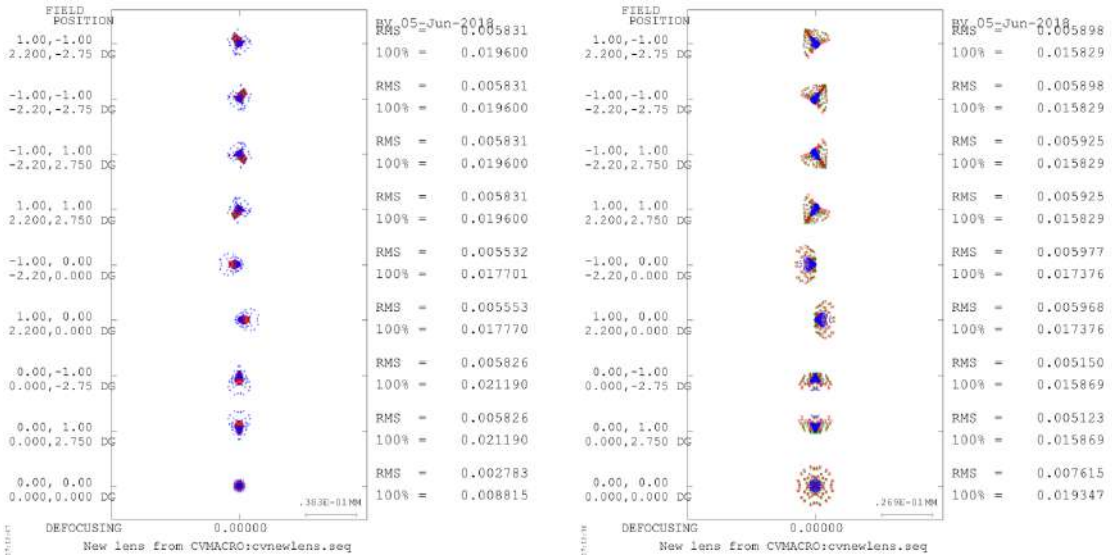

(a) T=0°C (b) T=-45°C

Fig. C.2: Spot Diagrams of the SiGeZnS optical design re-optimized for -22.5°C at maximum and minimum temperatures for aluminum mount with the image plane focused

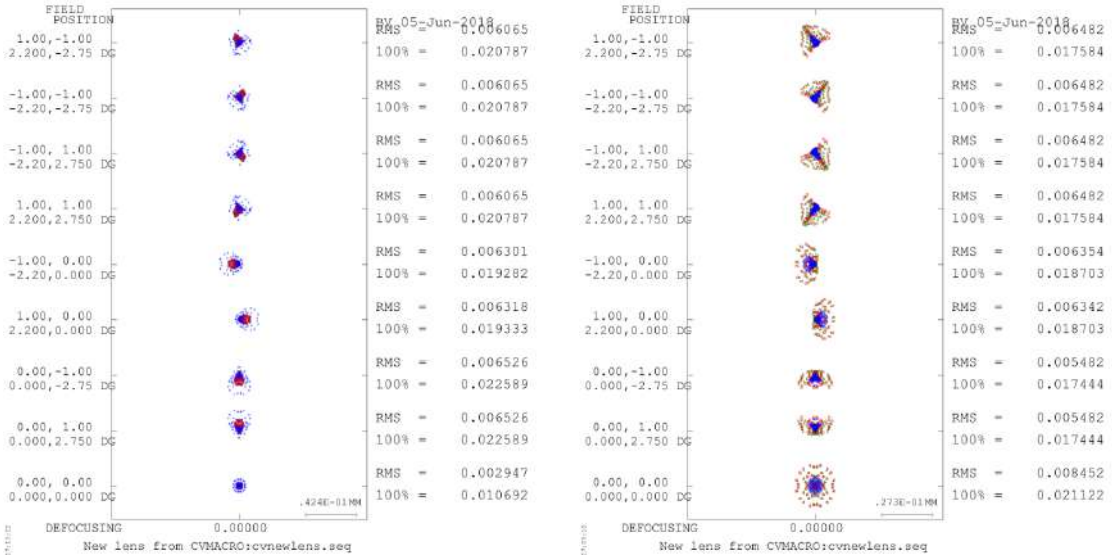

(a) T=0°C (b) T=-45°C

Fig. C.3: Spot Diagrams of the SiGeZnS optical design re-optimized for -22.5°C at maximum and minimum temperatures for invar mount with the image plane focused

system would be fairly good for our application if the image plane was positioned at focus when temperature varies. The spot diagrams defocused are shown in figure C.9 and figure C.10.

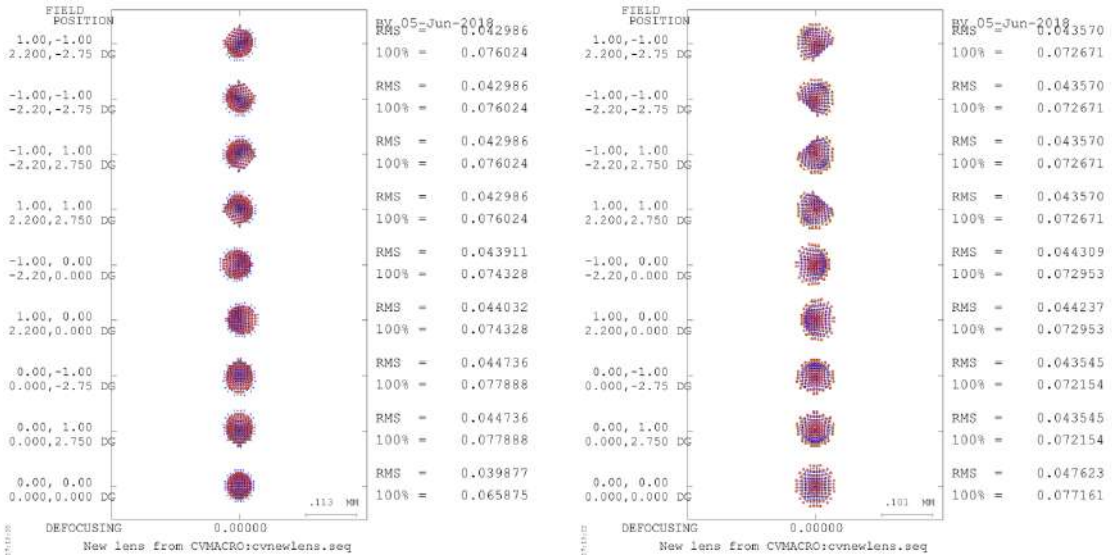

(a) T=0°C (b) T=-45°C

Fig. C.4: Spot Diagrams of the SiGeZnS optical design re-optimized for -22.5°C at maximum and minimum temperatures for aluminum mount

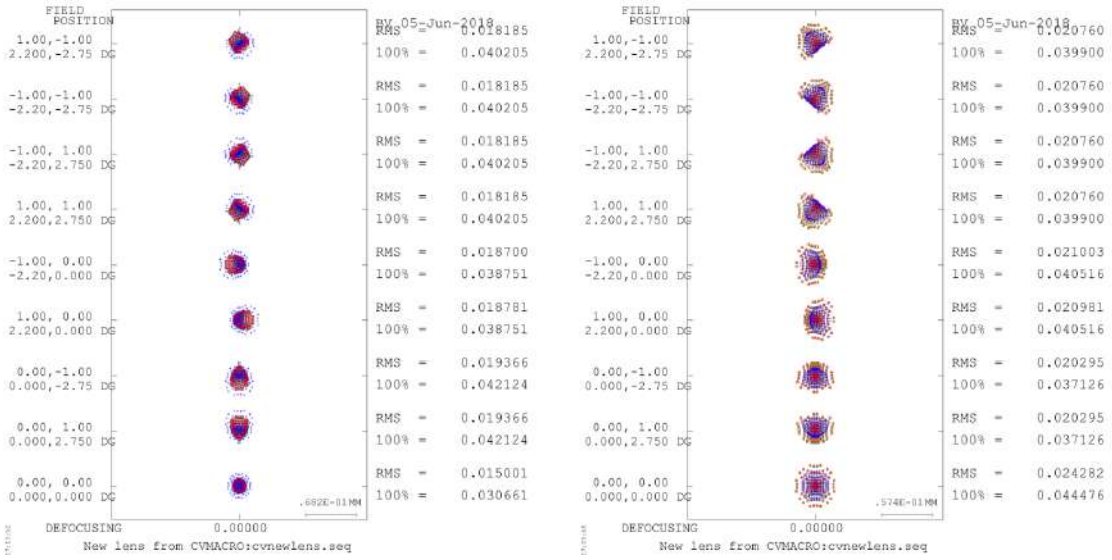

(a) T=0°C (b) T=-45°C

Fig. C.5: Spot Diagrams of the SiGeZnS optical design re-optimized for -22.5°C at maximum and minimum temperatures for invar mount

2 Si(h)GaAs: spot diagrams at 0°C and -45°C

The spot diagram of this new optical system at its design temperature is shown in figure C.6. The spot diagrams at the minimum and maximum temperature considering aluminum and invar mount materials and an ideal image focusing are shown in figure C.7 and figure C.8.

The results are good in all cases. Obviously, the spot size is smaller at the design temperature (see figure C.6) than when temperature varies (see figure C.7 and figure C.8) but, despite

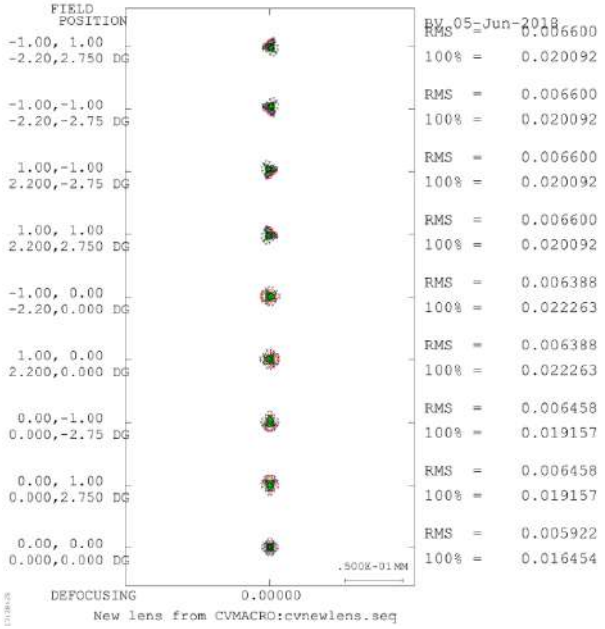

Fig. C.6: Spot diagram of the SiHGaAs optical design re-optimized for -22.5°C

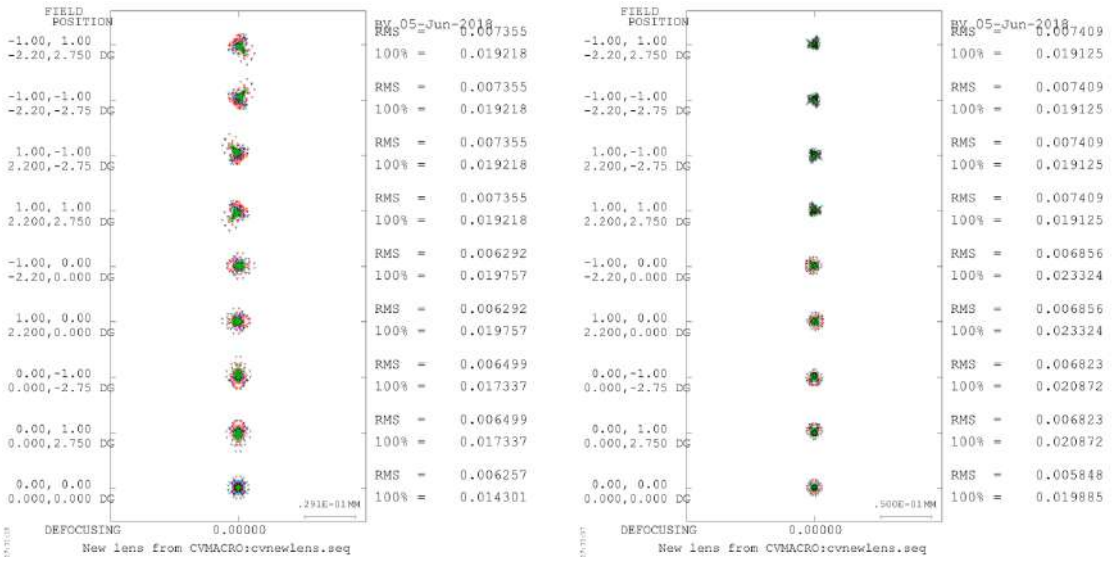

(a) T=0°C (b) T=-45°C

Fig. C.7: Spot Diagrams of the SiHGaAs optical design re-optimized for -22.5°C at maximum and minimum temperatures for aluminum mount with the image plane focused

this increase, the RMS radius value is still smaller than 7.5 μm. Therefore, in the case the image focal plane moved to the focal plane position, the system would be valid for our application. In figure C.9 and figure C.10, the defocused spot diagrams for minimum and maximum temperatures using both materials are shown for further information of the system's performance.

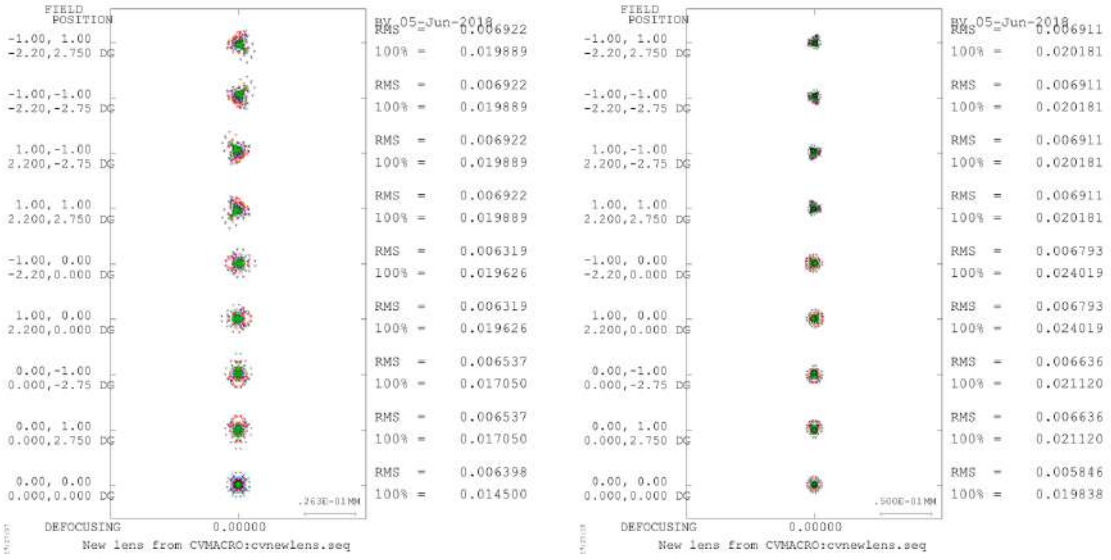

(a) T=0°C (b) T=-45°C

Fig. C.8: Spot Diagrams of the SiHGaAs optical design re-optimized for -22.5°C at maximum and minimum temperatures for invar mount with the image plane focused

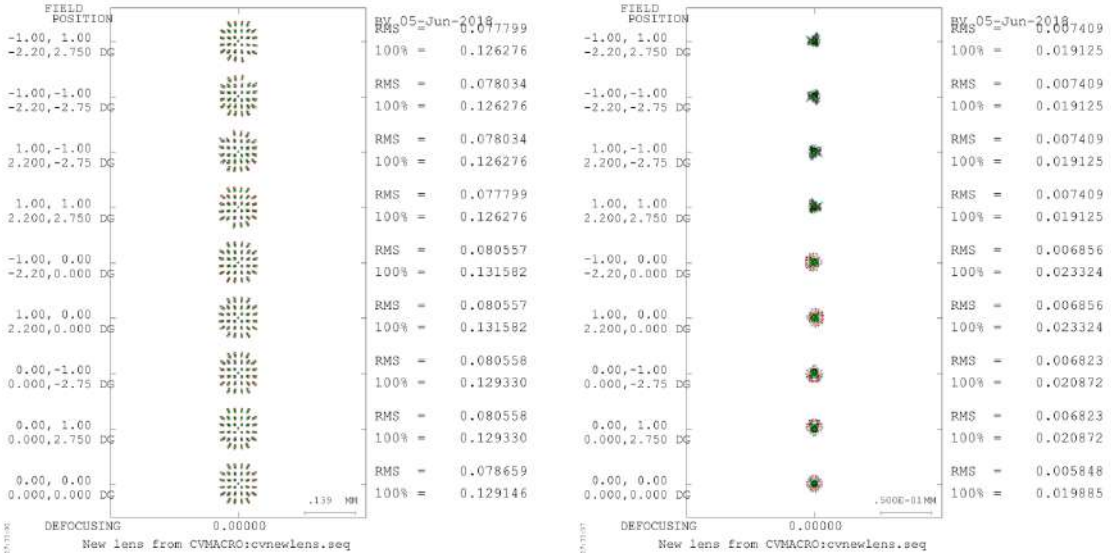

(a) T=0°C (b) T=-45°C

Fig. C.9: Spot Diagrams of the Si(h)GaAs optical design re-optimized for -22.5°C at maximum and minimum temperatures for aluminum mount

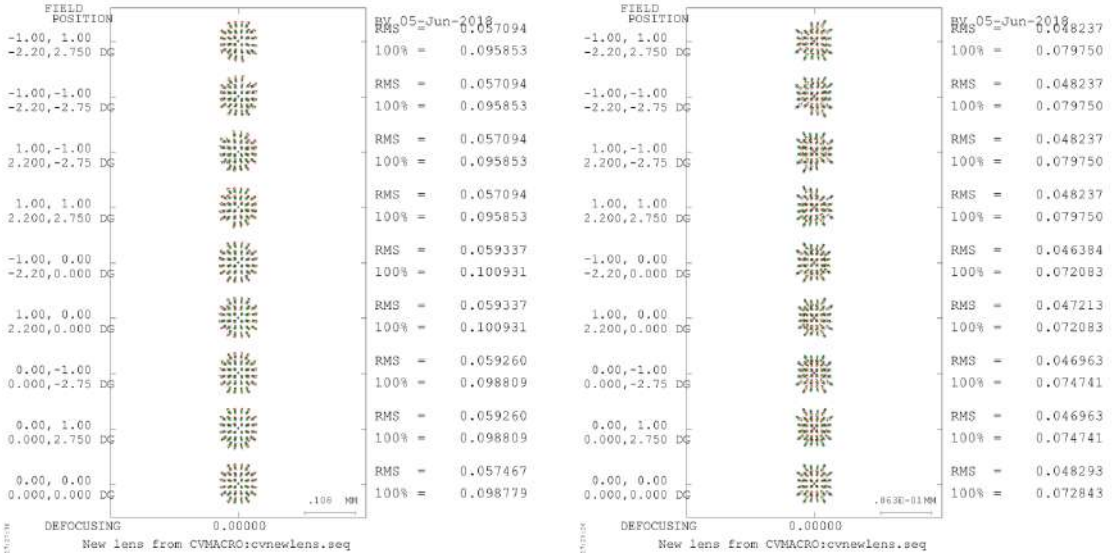

(a) T=0°C (b) T=-45°C

Fig. C.10: Spot Diagrams of the Si(h)GaAs optical design re-optimized for -22.5°C at maximum and minimum temperatures for invar mount

3 Si(h)ZnS: spot diagrams at 0°C and -45°C

In figure C.11, the spot diagram at -22.5°C is shown. The spot diagrams at minimum and maximum temperatures considering aluminum and invar materials and an ideal position of the image plane are shown in figure C.12 and figure C.13.

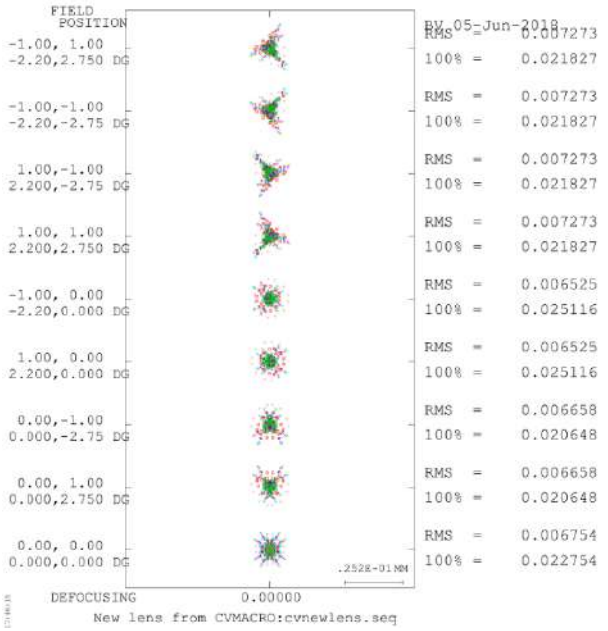

Fig. C.11: Spot diagram of the SiHZnS optical design re-optimized for -22.5°C

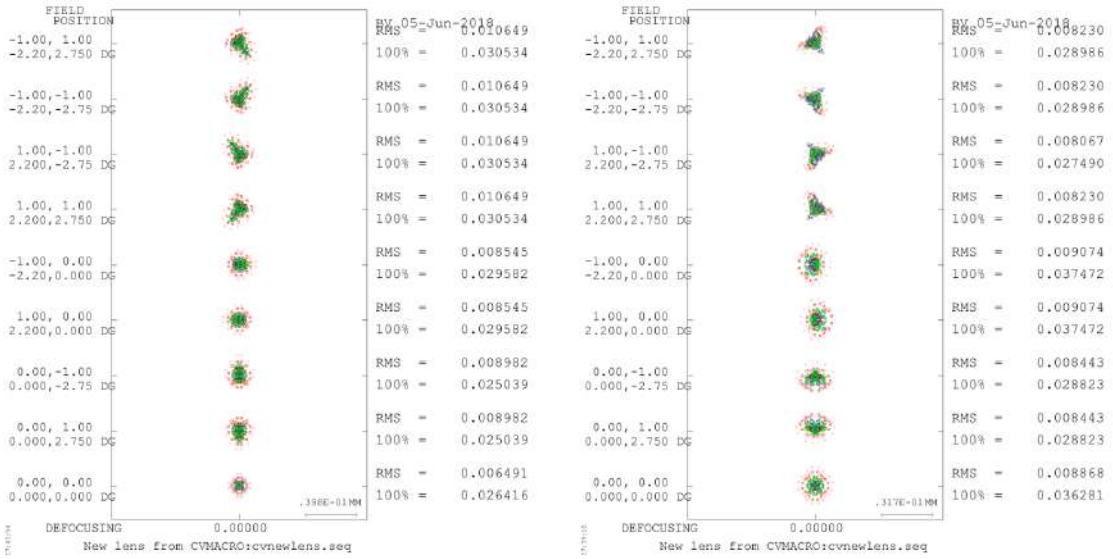

(a) T=0°C (b) T=-45°C

Fig. C.12: Spot Diagrams of the SiHZnS optical design re-optimized for -22.5°C at maximum and minimum temperatures for aluminum mount with the image plane focused

When re-optimizing the optical system, the RMS radius is almost 7.5 μm for some FoVs (see figure C.11). This proximity to the limit value makes the performance of the system no longer

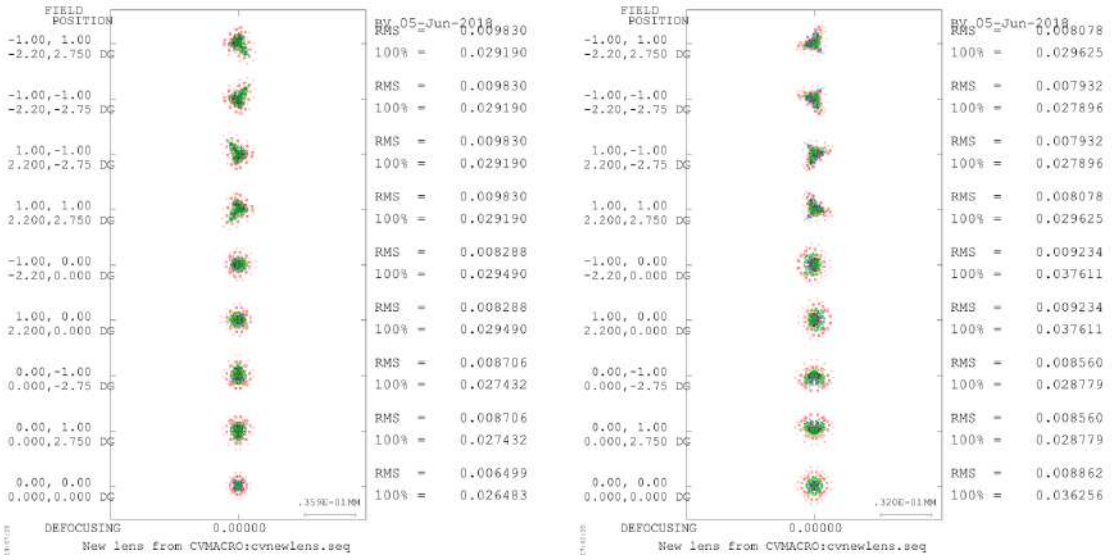

(a) T=0°C (b) T=-45°C

Fig. C.13: Spot Diagrams of the SiHZnS optical design re-optimized for -22.5°C at maximum and minimum temperatures for invar mount with the image plane focused

good when the temperature increases, given that with temperature changes the performance of the system in a worse way. The defocused spot diagrams are shown in figure C.14 and figure C.15.

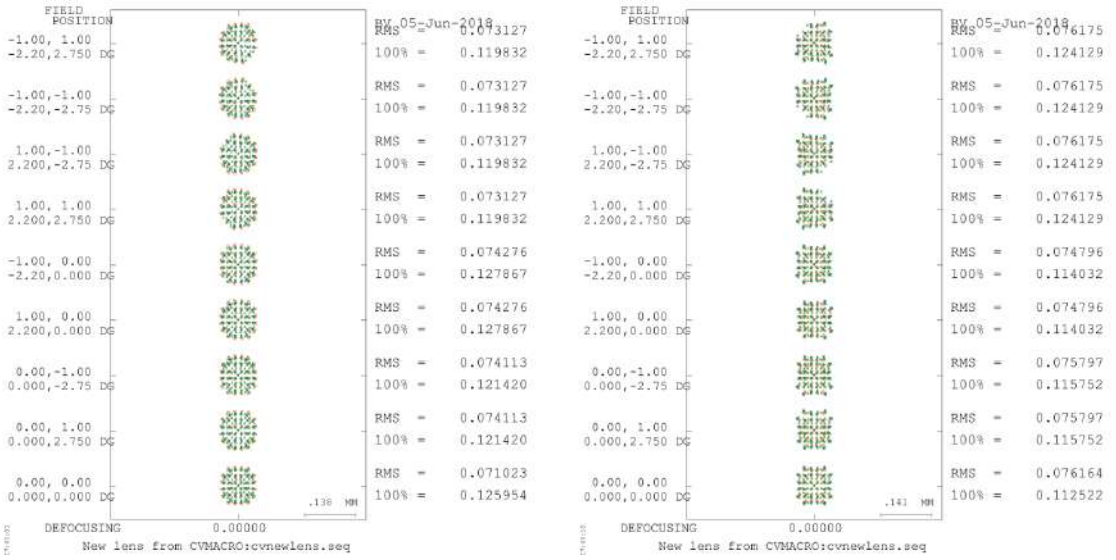

(a) T=0°C (b) T=-45°C

Fig. C.14: Spot Diagrams of the Si(h)ZnS optical design re-optimized for -22.5°C at maximum and minimum temperatures for aluminum mount

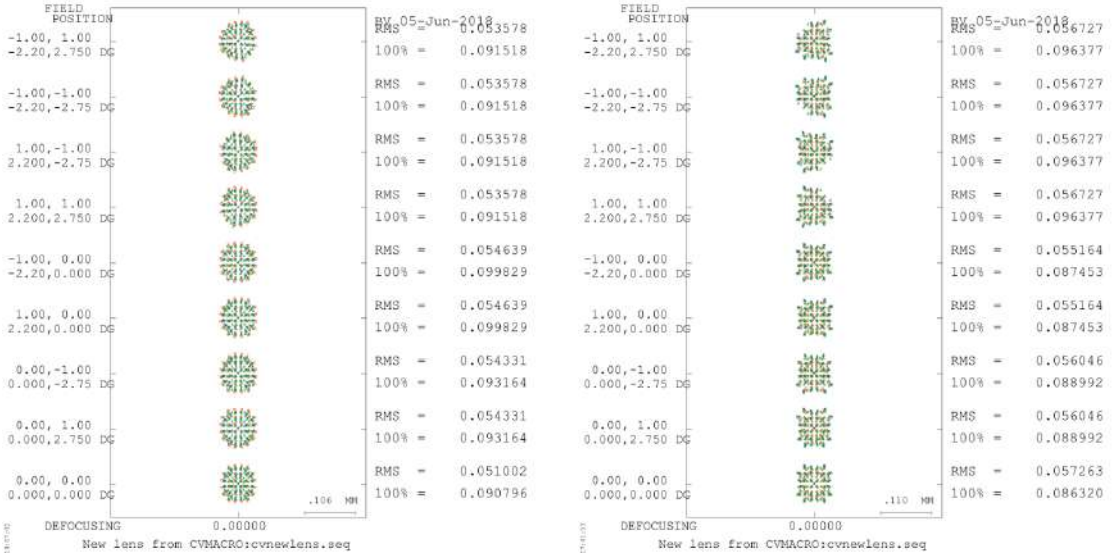

(a) T=0°C (b) T=-45°C

Fig. C.15: Spot Diagrams of the Si(h)ZnS optical design re-optimized for -22.5°C at maximum and minimum temperatures for invar mount